

Molecular Simulations of Adsorption and Self-Assembly of Surfactants on Metallic  
Surfaces

A dissertation presented to  
the faculty of  
the Russ College of Engineering and Technology of Ohio University

In partial fulfillment  
of the requirements for the degree  
Doctor of Philosophy

Xueying Ko

August 2021

© 2021 Xueying Ko. All Rights Reserved.

This dissertation titled  
Molecular Simulations of Adsorption and Self-Assembly of Surfactants on Metallic  
Surfaces

by  
XUEYING KO

has been approved for  
the Department of Chemical and Biomolecular Engineering  
and the Russ College of Engineering and Technology by

Sumit Sharma  
Assistant Professor of Chemical and Biomolecular Engineering

Mei Wei  
Dean, Russ College of Engineering and Technology

## ABSTRACT

KO, XUEYING, Ph.D., August 2021, Chemical Engineering

Molecular Simulations of Adsorption and Self-Assembly of Surfactants on Metallic Surfaces (185 pp.)

Director of Dissertation: Sumit Sharma

Surfactant molecules are widely used in the oil and gas industry as corrosion inhibitors. These inhibitor molecules are known to self-assemble in various morphologies at the metal-water interfaces. Despite their wide usage in the oil and gas industry for corrosion mitigation purposes, the selection of corrosion inhibitors is still mostly based on trial-and-error experimentation, and the mechanisms by which these molecules retard corrosion are still poorly understood. This dissertation focuses on the study of the adsorption and self-assembly of surfactant molecules of different chemistry and geometry via classical molecular dynamics of a coarse-grained model. From this research, the following key findings are made: (a) Hydrophobic interactions between surfactant tails play an important role in their adsorption and self-assembly on surfaces; (b) The morphology of the adsorbed surfactant film is dictated by the molecular geometry; (c) Entrainment of oil in surfactant films improves film integrity and hydrophobicity; (d) A theoretical model was developed that is able to predict adsorbed morphologies given geometry of surfactant molecules and their strength of interactions with the surface. It has been shown, via coarse-grained simulations, that this theoretical model is quantitatively accurate in predicting the adsorbed configurations for both linear-shaped surfactants as well as asymmetrically shaped surfactant molecules; (e) Lateral hydrophobic interactions can help surfactant molecules adsorb onto a heterogeneous surface where part of the surface has no interactions with surfactant molecules.

## DEDICATION

*To my parents Baoyue He and Fahui Li, and my husband Ben Ko, for their unconditional  
love and unwavering support.*

*And to my son Ian, without whom this dissertation would have been completed a year  
earlier, yet life is so much fuller with him.*

## ACKNOWLEDGMENTS

I would like to express my deepest appreciation to my advisor Dr. Sumit Sharma, who has been a great role model throughout my Ph.D. journey. The first time we met in person, he told me that there is never a stupid question, and he will be available anytime when I have questions for him. He has more than kept his words, and has been there every step of the way. His inquisitive mind and hardworking spirit are great inspirations for me. I have also benefited from his meticulous approach to research and learned from him how to create simple models to study complex systems.

I would also like to extend my deepest gratitude to my committee members, Dr. Srdjan Nestic, Dr. David Young, Dr. David Drabold, and Dr. Katherine Cimatu for their guidance during the past few years. I would like to thank Dr. Nestic for always keeping an open mind towards our modeling work and providing constructive feedback on our research. I also thank Dr. Young for being in every review session for board meeting presentations and helping me better understand the experimental work related to our research. Dr. Drabold helped me when I was learning the fundamentals of Density Functional Theory (DFT). Although we ended up not applying DFT in our research, the knowledge I gained through taking Quantum Mechanics and learning DFT will without a doubt serve me well in the years to come. Dr. Drabold has also graciously helped me with a recommendation letter on short notice for the Graduate College Named Fellowship application, for which I am very grateful. I also thank Dr. Cimatu for bringing her expertise into our project and sharing her group's research findings with us.

I would like to thank Dr. Monica Burdick for taking the time to write a recommendation letter for me to the Graduate College Named Fellowship, and for always being accessible to me. I also thank Dr. Sunggyu Lee for all the encouragement over the years and for making the Heat Transfer class super fun to learn. Tom Riggs, our previous graduate program coordinator, was ever a great help with all our graduate school

paperwork and keeping us on track with all our milestones. I also thank Dr. Valerie Young for helping me with my registration during my internship. I would also like to thank Dr. Bruce Brown for his great support during each CCJIP board meeting. I also thank our administrative specialist, Carrie Linscott, for taking care of all the travel reimbursements and lab purchases, and for doing it with so much patience.

I'm extremely grateful to my colleagues from my internship at Procter & Gamble for their wonderful support and collaboration. Especially helpful to me during this time were my P & G coach, Dr. Sumanth Jamadagni, who provided me with great support and encouragement throughout my stay at P & G. The unparalleled knowledge and invaluable insight he had in my internship project helped me to grow more as a scientist.

I would like to thank my current and past labmates – Himanshu, Reza, Ramin, Athena, Abolfazl, Bahar, Yathish, Mohsen, Saeed Miri, and Patrick. I have thoroughly enjoyed working with you all in the office and talking about research and life together. My stay at OU would not have been this fun without my many friends: Zheyao, Chao, Helen, Zhong, Wenwen, Xinyue, Yiying, Tasha, Sally, Junia, Ishan, Brijal, Saeed, Amid, Andrew, Nikita, and many others. I would also like to thank Jen, Tina, Brijal, Xiaorui, Andrea, Ratna, and Becky for helping to babysit Ian; you all have made life so much easier for my family during the last few months of my PhD study. Special thanks to our Central Avenue church family, our small group, and the IFI group, for all you have done for my family, and words cannot express enough how much I appreciate all of you.

I also acknowledge the National Science Foundation, Ohio University Graduate College, and the American Chemical Society Petroleum Research Fund for funding my research. I would also like to thank the Ohio Supercomputer Center and the Extreme Science and Engineering Discovery Environment for computational resources. I thank British Petroleum (BP) for granting us the permission to include experimental results in the study of co-adsorption of oil molecules with inhibitor molecules.

Last but not least, I must thank my family for all the love and support they have provided over the past many years. My husband, Ben, has given me unrelenting support and encouragement throughout my graduate school. My parents, Baoyue and Fahui, have given me all the freedom to pursue my dreams. My in-laws, Shang and Jowen have taken great care of our family whenever needed. Thank you for always being here for me. And thank you little Ian, for all the adorable distractions and interruptions - which brought so much unexpected joy and perspective into my life during this once-in-a-life-time (at least I hope so) global pandemic.

## TABLE OF CONTENTS

|   | Page      |
|---|-----------|
| Abstract . . . . .  | 3         |
| Dedication . . . . .  | 4         |
| Acknowledgments . . . . .   | 5         |
| List of Tables . . . . .  | 11        |
| List of Figures . . . . .   | 12        |
| <b>1 Introduction . . . . .</b>   | <b>15</b> |
| 1.1 Background . . . . .  | 15        |
| 1.1.1 Corrosion . . . . .   | 15        |
| 1.1.2 Corrosion Inhibitors . . . . .  | 16        |
| 1.1.3 Organic Corrosion Inhibitors . . . . .  | 17        |
| 1.1.4 Mechanisms of Corrosion Inhibition by Adsorption of Surfactant<br>Molecules . . . . .                               | 19        |
| 1.1.5 Surfactant Adsorption Morphologies . . . . .  | 20        |
| 1.2 Overview of Molecular Simulations . . . . .   | 24        |
| 1.2.1 Molecular Simulation . . . . .  | 24        |
| 1.2.2 Molecular Dynamics Simulation . . . . .   | 25        |
| 1.2.3 Coarse-grained Modeling . . . . .   | 27        |
| 1.3 Dissertation Outline . . . . .  | 28        |
| <b>2 The Role of Tail Hydrophobicity, Molecular Geometry and Surface Affinity on<br/>  Inhibitor Adsorption . . . . .</b> | <b>29</b> |
| 2.1 Introduction . . . . .  | 29        |
| 2.2 Methods . . . . .   | 31        |
| 2.2.1 Simulation System . . . . .   | 31        |
| 2.2.2 Simulation Details . . . . .  | 32        |
| 2.3 Results and Discussion . . . . .  | 33        |
| 2.3.1 Effect of Tail Hydrophobicity on Adsorption Behavior . . . . .  | 33        |
| 2.3.2 Effect of the Size of the Polar Head Group . . . . .  | 38        |
| 2.3.2.1 Adsorbed Amount . . . . .   | 38        |
| 2.3.2.2 Micelle Formation . . . . .   | 41        |
| 2.3.2.3 Nature of the Adsorbed Layer . . . . .  | 46        |
| 2.3.3 Effect of the Affinity between Polar Head Group and Surface . . . . .   | 48        |
| 2.4 Conclusions . . . . .   | 51        |

|       |   |     |
|-------|---|-----|
| 3     | A Quantitatively Accurate Theory To Predict Adsorbed Configurations of Linear Surfactants on Polar Surfaces . . . . .                                     | 54  |
| 3.1   | Introduction . . . . .  | 54  |
| 3.2   | Theoretical Model . . . . .   | 55  |
| 3.3   | Simulation System and Methods . . . . .   | 56  |
| 3.4   | Results and Discussion . . . . .  | 58  |
| 3.4.1 | Validating the Theoretical Model . . . . .  | 58  |
| 3.4.2 | Kinetics of SAM Formation . . . . .   | 62  |
| 3.4.3 | Validating the Theoretical Model for 30-Mer Surfactants . . . . .   | 69  |
| 3.4.4 | Conditions for Validity of our Theoretical Model . . . . .  | 72  |
| 3.5   | Conclusions . . . . .   | 73  |
| 4     | A Quantitatively Accurate Theory to Predict Adsorbed Configurations of Asymmetric Surfactant Molecules on Polar Surfaces . . . . .                        | 74  |
| 4.1   | Introduction . . . . .  | 74  |
| 4.2   | Theoretical Model . . . . .   | 76  |
| 4.3   | Simulation System and Methods . . . . .   | 78  |
| 4.4   | Results and Discussion . . . . .  | 80  |
| 4.4.1 | Validating the Theoretical Model . . . . .  | 80  |
| 4.4.2 | Kinetic Pathways of Formation of Adsorption Morphologies . . . . .  | 88  |
| 4.5   | Conclusions . . . . .   | 95  |
| 5     | Experiments and Molecular Simulation Study of How Co-adsorption of Oil Molecules in Adsorbed Corrosion Inhibitors Improves Corrosion Mitigation . . . . . | 98  |
| 5.1   | Introduction . . . . .  | 98  |
| 5.2   | Scope of Work . . . . .   | 100 |
| 5.2.1 | Simulation Setup: . . . . .   | 101 |
| 5.2.2 | Simulation Details: . . . . .   | 104 |
| 5.3   | Results and Discussion . . . . .  | 105 |
| 5.3.1 | Presence of Oil Molecules Promotes Adsorption . . . . .   | 105 |
| 5.3.2 | Presence of Oil Molecules Improves Corrosion Inhibition Properties of Adsorbed Films . . . . .  | 111 |
| 5.3.3 | Effect of Length of Oil Molecules . . . . .   | 113 |
| 5.3.4 | Experimental Confirmation . . . . .   | 115 |
| 5.4   | Conclusion . . . . .  | 122 |
| 6     | Adsorption Behavior of Corrosion Inhibitors on Heterogeneous Metallic Surfaces Studied using Molecular Simulations . . . . .                              | 125 |
| 6.1   | Introduction . . . . .  | 125 |
| 6.2   | Simulation System and Methods . . . . .   | 125 |
| 6.3   | Results and Discussion . . . . .  | 126 |
| 6.3.1 | Single Metal Patch System . . . . .   | 126 |

|         |   |     |
|---------|---|-----|
| 6.3.1.1 | Adsorbed Amount . . . . .   | 126 |
| 6.3.1.2 | Structure of the Adsorbed Corrosion Inhibitor Film . . . . .  | 127 |
| 6.3.2   | Multi-patch System . . . . .  | 128 |
| 6.3.2.1 | Adsorbed Amount . . . . .   | 128 |
| 6.3.2.2 | Film Structure . . . . .  | 130 |
| 6.3.3   | Distance between Metal Patches Play an Important Role in Adsorption . . . . .   | 130 |
| 6.4     | Conclusion . . . . .  | 132 |
| 7       | Salt- and pH-Dependent Viscosity of SDS/LAPB Solutions: Experiments and a Semiempirical Thermodynamic Model . . . . . | 134 |
| 7.1     | Introduction . . . . .  | 134 |
| 7.2     | Thermodynamic Model . . . . .   | 138 |
| 7.2.1   | Overview of Mixed Micelle Thermodynamics . . . . .  | 138 |
| 7.2.2   | Titration Surfactants at High Total Surfactant Concentration . . . . .  | 139 |
| 7.2.3   | Effect of Added Salt . . . . .  | 140 |
| 7.2.3.1 | Pure Component CMCs . . . . .   | 141 |
| 7.2.3.2 | Effect of Salt on Activity Coefficients in the Micelle . . . . .  | 142 |
| 7.2.4   | Final Algorithm . . . . .   | 144 |
| 7.2.5   | Example Calculations with the Model . . . . .   | 145 |
| 7.3     | Materials and Methods . . . . .   | 148 |
| 7.3.1   | Materials . . . . .   | 148 |
| 7.3.2   | Sample Preparation . . . . .  | 148 |
| 7.3.3   | Viscosity Measurements . . . . .  | 148 |
| 7.3.4   | NMR Measurements . . . . .  | 149 |
| 7.4     | Experimental Results . . . . .  | 150 |
| 7.4.1   | Viscosity Measurements . . . . .  | 150 |
| 7.4.1.1 | Effect of Added Salt . . . . .  | 150 |
| 7.4.1.2 | Effect of pH . . . . .  | 151 |
| 7.4.2   | NMR Titration of LAPB . . . . .   | 151 |
| 7.4.2.1 | pKa of Pure LAPB . . . . .  | 156 |
| 7.4.2.2 | pKa of LAPB in LAPB/SDS Micelles . . . . .  | 156 |
| 7.4.2.3 | Parameterizing $\beta$ parameters with the pKa shift . . . . .  | 158 |
| 7.5     | A Semi-empirical Model of Viscosity . . . . .   | 159 |
| 7.5.1   | A Bayesian Model for $\ln(\eta)$ based on Surfactant Chemical Activity Coefficients $\gamma_i$ . . . . .              | 162 |
| 7.6     | Conclusion . . . . .  | 165 |
| 8       | Conclusions and Future Work . . . . .   | 167 |
| 8.1     | Summary of Results . . . . .  | 167 |
| 8.2     | Future work . . . . .   | 168 |
|         | References . . . . .  | 170 |

## LIST OF TABLES

| Table   | Page |
|---|------|
| 5.1 Proprietary corrosion inhibitor MSDS listed components . . . . .  | 121  |
| 7.1 Different outputs from the thermodynamic micelle model . . . . .  | 154  |
| 7.2 Surfactant compositions tested in wt%, mM and mole fraction (in the micellar phase) . . . . .   | 155  |
| 7.3 Correlation coefficients between modeled surfactant excess chemical potential, micelle water electric potentials and experimentally measured viscosities. . . . . | 161  |

## LIST OF FIGURES

| Figure | Page  |    |
|--------|---|----|
| 1.1    | Typical structure of an imidazolium-type inhibitor. . . . .   | 18 |
| 1.2    | Schematic representations of the different regions of the adsorption isotherm. . . . .  | 21 |
| 1.3    | Proposed mechanism of surfactant adsorption. . . . .  | 24 |
|        |   |    |
| 2.1    | Adsorption behavior of surfactant molecules with $\sigma_P = \sigma$ . . . . .  | 35 |
| 2.2    | Density profile of center of mass of surfactant molecules as a function of distance from the metal surface, $z$ for $\sigma_P = \sigma$ and $\varepsilon = 0.065$ . . . . .   | 36 |
| 2.3    | Orientation factor, $S$ of molecules with $\sigma_P = \sigma$ in the bulk and the adsorbed phases. . . . .  | 37 |
| 2.4    | Comparison of adsorption behavior of surfactant molecules with different values of $\sigma_P$ . . . . .   | 39 |
| 2.5    | Shape factor and cluster analysis . . . . .   | 42 |
| 2.6    | Acylicity and asphericity of the largest cluster identified for $\sigma_P = 1.5\sigma$ as a function of $\varepsilon$ for (a) the bulk phase, and (b) the adsorbed phase. . . . .   | 44 |
| 2.7    | A snapshot of the simulation system for $\sigma_P = 1.5\sigma$ and $\varepsilon = 0.07$ . . . . .   | 45 |
| 2.8    | Fraction of the adsorbed surfactant molecules with their polar groups pointing towards the surface. . . . .   | 47 |
| 2.9    | The number of adsorbed molecules, $N$ as a function of $\varepsilon$ for 20-mer and 30-mer surfactants with $\sigma_P = \sigma$ . . . . .   | 48 |
| 2.10   | Kinetics of adsorption of corrosion inhibitor molecules. . . . .  | 49 |
| 2.11   | Total number of molecules adsorbed as a function of simulation time for different values of the affinity between polar head group and metal surface, $\varepsilon_s$ . . . . .  | 50 |
| 2.12   | Number of molecules adsorbed with their polar group towards the surface as a function of simulation time for different values of affinity between the polar head group and metal surface, $\varepsilon_s$ . . . . .                 | 51 |
|        |   |    |
| 3.1    | Summary of results of Langevin dynamics simulations performed for different values of $(\varepsilon_{TS}, \varepsilon_{HS})$ . . . . .  | 59 |
| 3.2    | Snapshots of equilibrium configurations: (a) bottom view and (b) side view for $(\varepsilon_{TS}, \varepsilon_{HS}) = (0.49, 3.0)$ . . . . .   | 60 |
| 3.3    | Equilibrium distribution of surfactant molecules as a function of distance from the surface $z$ for (a) $(\varepsilon_{TS}, \varepsilon_{HS}) = (0.49, 3.0)$ and (b) $(\varepsilon_{TS}, \varepsilon_{HS}) = (0.55, 3.0)$ . . . . . | 61 |
| 3.4    | A simulation trajectory with $(\varepsilon_{TS}, \varepsilon_{HS}) = (0.49, 3.0)$ . . . . .   | 64 |
| 3.5    | Results of a simulation trajectory with $(\varepsilon_{TS}, \varepsilon_{HS}) = (0.36, 5.0)$ . . . . .  | 66 |
| 3.6    | Results of a simulation trajectory with $(\varepsilon_{TS}, \varepsilon_{HS}) = (0.49, 2.0)$ . In this trajectory, a stripe configuration is eventually formed. . . . .   | 67 |
| 3.7    | Results of a simulation trajectory with $(\varepsilon_{TS}, \varepsilon_{HS}) = (0.4, 2.5)$ . In this trajectory, a stripes-to-SAM orientation transition is observed. . . . .  | 68 |

|      |  |     |
|------|--|-----|
| 3.8  | A simulation trajectory of 30-mer surfactant molecules with $(\epsilon_{TS}, \epsilon_{HS}) = (0.4, 4.0)$ . . . . .  | 70  |
| 3.9  | A simulation trajectory for 30-mer surfactant molecules with $(\epsilon_{TS}, \epsilon_{HS}) = (0.5, 4.0)$ is shown. A stripe configuration is eventually formed. . . . .  | 71  |
| 4.1  | Results of equilibrium adsorbed configuration obtained from simulation . . . . .   | 81  |
| 4.2  | $\theta$ and center of mass distribution . . . . .   | 82  |
| 4.3  | $\theta$ and center of mass distribution of a lying-down configuration close to the theoretical line . . . . .   | 83  |
| 4.4  | $\theta$ and center of mass distribution of a standing-up configuration close to the theoretical line . . . . .  | 84  |
| 4.5  | $\theta$ and center of mass distribution of a mixed configuration close to the theoretical line . . . . .  | 85  |
| 4.6  | Snapshot of equilibrated simulation system . . . . .   | 86  |
| 4.7  | Topview of the adsorbing surface . . . . .   | 87  |
| 4.8  | Equilibrium number of adsorbed molecules . . . . .   | 89  |
| 4.9  | Kinetics of adsorption of surfactants in lying down configuration . . . . .  | 91  |
| 4.10 | Fraction of surface coverage as a function of N . . . . .  | 92  |
| 4.11 | Kinetics of adsorption of the surfactants in standing up configuration . . . . .   | 93  |
| 4.12 | Formation of islands of adsorbed molecules during adsorption process . . . . .   | 94  |
| 4.13 | Number of islands of adsorbed molecules as a function of the fraction of the surface covered by surfactant molecules . . . . .   | 96  |
| 5.1  | A schematic of the coarse-grained model of a corrosion inhibitor. . . . .  | 101 |
| 5.2  | (a) A snapshot of an equilibrium configuration of the pure inhibitor system ( $\sigma_p = 2\sigma$ ). (b) An enlarged snapshot of adsorbed film of the pure inhibitor system ( $\sigma_p = 2\sigma$ ). Blue colored beads are the polar head groups, and cyan colored beads are the hydrophobic tails. (c) Distribution of angles, $\theta$ , that adsorbed molecules make with the surface normal. . . . .  | 106 |
| 5.3  | (a) A snapshot of an equilibrium configuration of the inhibitor+oil system ( $\sigma_p = 2\sigma$ ). (b) An enlarged snapshot of configuration of the inhibitor+oil system ( $\sigma_p = 2\sigma$ ). Blue colored beads are the polar head groups, cyan colored beads are the hydrophobic tails, and the red colored beads represent the oil molecules. (c) Distribution of angles, $\theta$ , that adsorbed molecules make with the surface normal. . . . .                     | 108 |
| 5.4  | (a) A snapshot of an equilibrium configuration of the pure inhibitor system ( $\sigma_p = \sigma$ ). (b) A snapshot of equilibrium configuration of the inhibitor+oil system ( $\sigma_p = \sigma$ ). Oil molecules are in red and inhibitor molecules are in cyan with a blue colored polar head group. (c) Distribution of angles, $\theta$ , that adsorbed molecules make with the surface normal for $\sigma_p = \sigma$ with oil and without oil molecules present. . . . . | 109 |
| 5.5  | Number of molecules adsorbed per unit area with oil and without oil . . . . .  | 110 |

|      |  |     |
|------|--|-----|
| 5.6  | Radial distribution function in the XY plane for pure inhibitor system and mixture system . . . . .  | 112 |
| 5.7  | Comparison of film hydrophobicity for $\sigma_p = 2\sigma$ and $\sigma_p = \sigma$ with oil and without oil molecules present. . . . .   | 113 |
| 5.8  | Number of inhibitor molecules adsorbed on the surface at equilibrium for a pure inhibitor system, or with oil at molecule chain lengths of 10, 19, and 25. . . . .   | 115 |
| 5.9  | Experimental configuration for testing inhibitor efficiency and persistency. . . . .   | 117 |
| 5.10 | Inhibitor adsorption experiments with Inhibitor # 1 conducted with and without the presence of a hydrocarbon (80°C, pH 6.0, 0.5 ionic strength brine, RCE at 20 Pa WSS, 1000 ppm LVT 200). . . . .   | 119 |
| 5.11 | Inhibitor adsorption and dilution experiments with Inhibitor #1 conducted with and without the presence of a hydrocarbon (80°C, pH 6.0, 0.5 ionic strength brine, RCE at 20 Pa WSS, 1000 ppm LVT 200). . . . .   | 120 |
| 6.1  | Number of adsorbed molecules N, as a function of the surface area of the metal patch . . . . .   | 127 |
| 6.2  | Fraction of surface covered by inhibitor molecules as a function of the surface area of the metal patch . . . . .  | 128 |
| 6.3  | Fraction of adsorbed molecules with their polar group pointing toward surface . . . . .  | 129 |
| 6.4  | Number of adsorbed molecules N, as a function of the surface area of the metal patch. . . . .  | 130 |
| 6.5  | Fraction of molecules with their polar group pointing toward surface . . . . .   | 131 |
| 6.6  | Number of adsorbed molecules as a function of distance between patches . . . . .   | 132 |
| 7.1  | (A) Effect of salt on the electric potential, $\psi$ (from Eqn. 7.13), (B) the change in the electric potential compared to the no-added salt case and (C) the effect on the CMC (from Eqn. 7.12) for anionic micelles of different charge densities . . . . . | 143 |
| 7.2  | Thermodynamic properties of a 50/50 (equimolar) SDS/LAPB micelle as a function of pH and salt. . . . .   | 145 |
| 7.3  | Same as Fig. 7.2 but for an 80/20 SDS/LAPB mixture. . . . .  | 146 |
| 7.4  | Viscosity of 12 wt% SDS/LAPB mixtures as a function of added salt in the pH range of 4.5-6.0 . . . . .   | 151 |
| 7.5  | Viscosity of 12 wt% SDS/LAPB mixtures as a function pH with no added salt. . . . .   | 152 |
| 7.6  | NMR spectrum . . . . .   | 153 |
| 7.7  | NMR fitting . . . . .  | 156 |
| 7.8  | Correlation between measured NMR shift of LAB with solution viscosity . . . . .  | 157 |
| 7.9  | Pair-plot of correlations between various parameters . . . . .   | 160 |
| 7.10 | Results of the Bayesian regression . . . . .   | 163 |

# 1 INTRODUCTION

Adsorption of surfactants on metallic surfaces has many applications, including corrosion mitigation in oil and gas pipelines[1], synthesis of anisotropic metal nanoparticles [2], modulating electrochemical reactions [3], and tuning the selectivity of chemical reactions [4]. The direct application of interest is the use of surfactants as corrosion inhibitors to mitigate internal corrosion of oil and gas pipelines [5].

Corrosion is a major concern for the oil and gas industry, costing more than \$ 7 billion per year in maintenance in the United States (US) alone [6]. Besides the huge economic loss that can be caused by corrosion, it can also damage the environment, and sometimes even lead to life-threatening incidents [7]. A popular and cost-effective way to mitigate internal corrosion in oil and gas pipelines is to inject certain surfactant molecules in parts-per-million levels into the oil stream. These surfactant molecules, called corrosion inhibitors, adsorb onto metal-water interfaces and are known to self-assemble in organized layers to form a protective film of molecular dimensions to retard corrosion [8]. However, the performance of these molecules varies with operating conditions, leading to unpredictable behaviors and corrosion-related failures. Therefore, there is an urgent need to design new inhibitor molecules with well-understood and robust corrosion mitigation capabilities under varying conditions. So far, this endeavor has largely been driven by trial and error experimentation. This is because a critical knowledge gap exists in our understanding of the mechanisms of adsorption and self-assembly of these molecules.

## 1.1 Background

### 1.1.1 Corrosion

Corrosion is defined as the gradual destruction or deterioration of materials (usually metals) because of reactions with their environment [9]. It's an electrochemical process that involves cathodic (reduction) and anodic (oxidation) reactions. In every corrosion reaction,

the anodic reaction is the metal oxidation to its ion [9].

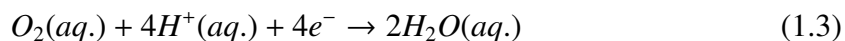


In metallic corrosion, several different cathodic reactions are common [9]:

Hydrogen evolution:



Oxygen reduction (acidic solutions):



Oxygen reduction (neutral or basic solutions):



In an acidic environment, hydrogen evolution is the common cathodic reaction. Oxygen reduction is also very common because any aqueous solution in contact with air can produce this reaction. In neutral or basic solutions, oxygen reduction is the common cathodic reaction. Corrosion is inevitable whenever we have metals like iron and copper exposed to air or water, and it happens in many industrial settings and is a major concern requiring significant maintenance and monitoring requirements. However, by understanding the mechanisms and fundamentals of this process, the cost of corrosion can be considerably reduced by different corrosion inhibition methods [7], such as via the use of protective coatings, corrosion-resistant alloys, sacrificial anodes, and/or corrosion inhibitors. The scope of this proposed research is limited to the modeling the adsorption behavior of corrosion inhibitors for the oil and gas industry.

### 1.1.2 Corrosion Inhibitors

A corrosion inhibitor is a chemical substance that, when added in small concentrations (ppm level) to a corrosive environment (such as into oil and gas pipelines), increases

corrosion resistance, and thus help to mitigate corrosion[10]. The use of corrosion inhibitors is considered as one of the most effective and economic ways of mitigating corrosion in the oil and gas industry. The majority of corrosion inhibitors have been developed by empirical experimentation, and many of them are proprietary in nature and thus their composition is not disclosed. Due to these reasons, their inhibition mechanism is not well understood [9].

Generally, the inhibition mechanism falls into one or more of the three categories below [8]:

- The corrosion inhibitor is chemically or physically adsorbed on the metal surface and forms a protective layer and inhibits the cathodic and anodic processes. Most organic inhibitors are in this category;
- The corrosion inhibitor facilitates the formation of an oxide film on the metal substrate. In general, they are primarily used for corrosion inhibition of metals and alloys that demonstrate active-passive transitions;
- The inhibitor acts by reacting with potential corrosive reagents from the solution. They work effectively in solutions where oxygen reduction is the main corrosion cathodic reaction but are not very effective in strong acid solutions.

### **1.1.3 Organic Corrosion Inhibitors**

Inhibitors can be classified in different ways, such as their chemical structure (organic or inorganic), their inhibition mechanism, as oxidants or not oxidants [8]. Almost 80% of the inhibitors used today are organic compounds that adsorb onto the metal surface. As this type of inhibitors are widely used in the oil and gas industry, they will be the focus of our studies.

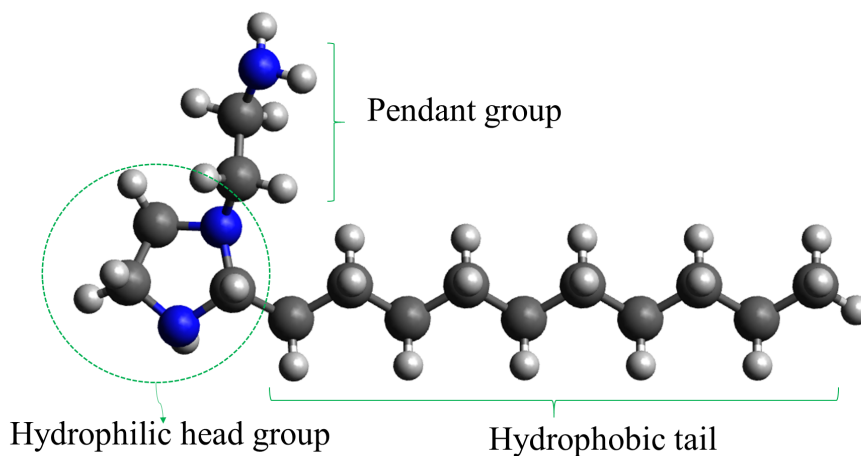


Figure 1.1: Typical structure of a generic imidazolium-type inhibitor. The molecule consists of a hydrophilic head group, a long hydrophobic tail, and a pendant group.

Organic corrosion inhibitors are often surfactant molecules with a typical three parts structure. Figure 1.1 shows a typical corrosion inhibitor molecule structure using imidazolium-type corrosion inhibitors as an example since they are widely used in the oil and gas industry. These molecules have a polar functional group and a hydrophobic tail. The polar head group often contains a heteroatom such as N, O, or S, that is understood to have strong affinity for the metal surface, and thus promotes adsorption [11–13]. The hydrophobic tails are long hydrocarbon chains (usually C6-C22) [14]. The lateral interactions between the hydrophobic tails help form a hydrophobic layer and retard corrosion [1, 15]. Imidazole, imidazoline, quaternary ammonium, and amid-amine based surfactants are some of the popular corrosion inhibitors that are used due to their high efficacy and low toxicity [1, 16, 17].

#### 1.1.4 Mechanisms of Corrosion Inhibition by Adsorption of Surfactant Molecules

Extensive experimental studies, such as saturation adsorption data [5], Electrochemical Impedance Spectroscopy (EIS) [18, 19], Second Harmonic Generation Laser Scattering [1], and Atomic Force Microscopy (AFM) [20] indicate that organic inhibitor molecules mitigate corrosion by self-assembly into monolayers or micelles onto metal surfaces upon adsorption. Several unique characteristics of organic corrosion inhibitors are understood to determine the effectiveness of corrosion inhibitors. Ramachandran *et al.* [21] suggest that for a molecule to be an effective corrosion inhibitor, it should have the following characteristics: (1) having a polar head group that strongly binds to the metal surface and displaces water; (2) ability to self-assemble with hydrophobic tails tightly packed to serve as a barrier for diffusion of water and ions towards the metal; and (3) the molecule should have sufficient solubility and rate of transport towards the metal surface to form a self-assembled monolayer (SAM) at a much faster rate than the corrosion rate.

Besides adsorption processes, surfactant interactions, water/oil partitioning, precipitation, surfactant interactions, and micellizations also directly influence corrosion inhibition efficiency [22]. Factors such as temperature and flow condition in the pipeline also affect inhibition efficiency. Hence, it is not a straightforward task to evaluate corrosion inhibition efficiency [23]. Many different approaches to describe the effect of corrosion inhibitors have been discussed in the literature, varying from using simple inhibition efficiencies to applications of complicated molecular modeling techniques [24]. It is generally assumed that good surface coverage is essential for effective corrosion inhibition, that is to say, the degree of protection is directly proportional to the fraction of metal surface covered by the inhibitor [25, 26].

While experimental observations highlight that corrosion inhibition efficiency is mainly measured by surface coverage by surfactant molecules, this is a simplistic assumption. There is limited research on what adsorption morphologies do surfactant

adsorb, or how these different morphologies change surface coverage, or retard corrosion. Many different factors, such as the molecular structure of inhibitor molecules, geometries of inhibitor molecules and the metal-inhibitor interaction could changes the adsorption behavior of surfactants on metallic surfaces, and needs to be investigated.

### **1.1.5 Surfactant Adsorption Morphologies**

Many previous experimental studies have focused on understanding how surfactants organize and adsorb on polar surfaces. These studies provide interesting insights on various factors that seem to govern the adsorption behavior of surfactants on these surfaces.

One method commonly used to understand the adsorption morphologies and mechanisms was adsorption isotherms. A few different models have been proposed based on the adsorption isotherms, which are determined by solution depletion methods traditionally [27]. In general, the adsorption isotherm can be analyzed by the slope change that indicates a change in the surface excess with concentration. In this way, the isotherm can be divided into different regions, and the most likely configurations formed by surfactants on the surface can be inferred.

One early model of the adsorption isotherm is the bilayer model [28]. Using the nitrogen Brunauer-Emmett-Teller (BET) method, the adsorption of cetyltrimethylammonium bromide (CTABr) on silica at high pH was studied [29]. From the adsorption results, it was suggested that a bilayer of surfactant ions were formed on silica surface (Figure 1.2 (right)). According to this model, the surfactant molecules adsorb from the beginning as bilayers and full coverage of the surface is reached after the critical micelle concentration (CMC) [30].

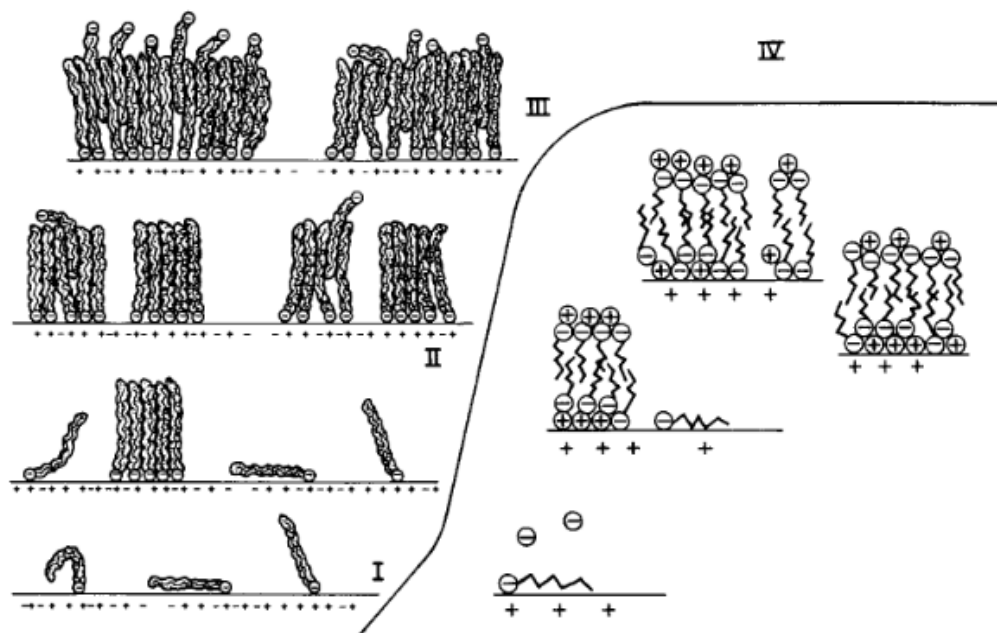


Figure 1.2: Schematic representations of the different regions of the adsorption isotherm.(left)reverse orientation model,(right)the bilayer model [31].<sup>1</sup>

Using luminescence, electron spin resonance, and time-resolved resonance Raman, Somansundran *et al.* [31] studied the adsorption of sodium dodecyl sulfate (SDS) on alumina, and proposed a reverse orientation model of adsorption isotherm. Figure 1.2(left) shows the suggested adsorbed morphologies of adsorbed surfactant molecules in different region. In region I, molecules start to adsorb due to the surface-surfactant affinity. At higher surfactant concentration, in region II, adsorption increases due to the aggregate structure formation on the surface. Surfactants can form hemi-micelles or micelles due to the lateral hydrophobic interaction between the hydrocarbon tails. In region III, the electrostatic interaction is less dominant due to the neutralization of the surface by surfactant molecules, a decrease in adsorption is shown, where most adsorption happens because of the lateral

<sup>1</sup> This figure was published in *Colloids and Surfaces*, Volume 37, P. Somasundaran, Joy T. Kunjappu, In-situ investigation of adsorbed surfactants and polymers on solids in solution, Pages 245-268, Copyright Elsevier (1989). Reproduced with permission.

interaction of the hydrocarbon tails. Some of the molecules adsorb with the head facing the solution, resulting in a reverse orientation of the surfactant molecules, hence the name of the model. In region IV, not much adsorption happens because of the micelle formation in the solution. Maximum surface coverage is determined by micelle formation in the bulk. Comparing the bilayer model and the reverse orientation model (Figure 1.2), the bilayer model suggested that the hydrophobic tails of the top layer do not penetrate and interact with the tail groups in the bottom layer.

For nonionic surfactants, they tend to form hydrogen bonds with the surface. Because of the weaker interaction of hydrogen bonds compared to electrostatic interactions, their adsorption to most solid surfaces is weaker compared to ionic surfactants. There is a sharp increase in region III in the adsorption isotherm for nonionic surfactants, which can be attributed to the diminished electrostatic interactions. In all other regions, the adsorption isotherm for nonionic and ionic surfactants show similar characteristics [23].

Atkin *et al.* [28] suggested that surfactants adsorb into discrete aggregates on the surface rather than the traditional monolayer/bilayer. Adsorption of ionic surfactants is controlled by electrostatic and hydrophobic interactions. The adsorption isotherm can be divided into different spans based on the driving force of adsorption. The three spans are the electrostatic concentration span, the electrostatic-hydrophobic concentration span, and the hydrophobic concentration span. Mechanisms of each span are available to surfactant adsorption at greater concentrations as well. For example, in the hydrophobic concentration span, hydrophobic interactions are accountable for micelle formation, and as the micelles approach the surface, the electrostatic mechanisms begin to operate. This model is shown in Figure 1.3.

These models affirm the two balancing forces of electrostatic interactions (or hydrogen bonding for nonionic surfactants) and hydrophobic interactions. One key difference is

the morphology of adsorbed surfactants; another one is that Atkin suggests that direct adsorption of micelles above the solution CMC is possible.

Although AFM [20, 32], neutron reflectivity [33], optical reflectometry [34], and some other modern experimental techniques have offered some credible evidence for these proposed mechanisms of adsorption and adsorption isotherm models, it is challenging to separate the different factors that govern the adsorption process in an experimental setting. The hydrophobic tail interactions, surface-polar head group affinities, size of polar head group, the concentration of surfactant and counter-ions, and length of hydrophobic tails, etc. can all play a role in the adsorption process, thus changing the adsorbed morphologies on surfaces. Using computational approaches such as molecular dynamics simulations, it is possible to systematically study different factors and it can aid in this endeavor to decipher the adsorption mechanism and determine the effect of hydrophobic interactions and electrostatic interactions in the adsorption process. In this current work, we employed molecular dynamics simulations to study the adsorption and self-assembly of surfactant molecules, and in this next section, a brief discussion on molecular simulations will be provided.

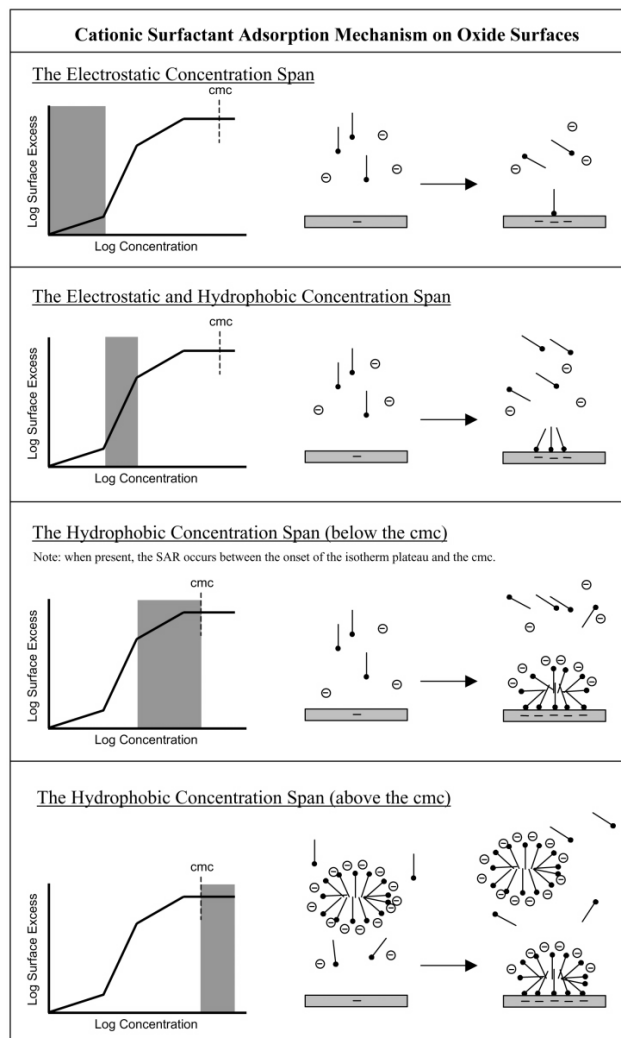


Figure 1.3: Proposed mechanism of surfactant adsorption [35].<sup>2</sup>

## 1.2 Overview of Molecular Simulations

### 1.2.1 Molecular Simulation

Computer simulation is the use of computers to represent or imitate the behavior of a system. Physical, chemical, biological, and astrophysical systems have all been studied

<sup>2</sup> This figure was published in *Advances in Colloid and Interface Science*, Volume 103, Issue 3, R. Atkin, V.S.J. Craig, E.J. Wanless, S. Biggs, Mechanism of cationic surfactant adsorption at the solid–aqueous interface, Pages 219–304, Copyright Elsevier (2003). Reproduced with permission.

using computer simulations over the past decades [36–40]. Computer simulations can provide valuable results for problems in statistical mechanics, which may otherwise be hard to study, and act as a good test for theories. The results of computer simulations can be compared with real experiments, and from this comparison, the model underlying the simulation can be tested. In this sense, computer simulation acts as a bridge between theoretical models and experimental results and may offer insights and interpretations of what we see in real experiments [41, 42].

Molecular simulation is a type of computer simulation wherein the motion of molecules comprising a physical system is studied. Two of the most often used molecular simulation methods are Monte Carlo (MC) and Molecular Dynamics (MD). Since in this work, we have used MD to study inhibitor molecules, I will briefly introduce MD simulations in the following section. Readers interested in learning about the MC method can read about it in the literature [41, 42].

### **1.2.2 Molecular Dynamics Simulation**

MD simulation, as the name suggests, use computer to simulate the dynamics of molecules in a complex system. There are two approaches for MD methods, the classical MD simulation (often just referred as MD simulations), where atomic and molecular motions are defined by classical Newtonian mechanics; and the quantum MD simulation, where the potential energy of the system is calculated using quantum mechanical techniques, like density functional theory (DFT) [43]. Although quantum MD simulations are more accurate in estimating the electronic interactions between atoms, it is computationally more costly and is therefore limited to systems with a relatively small size and time scale than classical MD simulations. Classical MD simulation is better suited to study the adsorption process of inhibitor molecules, which involves interactions between a large number of molecules. When carrying out an MD simulation, the interactions between

different atoms can be represented using different potential functions, and the mathematical form and parameters used to calculate these potential functions of the system are called force field. For any configuration of atoms, forces can be calculated from the force field. The objective of statistical mechanics is to provide the molecular theory or interpretation of equilibrium properties of macroscopic systems. It connects the statistical properties of molecular configurations to thermodynamic properties. For example, the average kinetic energy is related to temperature. In an MD simulation, wherein each atom in the system can be explicitly represented, is called atomistic MD simulations. Atoms can also be grouped together and represented by a united atom or a “bead”, thus reducing the resolution and increasing the speed thereby providing us the capability of studying larger systems and longer time-scales. This type of simulation is called coarse-grained MD simulation. The basic idea of an MD simulation is similar to doing a real experiment in the lab. First, we prepare a sample: a model system containing  $N$  particles; the forces acting on all atoms are calculated using the potential functions, and then Newtonian equations of motion are integrated numerically in time to simulate molecular motion. According to the laws of statistical mechanics, mechanical properties, such as energy, temperature, pressure, etc. can be calculated as arithmetic averages over molecular configurations. When thermodynamic properties become time-invariant in the simulations then it is understood that the system has achieved equilibrium. After equilibrium, the properties of interest for a particular system will then be measured.

In atomistic MD simulations, the numerical integration of Newtonian equations of motion is of the order of  $10^{-15}$  seconds (femtosecond) [41]. To simulate a system over one nanosecond (ns) requires a million timesteps. In each timestep, forces for every atom need to be calculated. This is a relatively expensive calculation and takes a large amount of time. Thus, atomistic MD simulations, in general, can only sample systems for timescales from 1-100 ns. To sample timescales larger than this, CG MD simulation is implemented. In

doing so, the number of degrees of freedom is reduced, so some details of the system are lost, however, CG simulations help increase the computational efficiency and provide us the tools to probe system for a longer time where the adsorption process can be studied.

### 1.2.3 Coarse-grained Modeling

As stated in the previous section, atomistic MD simulations are suitable to study systems that are relatively smaller ( $10^3$  -  $10^5$  atoms) and over shorter time scales ( $\sim 10$  - 1000 ns) while CG simulations can be used to study collective behaviors of relatively large systems. In the CG models, since different atoms are grouped together into a CG bead, and the interactions between beads are represented by potential functions. As an example, a  $CH_3$  group can be represented by a single bead. Now, the motion of hydrogens are no longer modeled, a longer simulation timestep can be used. Furthermore, since the number of atomic entities are reduced, calculation of forces is also much faster. In our case, the adsorption of a large number of surfactant molecules can be simulated via CG models.

Previously, Duda *et al.* performed an MC simulation of corrosion inhibitor molecules in two dimensions and confirmed that molecular properties such as tail length, interactions with the substrate, size ratio between head group and tail unit, play an important key role in the adsorption behavior [17]. Wu *et al.* studied self-assemblies of ammonium-based surfactants using the MARTINI force field model, and found that the aggregation of surfactants has three stages: fast aggregation of monomers into disordered oligomers; larger aggregates grow by combining smaller ones; micelle formation with stable numbers. With smaller aggregation numbers ( $<100$ ), the surfactants form spherical micelles; worm-like micelles at a larger aggregation number are observed [44]. These CG models offered insights on key factors in adsorption and self-assembly and helped in the understanding and developing our own model to study the adsorption and self-assembly behavior of corrosion inhibitors.

### 1.3 Dissertation Outline

Chapter 2 of the dissertation introduces the developed CG model of surfactant molecules. Using this model, the importance of alkyl tail hydrophobicity in the adsorption behavior of surfactant molecules is examined. Then the effect of molecular geometry on the adsorption morphologies, and how surfactant polar head group affinity changes the kinetics of adsorption are studied. In chapter 3, a theoretical model is developed to predict adsorption morphologies of linear surfactant molecules. Linear molecules adsorb on the surface either in a strip-like configuration with the molecular axes parallel thereon, or in a self-assembled monolayer (SAM) with the axes perpendicular to the surface. Depending on the relative energetics of the two configurations, it is demonstrated that the theoretical model quantitatively agrees with the simulations. In chapter 4, the model described in chapter 3 is extended to asymmetric molecules and a discussion of the difference in adsorbed configurations is provided. How the model can explain the different kinetic pathways of adsorption of surfactant molecules on polar surfaces is also discussed here. Chapter 5 of the dissertation investigate how exposure to oil molecules affects the nature of the adsorbed corrosion inhibitor films on metal surfaces, where after introduction of a hydrocarbon phase into the system, how these oil molecules interact with corrosion inhibitors and thus change the adsorbed inhibitor film is investigated. In chapter 6, the adsorption behavior of surfactant molecules on a surface that is heterogeneous in its affinity for the molecules is investigated. This is to help understand the issue that, particularly in field conditions, the surface is always not uniform and corrosion inhibitors may have different affinity to different regions of the surface. In chapter 7, a semi-empirical model that links the rheology of surfactant mixtures to thermodynamics parameters is described. Chapter 8 provided some discussions of future work of this presented research.

## 2 THE ROLE OF TAIL HYDROPHOBICITY, MOLECULAR GEOMETRY AND SURFACE AFFINITY ON INHIBITOR ADSORPTION<sup>3</sup>

### 2.1 Introduction

Metal-water interfaces are ubiquitous in heterogeneous catalysis [45] and electrochemical reactions [46]. The ability to adjust properties of these interfaces via adsorption of surfactants has found applications in corrosion inhibition [47], electrochemistry [3], biomimetic design [48], fuel cells [49] and energy storage [50]. The direct application of interest is the use of surfactants as inhibitors of aqueous corrosion of metals in oil and gas pipelines. Organic, surface-active amphiphilic molecules have been found to be effective corrosion inhibitors. [5, 16, 47] These molecules contain both hydrophobic (non-polar “tail”) and hydrophilic (polar “head”) groups. The hydrophobic tails are long alkyl groups (usually C6 to C22), while hydrophilic heads are either non-ionic or ionic functional groups. Imidazoline, quaternary ammonium, amide and amido-amine based surfactants are popular corrosion inhibitors because of their low toxicity and high efficacy [1, 16, 17]. Due to their amphiphilic nature, these molecules adsorb on to metal-water interfaces and alter the nature of electrochemical reactions [18]. However, the performance of these compounds is found to vary with operating conditions leading to unpredictable behavior and many corrosion-related failures [47, 51]. Hence, there is a need to design new inhibitor molecules with well-understood and robust corrosion mitigation capabilities under varying conditions. So far, this pursuit has largely relied on trial and error experimentation [47, 52–55] because a fundamental understanding of the relationship between adsorption characteristics and molecular properties of surfactant molecules has been lacking.

---

<sup>3</sup> Adapted with permission from Ko, X., & Sharma, S. (2017). Adsorption and self-assembly of surfactants on metal–water interfaces. *Journal of Physical Chemistry B*, 121(45), 10364–10370. Copyright(2017) American Chemical Society.

Adsorption of surfactant molecules on hydrophobic surfaces is mainly driven by hydrophobic interactions between the alkyl tails and between the alkyl tails and the surface [56, 57]. As a result, hemi-cylindrical or hemi-spherical structures are observed in the adsorbed phase [56, 58]. On polar surfaces, initial stages of adsorption of surfactants is driven by the affinity between the polar head groups and the surface and/or adsorbed counter-ions [53]. In later stages, lateral hydrophobic interactions between the alkyl tails are understood to promote adsorption. [59, 60] The resulting adsorbed phases manifest many different morphologies, such as self-assembled layers or cylindrical or spherical micelles. [3, 61, 62] Adsorption isotherms of quaternary ammonium based surfactants with longer alkyl tails are observed to shift towards lower concentrations in comparison to the ones with shorter tails, highlighting the importance of hydrophobic interactions in promoting adsorption [63, 64]. Whereas, equilibrium adsorbed concentrations of imidazoline-based surfactant molecules on metal-water interfaces have been reported to be invariant of the alkyl tail length [1]. These seemingly contrary results on the role of alkyl tails on adsorption have not been reconciled.

Alkyl tails of adsorbed surfactants are known to affect interfacial properties; for example, molecules with small alkyl tails ( $< C_6$ ) show a significantly reduced corrosion inhibition efficiency [1]. The inability of small alkyl tails to form an effective hydrophobic barrier is often cited as the reason for these observations. For corrosion inhibition and electrochemistry applications, complete coverage of metal-water interfaces with surfactants is desired to achieve electrochemical “blocking” [3, 5]. The premise that adsorption is chiefly governed by the interaction between polar groups and the surface has prompted researchers to test surfactants with highly polar head groups comprising of bulky heterocyclic and aromatic groups [47]. However, little importance is given to understanding how the size of the polar head group impacts the nature of the adsorbed layer. Hence,

there is a need to perform a systematic investigation of how different molecular features of surfactants affect their adsorption characteristics on metal-water interfaces.

In this work, we employ molecular simulations to understand how the hydrophobic character of the alkyl tail and the size of the polar head group of the surfactants affect their adsorption behavior on a metal surface. It is found that tail hydrophobicity plays an important role in driving adsorption and self-assembly of surfactant molecules. The geometry of the molecule dictates the aggregation morphology in the adsorbed and the bulk phases.

## 2.2 Methods

### 2.2.1 Simulation System

A coarse-grained bead-spring model is used to represent surfactant molecules. All quantities in the simulation system are defined in reduced units of energy, mass and length, and therefore the results can be translated into real units by appropriate conversions [65]. In this model, one terminal bead of a surfactant molecule is the polar head bead and the remaining beads are hydrophobic and form the tail. The beads are connected via bonded interactions modeled using a harmonic potential. The angles between adjacent bonds in a surfactant molecule are restrained via angular harmonic potentials centered at  $180^\circ$ . Water molecules are not modeled explicitly. An effective attractive interaction between the hydrophobic tail beads incorporates the hydrophobic effect. This interaction is modeled as a Lennard Jones (LJ) potential with a well-depth  $\varepsilon$  (arbitrary energy units) and the length parameter  $\sigma$  (arbitrary length units). The polar beads interact with all other beads via a purely repulsive Weeks-Chandler-Andersen (WCA) potential [66]. WCA potential comprises of only the repulsive part of the LJ potential. The basis of employing this potential is the understanding that the interactions of a polar group with water and with other polar and hydrophobic groups are similar in magnitude and length-scale in an aqueous

medium. As a result, there are no net attractive interactions between two polar groups or between a polar group and a hydrophobic group in aqueous medium [67]. The surface is represented by a smooth wall at  $Z = 0$ . The strong affinity between the polar beads of the surfactant molecules and the surface is modeled by a 9-3 interaction potential with the well-depth parameter  $\varepsilon_s$ . The hydrophobic beads do not have attractive interactions with the surface. Reflective boundary conditions at  $Z = 0$  are used to prevent the hydrophobic beads from crossing the surface. To keep the simulation volume constant, reflective boundary conditions are used for all beads for the face opposite the surface in the simulation box. The simulation box is periodic in the X and Y dimensions. The X and Y dimensions of the simulation box are kept fixed at  $20\sigma \times 20\sigma$ . The Z dimension (the dimension perpendicular to the surface) is chosen to ensure that the number density of the beads in the system is maintained at  $0.5\sigma^{-3}$ . Hence, for 400 molecules of 20mers, the Z dimension is  $40\sigma$ . The mass of each bead,  $m$ , is taken as 1 (arbitrary mass units).

### 2.2.2 Simulation Details

Langevin dynamics molecular simulations are performed at a fixed temperature of 1.0 ( temperature units,  $K_B T/\varepsilon$ ) and a damping constant of 0.1 (time units,  $(\varepsilon/m\sigma^2)^{0.5}t$ ) [56]. In order to study the role of hydrophobic character of the tails on adsorption, the LJ well-depth parameter for the interactions between the hydrophobic beads,  $\varepsilon$  is varied from 0.01 to 0.11 in a series of simulations. The rationale behind choosing these values is that for  $\varepsilon = 0.05$ , the total interaction energy between two surfactant molecules is  $O(K_B T)$ , in accordance with the observed potential of mean force between two  $\sim 1nm$  sized hydrophobic solutes. [68] The well-depth of the interaction between the surface and the polar bead,  $\varepsilon_s$  is kept at a fixed value of 5.0. This value is chosen to match the interaction energy obtained from density functional theory (DFT) calculations of polar groups on metal surfaces [69]. The bond and angle harmonic potential coefficients are

set to 100 (energy units/ $\sigma^2$ ) and 50 (energy units/ $\text{radians}^2$ ) respectively. Simulations of 20mer surfactant molecules are performed for different values of  $\varepsilon$  at a fixed monomer number density of  $0.5\sigma^{-3}$  (a 20mer molecule has one polar head bead and 19 hydrophobic tail beads). To study the effect of the size of the polar head group, three different values of polar bead's WCA length-scale parameter,  $\sigma_P : \sigma, 1.5\sigma$  and  $2\sigma$ , are chosen. The WCA well-depth parameter,  $\varepsilon_P$  is kept fixed at 1.0. Along with these simulations, Langevin dynamics simulations in the bulk (that is, in absence of a surface) is also performed in order to study bulk aggregation behavior. While the size of the polar beads is changed, their mass is kept the same. Hence, the same damping constant of 0.1 (time units) is kept in all the simulations. All simulations are performed using Large-scale Atomic/Molecular Massively Parallel Simulator (LAMMPS) MD simulations package. [70] Typically, for each simulation, the system is first equilibrated for  $3 - 8 \times 10^8$  MD steps with a time step of 0.001, followed by a production run of  $8 - 16 \times 10^8$  MD steps. Equilibration is understood to be achieved when no change in the ensemble averaged surface adsorbed amount, orientation factor (discussed below) and energy of the system is observed.

## 2.3 Results and Discussion

### 2.3.1 Effect of Tail Hydrophobicity on Adsorption Behavior

In the first set of simulations, the  $\varepsilon$  (the LJ well-depth parameter between hydrophobic beads) is varied from 0.01 to 0.09 while keeping all other parameters fixed and with  $\sigma_P = \sigma$ . By changing the value of  $\varepsilon$ , one can evaluate how the hydrophobic character of the tail affects the adsorption behavior. Figure 2.1(a) shows the number of adsorbed molecules as a function of  $\varepsilon$ . For small values of  $\varepsilon (< 0.04)$ , low levels of adsorption are observed. Above  $\varepsilon = 0.04$ , a sharp increase in equilibrium adsorption is seen, which reaches a maximum for  $\varepsilon = 0.065$ . Beyond  $\varepsilon = 0.065$ , a decrease in the equilibrium adsorption is seen. Figure 2.1(b) shows snapshots corresponding to three different  $\varepsilon$  values

(1)  $\varepsilon = 0.03$ , (2)  $\varepsilon = 0.065$ , and (3)  $\varepsilon = 0.08$ . Clearly, for  $\varepsilon = 0.03$ , the molecules adsorb in random orientations on the surface. For  $\varepsilon = 0.065$ , a self-assembled monolayer (SAM) in the adsorbed state is observed while the molecules in the bulk are randomly oriented. For  $\varepsilon = 0.08$ , the molecules aggregate in both bulk and adsorbed phases as laminar micelles. Hence, as  $\varepsilon$  is increased from 0.04 to 0.065, the adsorption regime changes from low, random adsorption to an adsorbed SAM. Beyond  $\varepsilon = 0.065$ , molecular aggregates are formed in the bulk, and the molecules do not diffuse towards the surface, thereby decreasing adsorption. Figure 2.1(c) shows radial distribution function of center of mass of the adsorbed molecules in the plane of the surface (the XY plane),  $RDF_{xy}(r)$  for  $\varepsilon = 0.065$  and  $\varepsilon = 0.03$ . The  $RDF_{xy}$  for  $\varepsilon = 0.03$  resembles that of a low density phase with no local order, while for  $\varepsilon = 0.065$ , the  $RDF_{xy}(r)$  shows regular peaks corresponding to the ordered structure of the SAM. The gradually decreasing peaks indicate that the SAM is not a solid but has fluid-like behavior.

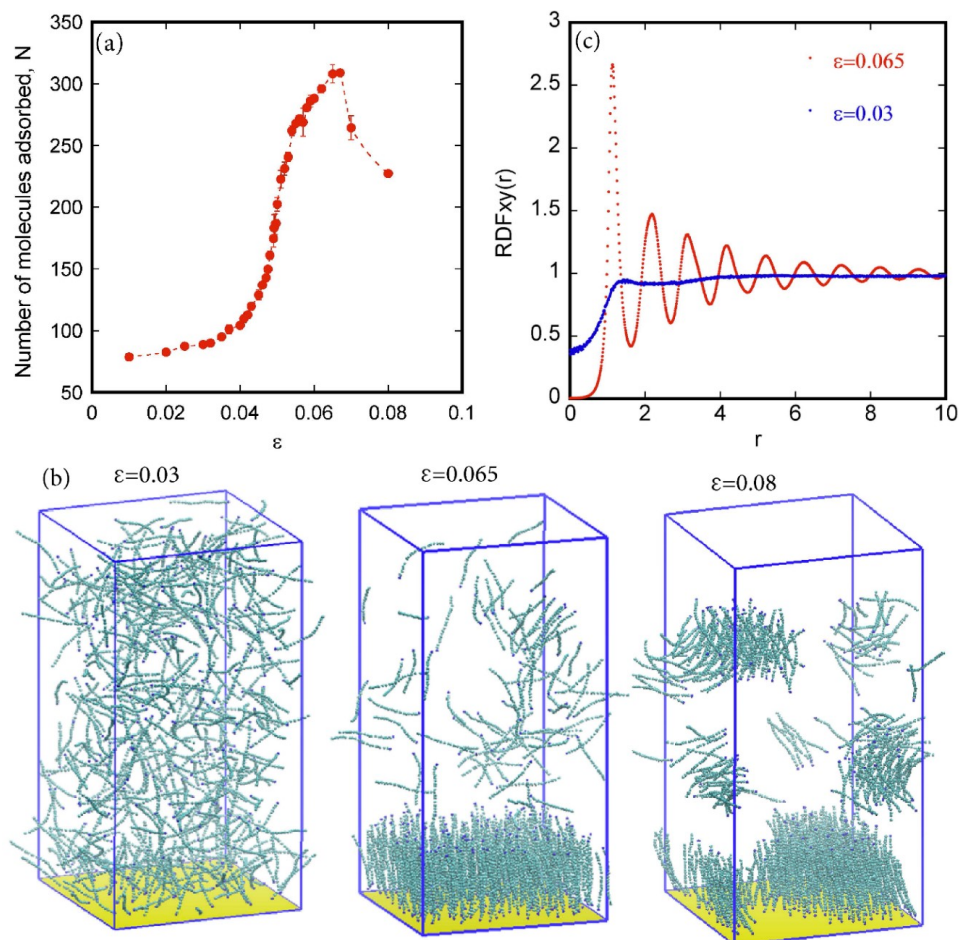


Figure 2.1: Adsorption behavior of surfactant molecules with  $\sigma_P = \sigma$ . (a) The number of adsorbed molecules,  $N$  as a function of  $\varepsilon$ . The molecules with their center of mass within a distance of  $6\sigma$  from the surface are counted as adsorbed. This criterion is based on the observed density profile of the center of mass of the molecules as a function of the distance from the surface (Figure 2.2). Error bars in this figure are standard deviations of ensemble averages calculated from 3-5 independent simulations. The line is a guide to the eye. (b) Snapshots of the system for  $\varepsilon = 0.03$  (low adsorption),  $\varepsilon = 0.065$  (self-assembled monolayer),  $\varepsilon = 0.08$  (laminar micelles in the bulk and on the surface). The surface is shown as a yellow plane. The molecules are shown as green (hydrophobic) and blue (polar) beads. (c) Radial distribution function of center of mass of the adsorbed molecules in the XY plane for  $\varepsilon = 0.03$ , which corresponds to low adsorption regime, and  $\varepsilon = 0.065$ , which corresponds to the adsorbed self-assembled monolayer.

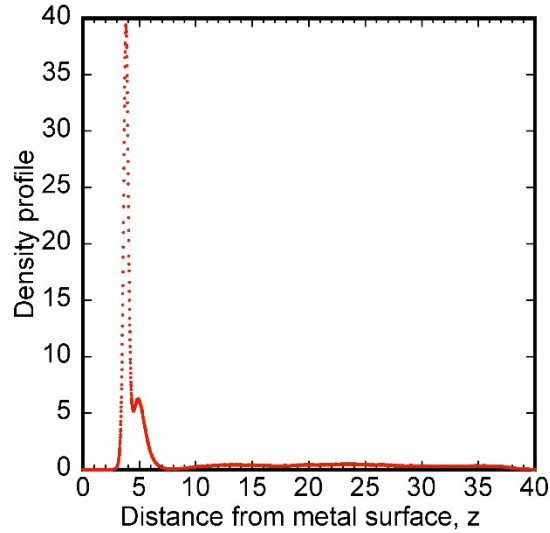


Figure 2.2: Density profile of center of mass of surfactant molecules as a function of distance from the metal surface,  $z$  for  $\sigma_p = \sigma$  and  $\varepsilon = 0.065$ .

The adsorption behavior observed above can be understood by analyzing the orientation factor of the molecules on the surface and in the bulk as a function of  $\varepsilon$  (Figure 2.3). The orientation factor,  $S$  is defined as the largest eigenvalue of the tensor  $Q$ , the elements of which are given by [71]:

$$Q_{\alpha\beta} = \frac{1.5}{N_t} \sum_{i=1}^{N_t} |n_{i\alpha} \cdot n_{i\beta}| - \frac{1}{2} \delta_{\alpha\beta} \quad (2.1)$$

where  $n_{i\alpha}$  and  $n_{i\beta}$  are the  $\alpha$  and  $\beta$  components of the end-to-end vector of the molecule  $i$  respectively.  $\delta_{\alpha\beta} = 1$  if  $\alpha = \beta$  and 0 otherwise.  $N_t$  is the total number of molecules in the system. If all the molecules are perfectly oriented parallel to each other, then  $S = 1$ . For a completely random orientation,  $S = 0.5$ .

Figure 2.3 shows  $S$  as a function of  $\varepsilon$  for bulk and adsorbed phases. For  $\varepsilon < 0.04$ ,  $S$  is small in the adsorbed phase indicating random orientation of the adsorbed molecules. For  $\varepsilon > 0.04$ , a sharp increase in the value of  $S$  in the adsorbed phase is observed. This indicates that as  $\varepsilon$  increases, the adsorbed molecules start aligning parallel (or anti-parallel) to each

other. For  $\varepsilon > 0.06$ ,  $S$  is close to 1, indicating formation of a near-perfectly aligned SAM. Interestingly, in the bulk phase, the value of  $S$  remains small up to  $\varepsilon = 0.065$ . This implies that while the molecules prefer to align parallel to each other in the adsorbed phase for  $0.04 < \varepsilon < 0.065$ , they remain randomly oriented in the bulk phase. Only for  $\varepsilon > 0.065$ , a sharp increase in the value of  $S$  in the bulk phase is observed, indicating formation of aggregates or lamellar micelles, which decreases the adsorption as seen in Figure 2.1. It is important to remember that the interaction strength between the polar beads and the surface is kept constant in these simulations. These results show that the hydrophobic interactions between surfactant tails promote adsorption and self-assembly on the surface.

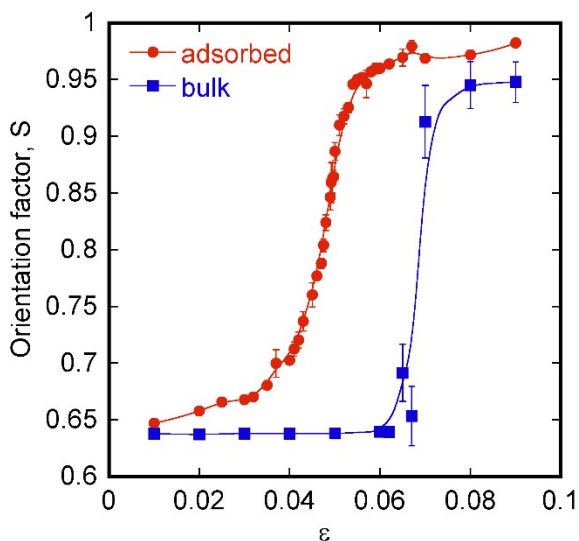


Figure 2.3: Orientation factor,  $S$  of molecules with  $\sigma_p = \sigma$  in the bulk and the adsorbed phases. A large value of  $S$  ( $\sim 1$ ) implies strong orientation of molecules parallel or antiparallel to each other. A small value of  $S$  ( $\sim 0.5$ ) corresponds to random orientation of the molecules with respect to each other. Error bars are standard deviations of ensemble averages calculated from 3-5 independent simulations. Lines are guide to the eye.

### 2.3.2 Effect of the Size of the Polar Head Group

In the next set of simulations, the size of the polar head bead,  $\sigma_p$  is increased from  $\sigma$  to  $1.5\sigma$  and  $2\sigma$  while keeping the size of the hydrophobic beads fixed at  $\sigma = 1$ . For each value of  $\sigma_p$ , the value of  $\varepsilon$  is varied as before. All other potential parameters are kept fixed.

#### 2.3.2.1 Adsorbed Amount

To understand the effect of  $\sigma_p$  on the adsorbed amount, one can naively compare the number of adsorbed molecules,  $N$  in each case (Figure 2.4(a) inset). However, this comparison will be misleading because with an increase in  $\sigma_p$ , the footprint of the molecules adsorbed with their polar bead towards the surface will be larger, and hence fewer molecules will be expected to get adsorbed. Instead, a fair comparison is to consider the fraction of the surface area covered by the molecules, or surface coverage, for different values of  $\sigma_p$ . The surface coverage is calculated as,

$$\text{surface coverage} = \frac{f\pi\sigma_p^2 + (1-f)\pi\sigma^2}{4A} \quad (2.2)$$

Where  $f$  is fraction of the adsorbed molecules with their polar head group pointing towards the surface, and  $A$  is the total surface area.

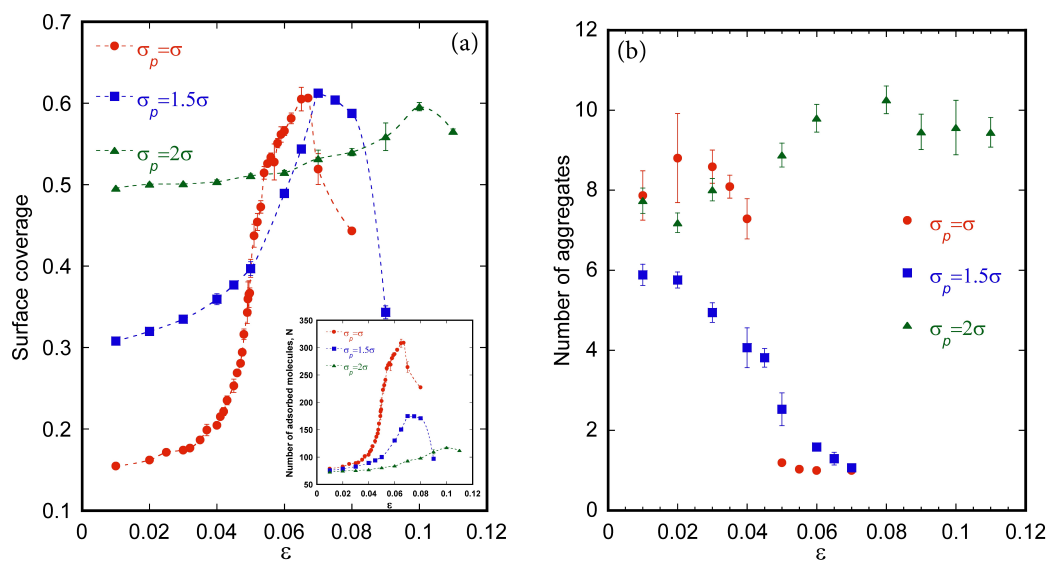


Figure 2.4: Comparison of adsorption behavior of surfactant molecules with different values of  $\sigma_p$ . (a) Surface coverage (defined in the text) as a function of  $\epsilon$ . Inset shows the number of adsorbed molecules,  $N$  for each  $\sigma_p$  as a function of  $\epsilon$ . (b) The number of aggregates of adsorbed molecules for each  $\sigma_p$  as a function of  $\epsilon$ . The aggregates are found using the 2D cluster algorithm described in the text.

Figure 2.4(a) shows surface coverage for the three values of  $\sigma_P$  as a function of  $\varepsilon$ . The low adsorption regime, observed for  $\varepsilon < 0.04$ , is dictated by attractive interactions between the polar beads and the surface, which are the same for the three values of  $\sigma_P$ . In this regime, the number of adsorbed molecules is about the same for the three cases (Figure 2.4(a) inset), and as a result, the surface coverage is highest for the largest  $\sigma_P$ . The surface coverage increases with  $\varepsilon$  for the three cases, but shows weaker dependence on  $\varepsilon$  as the value of  $\sigma_P$  increases. The maximum surface coverage, while almost invariant of the size of the polar head group, for  $\sigma_P = 2\sigma$  is observed at a higher value of  $\varepsilon$  ( $\sim 0.1$ ). Interesting differences in the nature of the adsorbed layer for the three cases explain this observation. Figure 2.4(b) shows the number of surface aggregates or 2D clusters observed for the three cases. The methodology to find 2D clusters in the adsorbed phase is similar to one employed previously [72] and is briefly described as follows: the monomers which are within a distance of  $1.5\sigma$  from the surface are projected on to the plane of the surface. The surface is divided into square boxes of length  $0.2\sigma$ . For each square box, if there exists a monomer whose surface projection is within an in-plane cut-off distance of 0.8 times  $\sigma$  (hydrophobic bead) or  $\sigma_P$  (polar bead) from the center of the square box, then the box is labeled as “occupied” or else is labeled as “vacant”. Adjacent occupied boxes are considered part of one cluster. For  $\sigma_P = \sigma$  and  $1.5\sigma$ , as  $\varepsilon$  increases, the number of surface aggregates decrease and eventually reach 1 indicating formation of a monolithic adsorbed layer. On the other hand, for  $\sigma_P = 2\sigma$ , the number of surface aggregates remain large as the  $\varepsilon$  is increased. For this case, as  $\varepsilon$  increases the adsorbed molecules tend to aggregate into cylindrical micelles (discussed below), and hence do not form a SAM as seen for smaller values of  $\sigma_P$ . We do not have a good explanation for the observed difference in the number of 2D clusters between the  $\sigma_P = \sigma$  and  $\sigma_P = 1.5\sigma$  cases for small values of  $\varepsilon$ .

### 2.3.2.2 Micelle Formation

To study the nature of aggregation of surfactant molecules in the bulk as well as in the adsorbed phase, we identify clusters of molecules using the Density-based Spatial Clustering of Applications With Noise (DBSCAN) algorithm [73]. This algorithm is useful for finding clusters in a collection of points in space. It works in the following manner: for a point  $p$ , if the number of points within a distance  $r_{cut}$  are above a cut-off value,  $N_{cut}$ , then the points are “directly reachable” to the point  $p$ . All points which are directly reachable to each other form part of a “cluster”. After identifying the clusters of monomers using the DBSCAN algorithm, we determine the size and the shape of each cluster by finding the principle eigenvalues of the radius of gyration squared tensor of each cluster. From the principle eigenvalues, the following quantities are defined [74]:

$$\text{Radius of gyration squared, } R_g^2 = \lambda_1 + \lambda_2 + \lambda_3 \quad (2.3)$$

$$\text{Asphericity, } b = [\lambda_1 - \frac{1}{2}(\lambda_2 + \lambda_3)]R_g^{-2} \quad (2.4)$$

$$\text{Acylicindricity, } c = [\lambda_2 - \lambda_3]R_g^{-2} \quad (2.5)$$

Where,  $\lambda_i$  are the eigenvalues and  $\lambda_1 > \lambda_2 > \lambda_3$  is the relative magnitude of the three eigenvalues.

A perfectly spherical cluster/micelle will correspond to  $b = 0$ . Similarly, a perfectly cylindrical cluster will correspond to  $c = 0$ . However, since even for a spherical cluster, the value of  $c$  will be close to 0, in order to classify a cluster as cylindrical, one needs to consider asphericity and acylicindricity together. Figure 2.5(a) shows asphericity and acylicindricity of the largest cluster of monomers identified for  $\sigma_P = 2\sigma$  for different values of  $\varepsilon$  in the bulk and in the adsorbed phase. In both the phases, the acylicindricity is small

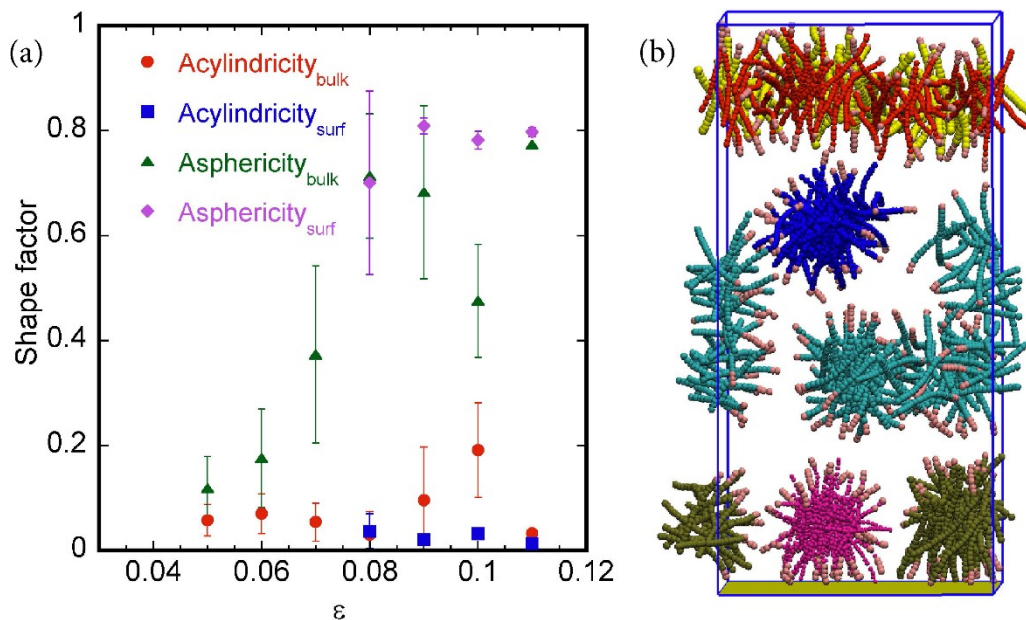


Figure 2.5: (a) Different shape factors evaluated for the largest cluster identified for molecules with  $\sigma_P = 2\sigma$  in the bulk and the adsorbed phase. (b) A snapshot of the simulation system with  $\sigma_P = 2\sigma$  and  $\varepsilon = 0.11$ . Different clusters identified by the DBSCAN algorithm are shown via different colors. Cylindrical micelles in the bulk and the adsorbed phases are clearly identifiable.

while the asphericity is large, which clearly indicates the formation of cylindrical micelles. While we focus here only on the largest cluster, similar behavior is observed for other clusters as well. Figure 2.5(b) shows a snapshot of the system for  $\varepsilon = 0.11$ . One can easily identify distinct cylindrical micelles in both the adsorbed and the bulk phases. For the case of  $\sigma_P = 1.5\sigma$ , the state of the system is more complicated. For  $\sigma_P = 1.5\sigma$ , Figure 2.6(a) and Figure 2.6(b) show asphericity and acylindricity of the largest cluster in the bulk and the adsorbed phase respectively. In both the bulk and the adsorbed phase, the acylindricity and the asphericity are similar in magnitude thereby demonstrating only a weak tendency of the molecules to form cylindrical micelles. As a result, it was not possible

to assign a distinct geometrical shape to these clusters (Figure 2.7 shows one snapshot of the system for  $\sigma_P = 1.5\sigma$  and  $\varepsilon = 0.07$ ). Note that in Figure 2.5 and Figure 2.6, no data points are shown for small values of  $\varepsilon$  for which no clusters are identified. For the case of  $\sigma_P = \sigma$ , the orientation factor,  $S$  shows formation of lamellar micelles in the bulk and the adsorbed phase. Hence, we do not evaluate acylindricity and asphericity shape factors for this case. Observation of lamellar and cylindrical micelles for the  $\sigma_P = \sigma$  and  $\sigma_P = 2\sigma$  cases respectively can be explained via calculation of Critical Packing Parameter (CPP) [75]. CPP is a dimensionless number given by  $V/(AL)$ , where  $V$  is the volume of the tail of the surfactant,  $A$  is the area of the surfactant head and  $L$  is the tail length. The CPP is calculated by assuming the tail to be a cylinder with excluded volume,  $V = \pi\sigma^2L$ , and the polar head excluded area,  $A = \pi\left(\frac{\sigma_P + \sigma}{2}\right)^2$ . For  $\sigma_P = \sigma$ , the  $CPP \sim 1$ , which suggests that the molecules will aggregate in lamellar micelles, while for  $\sigma_P = 2\sigma$ ,  $CPP \sim 0.44 < 0.5$ , which corresponds to cylindrical micelles. [75] From the above results, it is deduced that the adsorbed morphologies depend on the geometry of the surfactant molecules and correspond to bulk aggregation morphologies, a phenomenon which has been observed in AFM studies of adsorption of surfactants on surfaces [35].

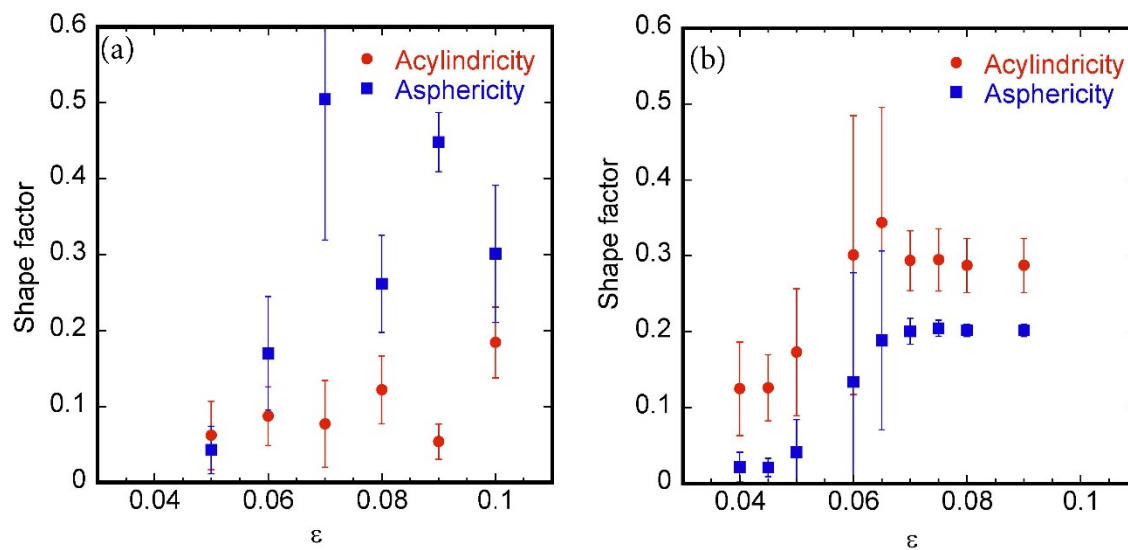


Figure 2.6: Acylindricity and asphericity of the largest cluster identified for  $\sigma_p = 1.5\sigma$  as a function of  $\varepsilon$  for (a) the bulk phase, and (b) the adsorbed phase.

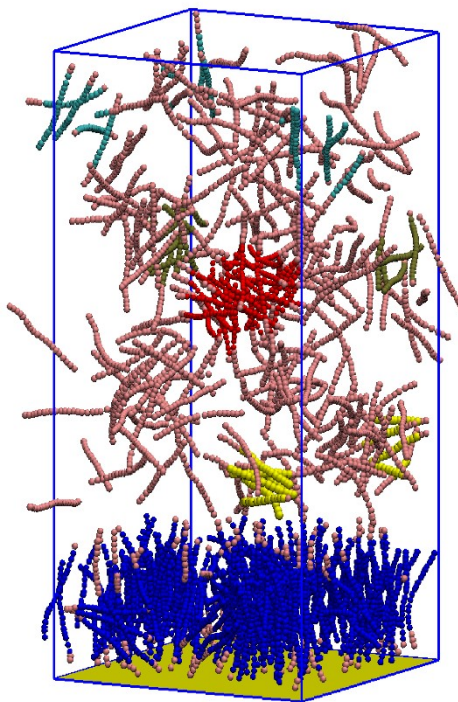


Figure 2.7: A snapshot of the simulation system for  $\sigma_p = 1.5\sigma$  and  $\varepsilon = 0.07$ . Clusters identified by the DBSCAN algorithm are shown in different colors. A monolithic adsorbed layer is seen.

### 2.3.2.3 Nature of the Adsorbed Layer

Figure 2.8 shows the fraction of adsorbed molecules with their polar head group pointing towards the surface,  $f$ , as a function of  $\varepsilon$  for the three values of  $\sigma_P$ . For small values of  $\varepsilon$  ( $< 0.04$ ) corresponding to low adsorption,  $f$  is large ( $> 0.8$ ) for all  $\sigma_P$ , as this adsorption regime is dominated by the attractive interaction between the polar head groups and the surface. For  $\sigma_P = \sigma$ , at first  $f$  increases with  $\varepsilon$  as the adsorbed molecules start aligning parallel to each other. However, beyond  $\varepsilon = 0.05$ ,  $f$  decreases with  $\varepsilon$ . The decrease in  $f$  is concomitant with the formation of a SAM. The formation of the SAM is dominated by hydrophobic interactions between the tails of the adsorbed molecules, and the polar head - surface interactions are not significant enough to cause flipping of the adsorbed molecules to have their polar beads towards the surface. Hence, the SAM (at  $\varepsilon = 0.065$ ) is patchy with  $\sim 30\%$  molecules adsorbed with their polar bead pointing away from the surface. This is an interesting revelation about the nature of the SAM, which is often presumed to form a uniformly hydrophobic layer of adsorbed surfactants. [3, 20] For  $\sigma_P = 1.5\sigma$ , a monotonic decrease in the  $f$  as a function of  $\varepsilon$  is observed. This is a consequence of geometric considerations of efficiently packing molecules with different sized polar and hydrophobic beads on the surface. For  $\sigma_P = 2\sigma$  as well, a monotonic decrease in the  $f$  as a function of  $\varepsilon$  is observed. While for  $\sigma_P = 1.5\sigma$ , a monolithic adsorbed layer is formed, for  $\sigma_P = 2\sigma$ , cylindrical micelles form in the adsorbed phase as  $\varepsilon$  increases, which results in the monotonic decrease in  $f$ . Hence, it is observed that the adsorbed layer of surfactant molecules is patchy with both hydrophobic and polar groups exposed to the solution.

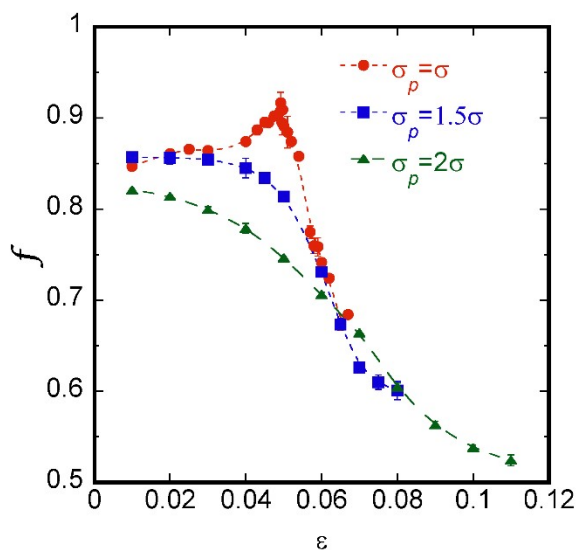


Figure 2.8: Fraction of the adsorbed surfactant molecules with their polar groups pointing towards the surface,  $f$  as a function of  $\varepsilon$  for different values of  $\sigma_p$ . Lines are guide to the eye.

While the focus of this study has been the adsorption of 20-mer surfactant molecules, the adsorption of 10-mer and 30-mer surfactant molecules were also studied. Since the bond length in the model is  $0.3\sigma$ , the length to diameter aspect ratio of 20-mer,  $l/d \sim 6$ . Whereas, for the 10-mer molecule,  $l/d \sim 3$ , which is found to be too small to form a stable, adsorbed SAM. Hence, the adsorption behavior of 10-mer surfactants is not interesting for the study of self-assembly of surfactants upon adsorption. On the other hand, 30-mer surfactant molecules show a similar adsorption behavior as the 20mer surfactant molecules (Figure 2.9). From the Figure 2.9, it is observed that for the 30-mer case, highest adsorption is achieved at a smaller value of  $\varepsilon$  ( $= 0.048$ ) as compared to the 20-mer case. This is expected as 30-mer molecules will have stronger hydrophobic attraction than the 20-mer molecules for the same  $\varepsilon$ . Furthermore, it is observed that the maximum adsorption for 30-mer molecules ( $\sim 280$ ) is less than that seen for 20-mer molecules ( $\sim 316$ ). It is believed

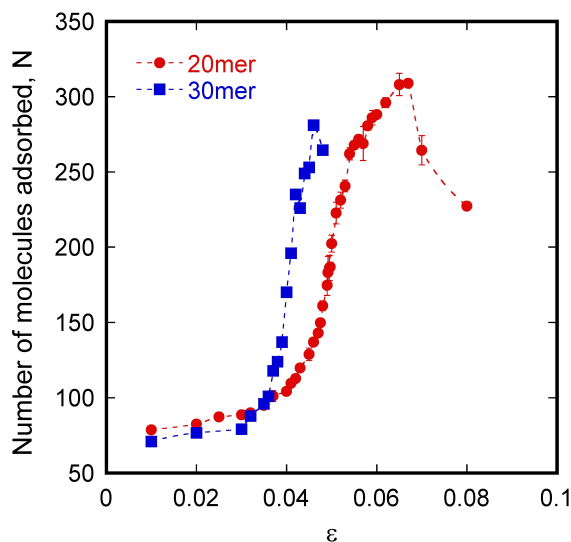


Figure 2.9: The number of adsorbed molecules,  $N$  as a function of  $\varepsilon$  for 20-mer and 30-mer surfactants with  $\sigma_p = \sigma$ .

that the origin of this difference is the larger entropy loss associated with adsorption for the 30-mer case. This aspect is currently being investigated in more detail using free energy calculations, and it will be a subject of a future publication.

### 2.3.3 Effect of the Affinity between Polar Head Group and Surface

It is found that in this system, the adsorption of corrosion inhibitor molecules occurs in three stages (Figure 2.10) [76]. In the first stage, most inhibitor molecules quickly adsorb onto the surface with their polar group towards surface. This is due to the strong interaction between surface and polar head group. In the second stage, the rate of adsorption is slower, and some molecules adsorb with their polar group pointing away from the surface. In the last stage, no further increase in the molecules adsorbed with their polar group towards surface is observed and molecules only adsorb with their polar head group pointing away

from surface. In the last stage, adsorption is driven by lateral hydrophobic interactions between the tails.

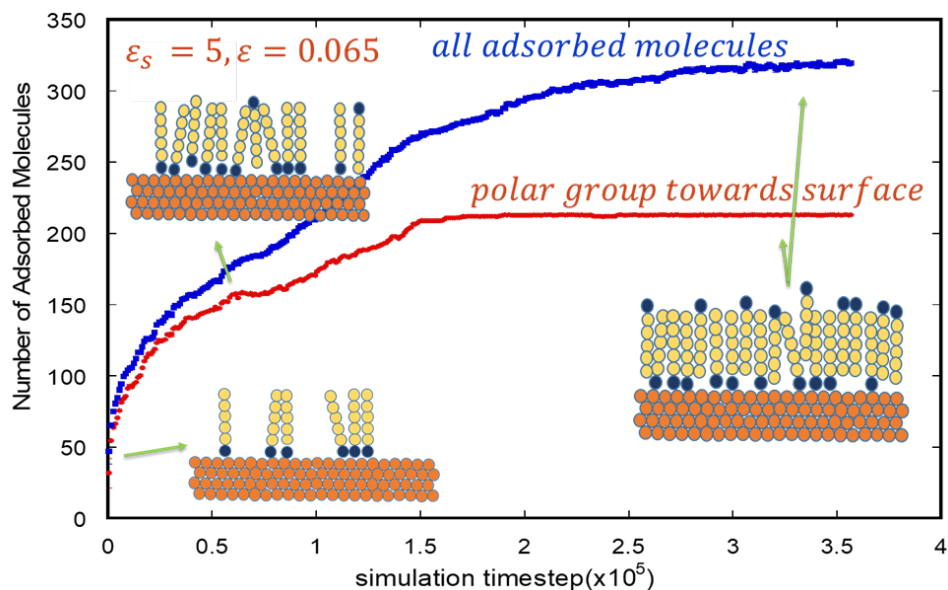


Figure 2.10: Kinetics of adsorption of corrosion inhibitor molecules. The red curve shows adsorption of molecules with their polar group towards the surface. The blue curve shows total number of adsorbed molecules. Adapted with permission from Sharma *et al.* [76].

In all the results discussed above, the affinity between the surface and the polar head group is  $\epsilon_s=5$ , which represents strong affinity between inhibitor and metal surface. To study how this affinity affects adsorption, we have varied the strength of  $\epsilon_s$  in the simulations. The interaction between the hydrophobic tails is kept at  $\epsilon=0.065$ . Figure 2.11 shows kinetics of adsorption with different values of  $\epsilon_s$ . From Figure 2.11, it is observed that upon reducing the strength of  $\epsilon_s$ , the rate of adsorption is reduced for both the first and the second stages. However, we find that the overall equilibrium adsorption amount does not vary significantly, indicating that a SAM of similar packing density is formed. This is

because the adsorption is dictated by lateral hydrophobic interactions between alkyl tails and not by the affinity of the polar group with the surface.

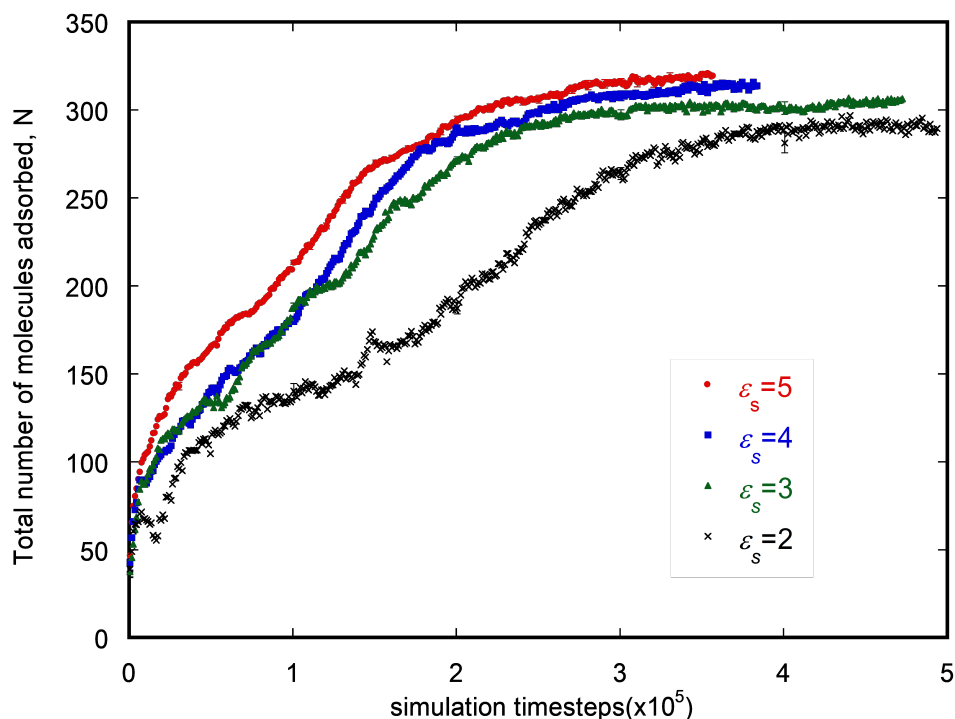


Figure 2.11: Total number of molecules adsorbed as a function of simulation time for different values of the affinity between polar head group and metal surface,  $\epsilon_s$ .

Figure 2.12 shows the number of molecules adsorbed with their polar group towards the surface as a function of time for the same simulation trajectories as in Figure 2.11. Here, it is found that the equilibrium adsorption amount is different for different values of  $\epsilon_s$ . This indicates that the affinity between the polar head group and surface changes the fraction of molecules adsorbed with polar group toward surface, and thus changes the nature of the adsorbed corrosion inhibitor film. A weaker affinity will result in less molecules adsorbed with their polar group towards surface, and thus a less hydrophobic film.

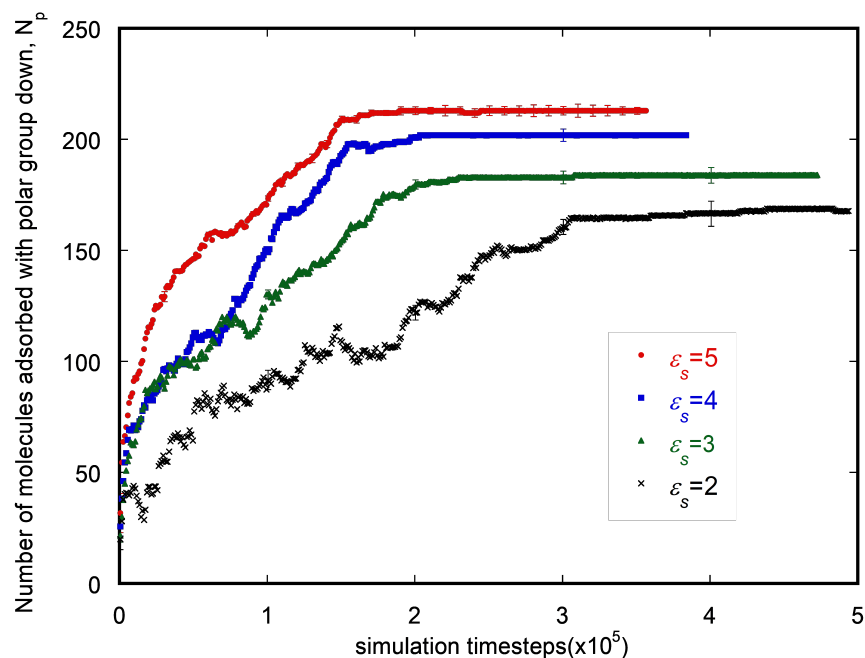


Figure 2.12: Number of molecules adsorbed with their polar group towards the surface as a function of simulation time for different values of affinity between the polar head group and metal surface,  $\epsilon_s$ .

## 2.4 Conclusions

Adsorption of surfactant molecules on metal-water interfaces is a useful mechanism for tuning interfacial properties, and has found applications in a wide range of fields. The goal of this work is to study how different molecular properties of surfactant molecules affect their adsorption characteristics. From our simulations, it is found that tail hydrophobicity plays a significant role in adsorption. When the tail is only weakly hydrophobic, only low levels of adsorption are observed even though the polar groups have strong affinity for the surface. For more hydrophobic tails, a SAM in the adsorbed phase is formed. In this regime, adsorption is dominated by hydrophobic interactions between

the tails, a phenomenon which has also been reported in experiments [69]. For surfactants with a larger polar head group than the hydrophobic monomers in the tail, the effect of tail hydrophobicity on surface coverage via adsorption is found to weaken. Nevertheless, the maximum surface coverage is found to be almost invariant of the size of the polar head group. These results explain the experimental observations wherein, for the case of small polar head groups, such as quaternary ammonium derivatives, a dramatic effect of the tail hydrophobicity on adsorption is reported, [60, 64] while for the case of bulky polar groups, such as imidazoline based groups, adsorption is found to be invariant of the tail hydrophobicity [51]. It is observed that the adsorbed surfactant layer is patchy with a good fraction of the polar groups in the adsorbed phase pointing towards the solution. This observation is contrary to the assumption that the adsorbed SAM manifests a uniformly hydrophobic interface to the solution [3, 20, 21]. It is also found that in accordance with the experimental observations, the molecules adsorb in micellar structures similar to those observed in the bulk phase [56, 77]. That is, the molecules which have tendency to form cylindrical micelles in the bulk, adsorb as cylindrical micelles rather than forming a mono/bilayer. Finally, it is found that metal-polar head group interactions change the nature of adsorbed corrosion inhibitor films. Total number of molecules adsorbed into a SAM does not change with affinity of metal surfaces and polar head group, but the overall hydrophobic character of the film decreases with decrease in the metal-polar head interaction strength. In experimental studies, the role of tail hydrophobicity is investigated by studying the adsorption behavior of surfactants with different tail lengths. Longer tails are expected to have more conformational entropy loss upon adsorption in comparison to smaller tails. Furthermore, surfactants with longer tails will have different transport and aggregation properties. In this work, the hydrophobic character of surfactant tails is changed while the tail length is fixed. This strategy may not have a direct experimental analogue, but is useful in isolating the role of hydrophobic interactions from other concomitant effects that

arise from varying the alkyl tail length. Similarly, by changing the size of the polar head group without changing its interaction strength with the surface, we study the role of polar group size in isolation of other effects. In summary, this work concludes that the nature of the hydrophobic tail and the polar head group play an important role in the adsorption characteristics of surfactant molecules, and these factors should be taken into account for rational design of these molecules for different applications.

### 3 A QUANTITATIVELY ACCURATE THEORY TO PREDICT ADSORBED CONFIGURATIONS OF LINEAR SURFACTANTS ON POLAR SURFACES<sup>4</sup>

#### 3.1 Introduction

Adsorption of surfactants on polar surfaces has numerous applications, including in corrosion inhibition[1], electrochemical reactions[3], synthesis of anisotropic metal nanoparticles[2], and heterogeneous catalysis[4]. Surfactants are known to adsorb onto polar surfaces in various morphologies, such as (hemi-) cylinders, (hemi-) spheres, or planar micelles[56, 78]. Morphology of adsorbed surfactant films is an important determinant of interfacial properties[79, 80]. An ingenious thermodynamics-based theory for predicting adsorbed morphologies of surfactants on hydrophobic and hydrophilic surfaces was introduced by Johnson and Nagarajan[81, 82]. However, it was not widely adopted because its predictions for hydrophilic surfaces did not match atomic force microscopy results and it required thermodynamic parameters like chemical potential of surfactants in different aggregation states, which are not easily obtainable from experiments or computer simulations.

Linear surfactant molecules, that is, molecules with a linear alkyl tail and a polar head group commensurate in size with an alkyl group, may adsorb as stripes with their molecular axes parallel to the surface and to each other[62, 83] or as a selfassembled monolayer (SAM) with their molecular axes perpendicular to the surface[84, 85]. However, there is no theoretical formalism for a priori predicting which configuration will be favored. Furthermore, experiments have revealed different kinetic pathways associated with the formation of a SAM of adsorbed surfactants on polar substrates like mica and gold. For instance, adsorption of octadecylphosphonic acid[86, 87] and octadecyltrimethyl

---

<sup>4</sup> Adapted with permission from Sharma, S., Singh, H., & Ko, X. (2019). A quantitatively accurate theory to predict adsorbed configurations of linear surfactants on polar surfaces. *Journal of Physical Chemistry B*, 123(34), 7464-7470. Copyright(2019) American Chemical Society.

ammonium bromide (C18TAB)[84] on mica initiates with nucleation of densely packed molecular islands followed by growth and coalescence of these islands into a contiguous adsorbed monolayer[86, 87]. The adsorption and selfassembly of alkanethiols on gold follow a different kinetic pathway. It comprises two steps: in the first step, the molecules completely cover the gold surface by adsorbing parallel to the surface in the form of stripes. The second step involves an orientational transition wherein the molecules “stand up” on the surface with their molecular axes parallel to the surface normal[88]. A similar orientational transition has been reported in other studies of alkanethiols on gold[89]. So far, there exists no theoretical basis to predict when one pathway is favored over the other.

In this work, we introduce a mathematical model to predict adsorbed configurations of linear surfactants on polar surfaces. From molecular simulations, we show that our model’s predictions are quantitatively accurate without the need of any fitting parameters. The model is based on the idea that linear surfactant molecules in the lying-down configuration maximize their interactions with the surface but also occupy a larger surface area. The standing-up configuration, on the other hand, allows more molecules to adsorb on the surface. In the lyingdown configuration, the molecules optimize their intermolecular interactions to eventually form a stripe morphology, while the standing-up configuration ultimately results in a SAM. Based on our theory, the kinetics associated with the formation of a SAM can also be predicted. The details of our theoretical model are discussed below.

### 3.2 Theoretical Model

Consider a surfactant molecule with a polar head group and an  $n$  carbon long alkyl tail. When these surfactant molecules are lying flat on a solid surface, the total interaction energy is given by

$$E^L = (\varepsilon_{HS}^L + n\varepsilon_{TS}^L) \frac{A}{A_m^L} P^L \quad (3.1)$$

where the superscript L indicates the lying-down configuration,  $\varepsilon_{HS}$  is the interaction strength of the polar head with the surface,  $\varepsilon_{TS}$  is the interaction strength of a tail group with the surface, A is the total adsorption surface area,  $A_m$  is the area occupied by one surfactant molecule, and P is the packing fraction of the molecules adsorbed on the surface. In the standing-up configuration, the total interaction energy is given by

$$E^S = \varepsilon_{HS}^S \frac{A}{A_m^S} P^S \quad (3.2)$$

The superscript S indicates the standing-up configuration. Equations 3.1 and 3.2 are applicable to surfactant molecules of any geometry.  $P^S$  can be estimated as  $P^S = N \frac{A_m^S}{A}$ , where N is the number of molecules adsorbed in the standing-up configuration. For a linear surfactant molecule, approximated as a cylinder,  $A_m^L = ld$ ,  $A_m^S = \frac{\pi d^2}{4}$  and  $P^L \approx 1$ , where  $l$  is the length and  $d$  is the diameter of the cylinder. Furthermore, if the interactions of the polar head and the tail groups are isotropic, that is, they do not depend on the adsorbed configuration, then the subscripts L and S from the interaction terms may be dropped. The ratio of eqs 3.1 and 3.2 thus becomes

$$\frac{E^L}{E^S} = \frac{\pi d}{4lP^S} \left( 1 + \frac{n\varepsilon_{TS}}{\varepsilon_{HS}} \right) \quad (3.3)$$

If the ratio  $\frac{E^L}{E^S} < 1$ , standing-up configurations are favored, which will eventually lead to formation of a SAM.

### 3.3 Simulation System and Methods

To test the validity of the theory, we have performed Langevin dynamics simulations to determine adsorbed configurations of linear surfactant molecules with different values of  $\varepsilon_{TS}$  and  $\varepsilon_{HS}$  on a polar solid surface. Surfactant molecules are modeled as linear bead-spring chains, same as in our previous study[90]. The first bead of the molecules represents the polar head group, and the remaining ones represent the alkyl tail. We have studied surfactant molecules comprising [65] beads. The interactions of the surface with the polar

head and the tail beads are modeled via 9-3 potential, which is the potential function obtained when the Lennard-Jones (LJ) potential is integrated over a semi-infinite slab. The solvent is treated implicitly in these simulations. All quantities in the simulation system are in reduced units[65]. In these units, the thermal energy  $k_B T$  is taken as the unit of energy, and thus,  $k_B T = 1$ . The interaction between any two tail beads is modeled via the LJ potential with  $\epsilon_{TT} = 0.065$  and  $\sigma = 1$ . This value of  $\epsilon_{TT}$  results in formation of a SAM for the case when there is no interaction between the alkyl tail and the surface, that is  $\epsilon_{TS} = 0.19$ . The overall hydrophobic interaction between two alkyl tails is of the order of  $k_B T$ [68]. The magnitude of  $\epsilon_{HS}$  matches binding energies between polar groups and metals determined from the density functional theory[69]. With  $\sigma$  taken as the unit of length in reduced units, the equilibrium bond length between adjacent beads is 0.3. The mass of each bead  $m$  is set to 1. In the Langevin dynamics simulations, the time step and the damping parameter are chosen to be  $0.001\sigma(m/k_B T)^{1/2}$  and  $0.1\sigma(m/k_B T)^{1/2}$ , respectively. The force constants for bond and angle harmonic potentials are  $100k_B T/\sigma^2$  and  $50k_B T/radians^2$ , respectively. These model parameters of surfactants are taken from our previous study[90]. The simulation box is periodic in the x-y directions, and the polar surface is at  $z = 0$ . The opposite face of the simulation box has an athermal surface with reflective boundary conditions for all beads. The size of the simulation box is  $20 \times 20 \times 40$ . The simulation system has 400 surfactant molecules. The initial configuration is generated by placing the surfactant molecules randomly in the simulation box. We have confirmed the invariability of our simulation results in a larger system (800 molecules with simulation box size  $20 \times 20 \times 80$ ) for some data points.

Our previous work[91] on atomistic simulations of surfactants in bulk and near metal surfaces has shown that (a) surfactant molecules form micelles with polar groups on the outside and alkyl tails in the core, implying that the alkyl tails have only weak interactions with the polar groups and (b) in infinite dilution, the surfactant molecules adsorb with their

alkyl tail lying parallel to the metal surface, suggesting that the tails have net attractive interactions with the surface. Thus, in our coarse-grained model, only excluded volume interactions between the polar heads and the alkyl tails have been considered, while the interactions between the alkyl tails and the surface are attractive.

### 3.4 Results and Discussion

#### 3.4.1 Validating the Theoretical Model

Figure 3.1 shows results of equilibrated adsorbed configurations of surfactant molecules obtained from Langevin dynamics simulations. Each data point in Figure 3.1 is from a Langevin dynamics simulation with a specific set of  $(\epsilon_{TS}, \epsilon_{HS})$  parameters. The theoretical line of  $E^L = E^S$  calculated from equation 3.3 is also shown. In equation 3.3 for 20-mer surfactants,  $l = 6$  and  $d = 1$ .  $P^S$  is calculated as  $P^S = \frac{N\pi d^2}{4A}$ , where  $N$  is the number of adsorbed molecules in the SAM. For a surface area of  $20 \times 20$ ,  $N \approx 310$ , which gives  $P^S = 0.6$ .

As per the model, when the  $\epsilon_{HS}$  is larger in magnitude (that is, more attractive) than the value corresponding to the  $E^L = E^S$  line for a given  $\epsilon_{TS}$ , the equilibrium configuration is expected to be a SAM, while below the  $E^L = E^S$  line, it is expected to be stripes. The simulation results are found to be in excellent agreement with the theoretical predictions implying that our theoretical model is quantitatively accurate. Figure 3.2 shows snapshots of two different state points. Figure 3.2a,b corresponds to  $(\epsilon_{TS}, \epsilon_{HS}) = (0.49, 3.0)$ , and Figure 3.2c,d corresponds to  $(\epsilon_{TS}, \epsilon_{HS}) = (0.55, 3.0)$ . For  $(\epsilon_{TS}, \epsilon_{HS}) = (0.49, 3.0)$ , a SAM configuration is obtained, while for  $(\epsilon_{TS}, \epsilon_{HS}) = (0.55, 3.0)$ , a stripe configuration is obtained. In the stripe configuration, the molecules stack up in multiple layers. The bottom view of the stripe configuration shows that the molecules are arranged in linear, parallel stripes. In the SAM configuration, the molecules stand up on the surface and are parallel to each other. In Figure 3.3, the density distribution of surfactant molecules is plotted as a

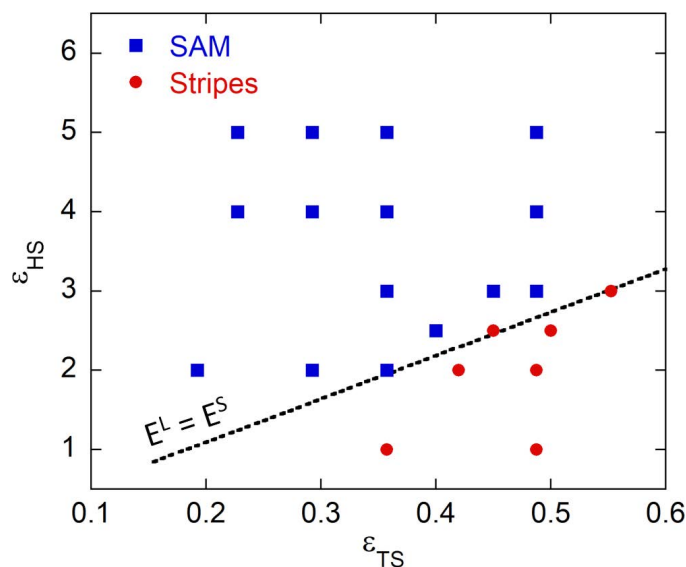


Figure 3.1: Summary of results of Langevin dynamics simulations performed for different values of  $(\epsilon_{TS}, \epsilon_{HS})$ . The dashed line shows the condition when  $E^L = E^S$ . An excellent match between the simulation results and theoretical predictions is obtained.

function of the distance  $z$  from the surface for these two equilibrium configurations. Figure 3.3a shows that the SAM configuration is predominantly a monolayer with a shoulder due to the formation of a partial second layer of adsorbed molecules. Figure 3.3b informs that, in the stripe configuration, the molecules stack up in nearly eight distinct molecular layers. Interestingly, the total numbers of adsorbed molecules in the SAM and the stripe configuration are similar, even when the adsorbed configurations are significantly different. This result suggests that adsorbed morphology cannot be conclusively deduced from the adsorbed amount alone[5].

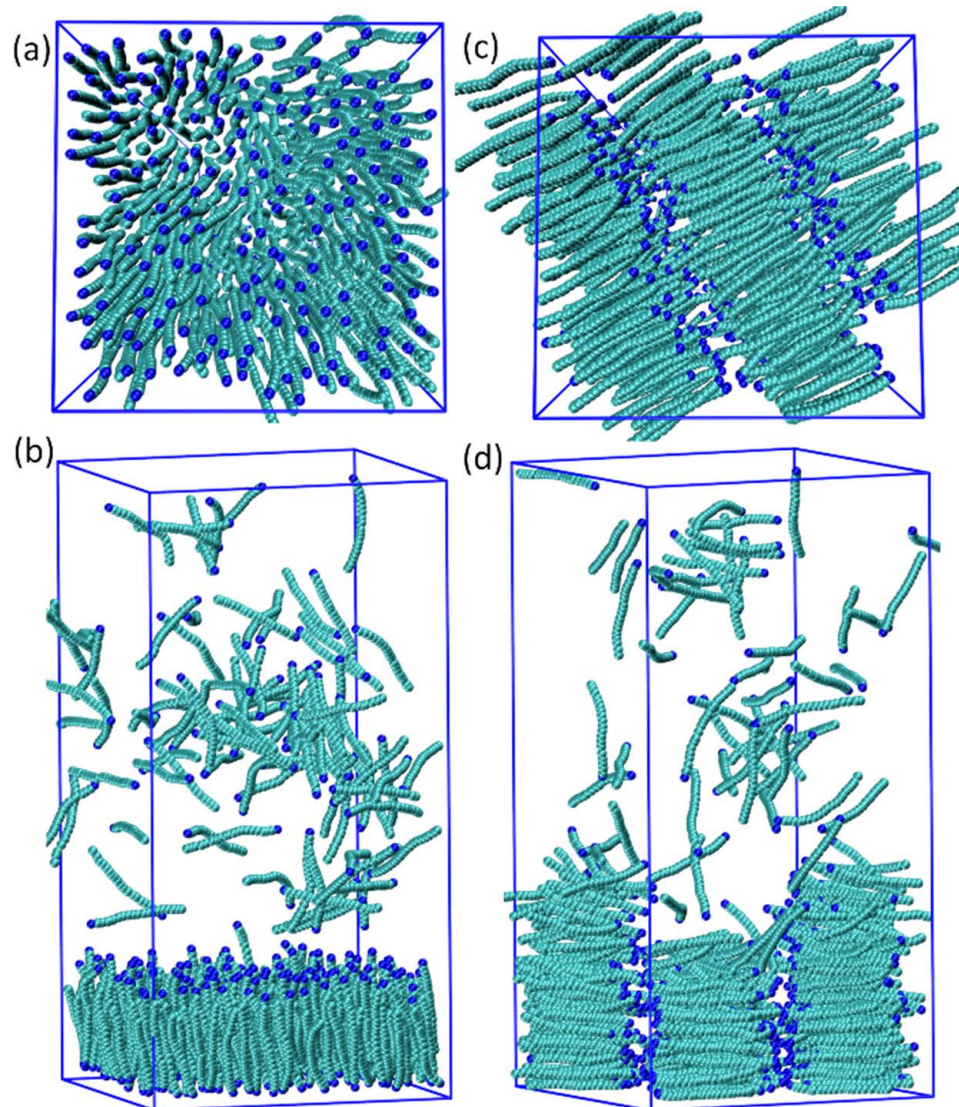


Figure 3.2: Snapshots of equilibrium configurations: (a) bottom view and (b) side view for  $(\epsilon_{TS}, \epsilon_{HS}) = (0.49, 3.0)$  showing SAM and (c) bottom view and (d) side view for  $(\epsilon_{TS}, \epsilon_{HS}) = (0.55, 3.0)$  showing stripes.

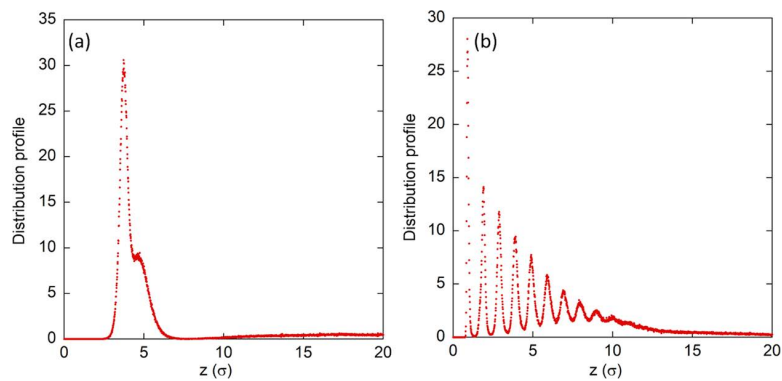


Figure 3.3: Equilibrium distribution of surfactant molecules as a function of distance from the surface  $z$  for (a)  $(\epsilon_{TS}, \epsilon_{HS}) = (0.49, 3.0)$  and (b)  $(\epsilon_{TS}, \epsilon_{HS}) = (0.55, 3.0)$ . The distribution in panel (a) shows a monolayer of adsorbed molecules standing-up on the surface with a partially formed second layer appearing as a shoulder. The distribution in panel (b) shows multilayer adsorption of surfactant molecules lying down on the surface.

### 3.4.2 Kinetics of SAM Formation

As discussed above, experiments have revealed two different kinetic pathways leading to the formation of a SAM: in the first pathway, molecules initially adsorb lying down on the surface and that is followed by an orientational transition from the stripe to the SAM configuration. In the second pathway, islands of adsorbed molecules standing up on the surface form. These islands grow and coalesce to become a SAM. Both these kinetic pathways are observed in our simulations. The stripe-to-SAM orientational transition is observed when the  $\frac{E^L}{E^S}$  is close to 1, roughly  $0.8 < \frac{E^L}{E^S} < 1$ . We illustrate this orientational transition by describing a simulation trajectory for the case  $(\epsilon_{TS}, \epsilon_{HS}) = (0.49, 3.0)$  for which the  $\frac{E^L}{E^S} = 0.9$  and it eventually forms a SAM (see Figure 3.1).

Movie S1<sup>5</sup> shows a movie of the simulation trajectory for  $(\epsilon_{TS}, \epsilon_{HS}) = (0.49, 3.0)$  in which the stripe-to-SAM orientational transition is clearly seen. For this simulation trajectory, Figure 3.4a shows the total number of surfactant molecules adsorbed,  $N$  as a function of time. The initial adsorption is rapid followed by a more gradual adsorption. Figure 4b shows the average angle of the axes of the adsorbed molecules with the surface normal  $\langle\theta\rangle$  as a function of  $N$ . During initial adsorption, the molecules lie flat on the surface as evidenced by  $\langle\theta\rangle \approx 80^\circ$ . Beyond  $N \sim 160$ , a rapid decrease in the  $\langle\theta\rangle$  is observed, indicating that the adsorbed molecules undergo an orientational transition and start standing up on the surface. The arrow in Figure 3.4a indicates the point in the trajectory when the stripe-to-SAM transition occurs. Figure 3.4c shows the fraction of the surface covered by the adsorbed molecules, *Fraction* as a function of time. To calculate *Fraction*, the surface is divided into squares of dimensions  $0.2 \times 0.2$  (length-scale is defined by  $\sigma$ , the LJ parameter of a bead of a surfactant molecule). The centers of all surfactant beads which are within a distance of  $z = 1.5$  from the surface are projected onto the plane of the surface. If the center of a square is within a distance of 0.5 from any projected center of a surfactant

<sup>5</sup> [https://pubs.acs.org/doi/suppl/10.1021/acs.jpcc.9b05861/suppl\\_file/jp9b05861\\_si\\_002.mpg](https://pubs.acs.org/doi/suppl/10.1021/acs.jpcc.9b05861/suppl_file/jp9b05861_si_002.mpg)

bead, then this square is labelled as “occupied” or else “vacant”. Fraction is defined as the fraction of occupied squares in a configuration. It is observed that Fraction  $\zeta$  0.8 is reached in a much quicker time ( $\sim 1 \times 10^4 \sigma(m/k_B T)^{1/2}$ ) than the orientational transition ( $\sim 20 \times 10^4 \sigma(m/k_B T)^{1/2}$ ) indicating that the molecules in the stripe configuration cover the entire surface before undergoing the transition. Figure 3.4d shows the distribution of  $\theta$  of adsorbed molecules at different time periods. Each time period spans  $4.3 \times 10^4 \sigma(m/k_B T)^{1/2}$ . In the  $t_1$  time period,  $N$  varies from 145 to 160; in the  $t_2$  time period,  $N$  varies from  $\sim 182$  to 190; in the  $t_3$  time period,  $N$  varies from  $\sim 220$  to 230; in the  $t_4$  time period,  $N$  varies from  $\sim 288$  to 292. In the  $t_1$  period, the distribution of  $\theta$  is predominantly around  $80^\circ$  indicating that the adsorbed molecules lie flat on the surface. The period  $t_2$  shows initiation of the orientational transition with the peak around  $80^\circ$  becoming shallower and a bump appearing near  $20^\circ$ . In the period  $t_3$ , the peak in the distribution of  $\theta$  is shifted to  $20^\circ$  indicating that the molecules now stand up on the surface. In the period  $t_4$ , the distribution of  $\theta$  is sharper and the peak is shifted to  $12^\circ$ , which is the case when the entire surface is covered with a SAM of adsorbed molecules.

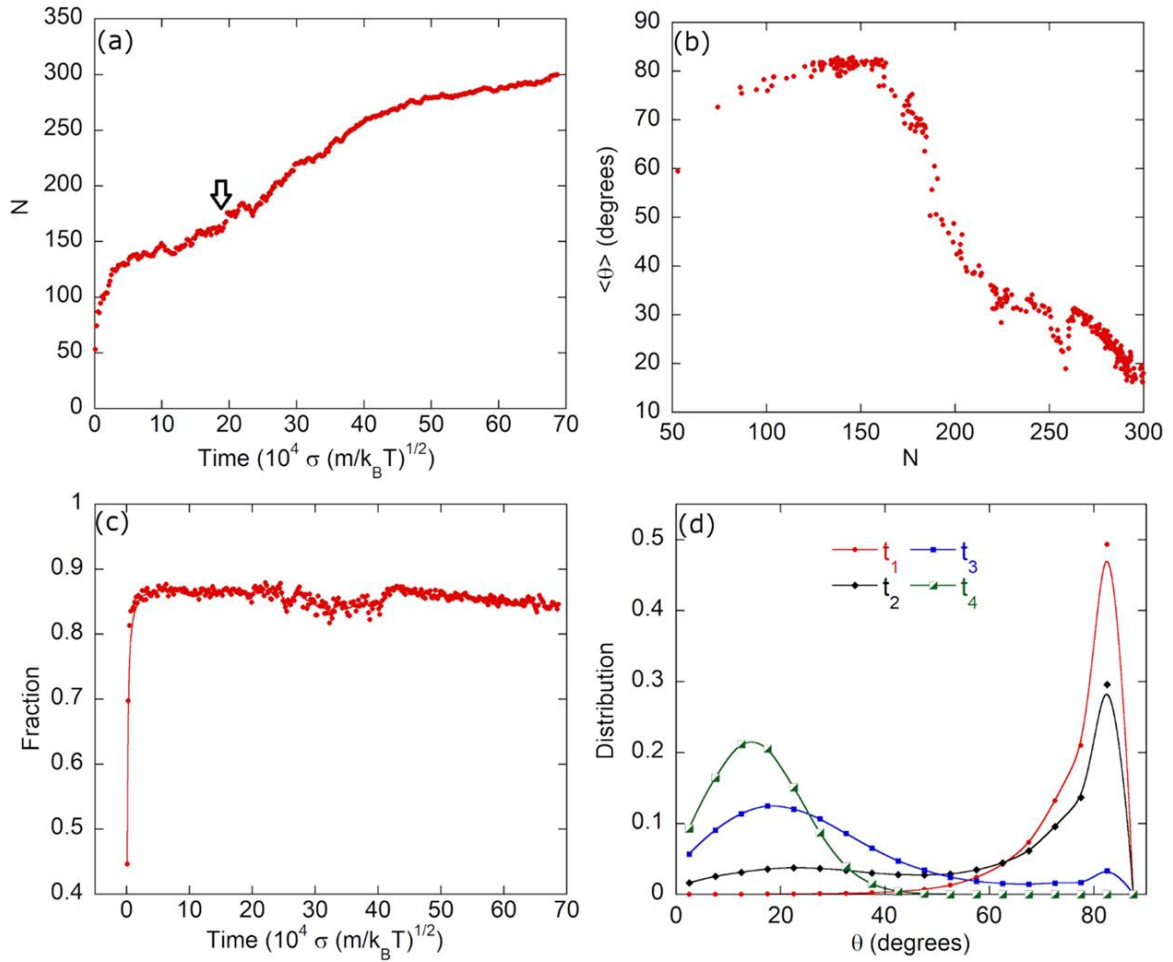


Figure 3.4: A simulation trajectory with  $(\epsilon_{TS}, \epsilon_{HS}) = (0.49, 3.0)$ . (a) Total number of adsorbed molecules,  $N$  as a function of time. (b) Average angle that the axes of adsorbed molecules make with the surface normal  $\langle \theta \rangle$  as a function of  $N$ . (c) Fraction of the surface covered with the adsorbed molecules, Fraction as a function of time. (d) Distribution of angles,  $\theta$  that adsorbed molecules make with the surface normal for different time periods ( $t_4 > t_3 > t_2 > t_1$ , see text).

The second kinetic pathway, in which islands of molecules are formed that coalesce into a SAM, is observed when  $\frac{E^L}{E^S} < 0.6$ . Figure 3.5 shows details of such a simulation trajectory for  $(\epsilon_{TS}, \epsilon_{HS}) = (0.36, 5.0)$ . For this case,  $\frac{E^L}{E^S} = 0.53$ . The  $\langle \theta \rangle$  is found to

decrease with  $N$  indicating that the adsorbed molecules are standing up on the surface (Figure 3.5b). The *Fraction* saturates to 0.9 (complete coverage) much more sluggishly (only after  $25 \times 10^4 \sigma(m/k_B T)^{1/2}$  time steps) showing that there are islands of adsorbed molecules as well as a bare, exposed surface (Figure 5c). Figure 5d shows distributions of  $\theta$  at different times. During the first time period  $t_1$  where the  $N$  varies from 40 to 140, the distribution has a peak at  $30^\circ$ , indicating that the molecules are already standing up on the surface. The peak at these small values of  $\theta$  becomes sharper as more adsorption occurs. Basically, when  $E^L \ll E^S$ , the molecules have a strong tendency to stand up in the adsorbed state, which leads to the formation of islands and a stripe configuration does not form.

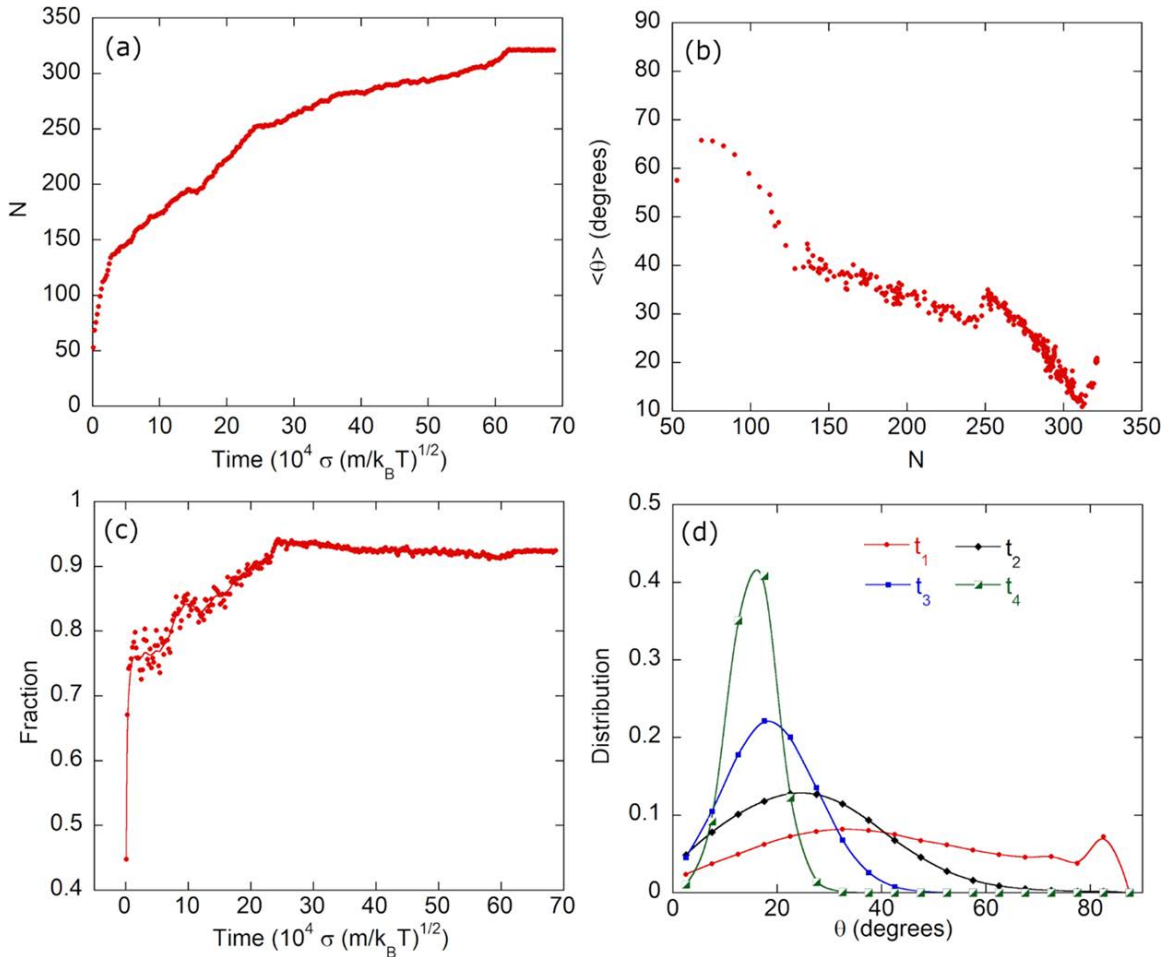


Figure 3.5: Results of a simulation trajectory with  $(\varepsilon_{TS}, \varepsilon_{HS}) = (0.36, 5.0)$ . In this trajectory, a SAM configuration is achieved via formation of islands of standing-up adsorbed molecules. (a)  $N$  as a function of time. (b)  $\langle \theta \rangle$  as a function of  $N$ . (c) Fraction as a function of time. (d) Distribution of  $\theta$  for different time periods ( $t_4 > t_3 > t_2 > t_1$ ). Each time period spans  $4.3 \times 10^4 \sigma (m/k_B T)^{1/2}$  time.  $t_1$  corresponds to the period when  $N$  varies from 40 to 140,  $t_2$  corresponds to  $N$  from 205 to 235,  $t_3$  corresponds to  $N$  from 280 to 290, and  $t_4$  corresponds to  $N$  from 319 to 322.

Figure 3.6 shows a simulation trajectory for  $(\varepsilon_{TS}, \varepsilon_{HS}) = (0.49, 2.0)$  for which the stripe configuration is achieved. Figure 3.7 shows a simulation trajectory for  $(\varepsilon_{TS}, \varepsilon_{HS}) = (0.4, 2.5)$ , which is another example of a stripe-to-SAM transition.

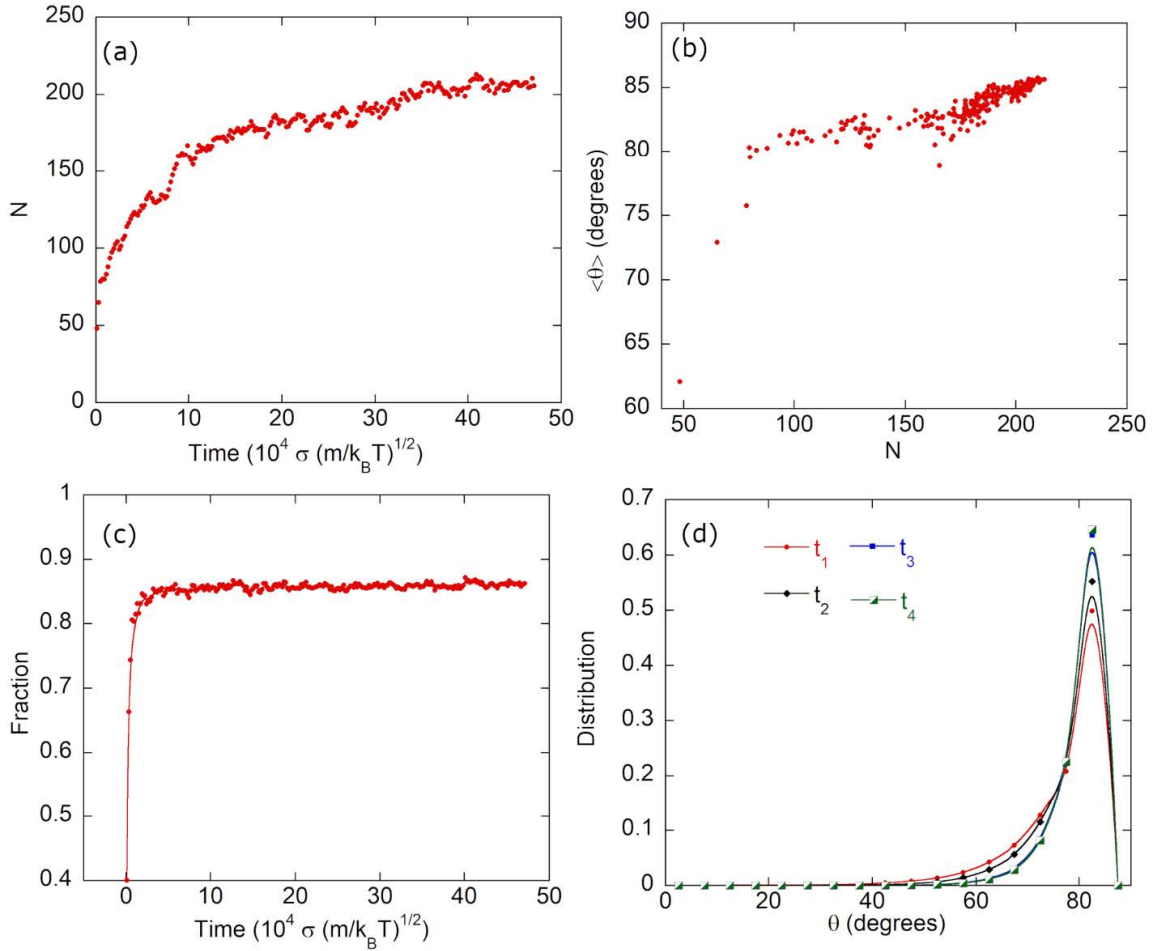


Figure 3.6: Results of a simulation trajectory with  $(\varepsilon_{TS}, \varepsilon_{HS}) = (0.49, 2.0)$ . In this trajectory, a stripe configuration is eventually formed. (a) Total number of adsorbed molecules,  $N$  as a function of time. (b) Average angle that the axes of adsorbed molecules make with the surface normal,  $\langle\theta\rangle$  as a function of  $N$ .  $\langle\theta\rangle$  increases with  $N$  indicating formation of the stripe configuration. (c) Fraction of the surface covered with the adsorbed molecules, Fraction as a function of time. The maximum surface coverage is very quickly attained. (d) The distribution of angles,  $\theta$  that adsorbed molecules make with the surface normal for different time periods ( $t_4 > t_3 > t_2 > t_1$ ). Each time period spans  $4.3 \times 10^4 \sigma (m/k_B T)^{1/2}$  time.  $t_1$  corresponds to the period when  $N$  varies from 120 to 155,  $t_2$  corresponds to  $N$  from 175 to 185,  $t_3$  and  $t_4$  correspond to  $N$  fluctuating around 205. The distribution is always peaked near  $80^\circ$  showing that the adsorbed molecules remain lying-down on the surface.

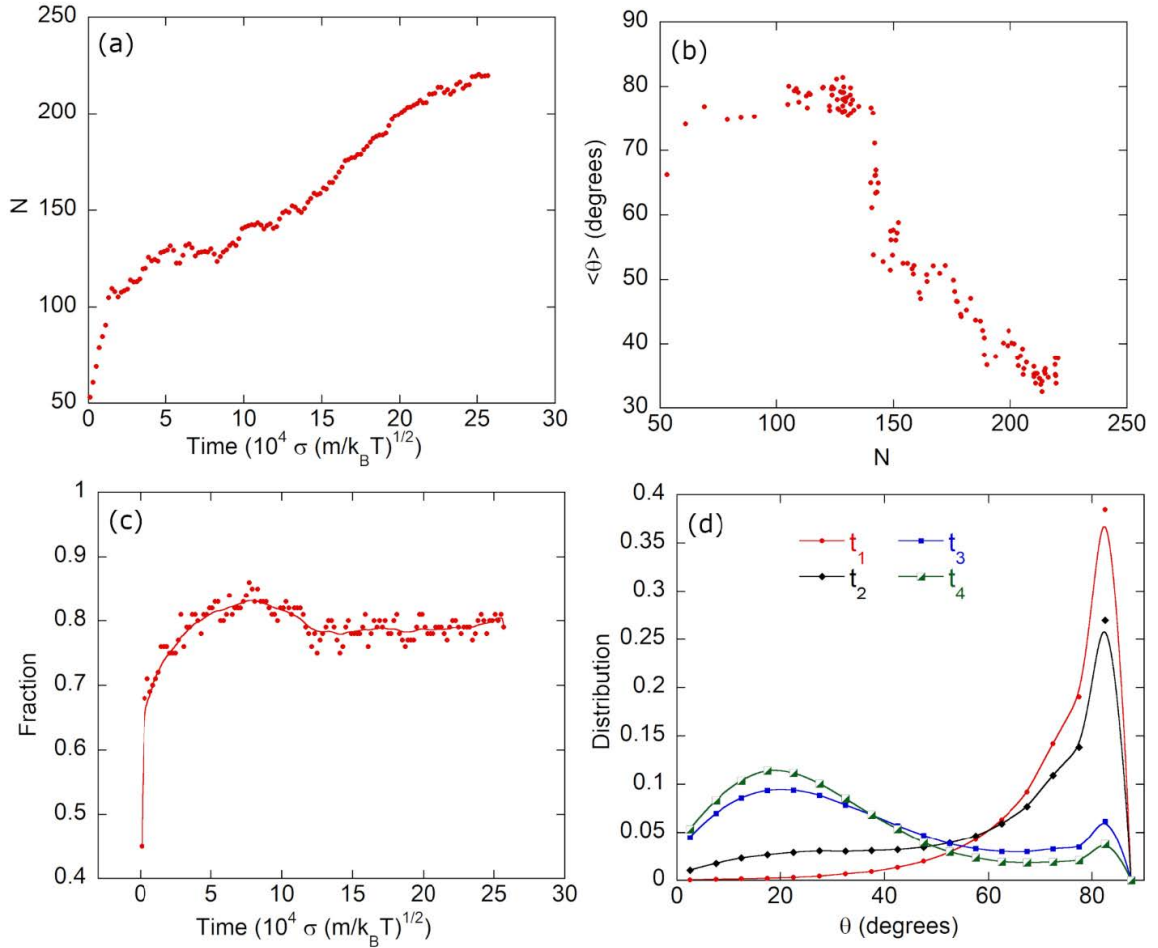


Figure 3.7: Results of a simulation trajectory with  $(\varepsilon_{TS}, \varepsilon_{HS}) = (0.4, 2.5)$ . In this trajectory, a stripes-to-SAM orientation transition is observed. (a)  $N$  as a function of time. (b)  $\langle\theta\rangle$  as a function of  $N$ .  $\langle\theta\rangle$  starts to decrease after  $N \sim 140$ , indicating the initiation of stripe-to-SAM transition. (c) Fraction as a function of time. Maximum surface coverage is attained before the stripe-to-SAM transition occurs. (d) The distribution of  $\theta$  for different time periods ( $t_4 > t_3 > t_2 > t_1$ ). Each time period spans  $4.3 \times 10^4 \sigma (m/k_B T)^{1/2}$  time.  $t_1$  corresponds to the period when  $N$  varies from 122 to 132,  $t_2$  corresponds to  $N$  from 130 to 150,  $t_3$  corresponds to  $N$  from 180 to 205, and  $t_4$  corresponds to  $N$  from 205 to 220. The shift in the peak of the distribution from  $80^\circ$  to  $20^\circ$  is observed, which is a signature of the stripe-to-SAM transition.

### 3.4.3 Validating the Theoretical Model for 30-Mer Surfactants

We have tested our theoretical model on 30 bead long linear surfactant molecules by performing Langevin dynamics simulations for two state points  $(\varepsilon_{TS}, \varepsilon_{HS}) = (0.4, 4.0)$  and  $(\varepsilon_{TS}, \varepsilon_{HS}) = (0.5, 4.0)$ . For this system,  $\sigma = 1$ ,  $d = 1$ , and  $l = 9$ . Following the above strategy, we set  $\varepsilon_{TT} = 0.046$ , which has been shown to result in maximal adsorption when the tail-surface interactions are zero.[90] Figure 3.8 shows the kinetics of adsorption for  $(\varepsilon_{TS}, \varepsilon_{HS}) = (0.4, 4.0)$  wherein a SAM is formed. The adsorption is observed to be sluggish as compared to the 20-mer case (Figure 3.8a). The maximum adsorbed amount is  $N \sim 200$ , which corresponds to  $P^S = 0.4$ . From equation 3.3,  $\frac{E^L}{E^S} = 0.87$  for  $(\varepsilon_{TS}, \varepsilon_{HS}) = (0.4, 4.0)$  suggesting that the preference is to form a SAM. For  $(\varepsilon_{TS}, \varepsilon_{HS}) = (0.5, 4.0)$ , equation 3.3 gives  $\frac{E^L}{E^S} = 1.03$ , indicating that a stripe configuration should form, which is indeed the case (Figure 3.9). The  $N$  as a function of time is plotted in Figure 3.8a. The arrow indicates when the stripe-to-SAM orientational transition is observed. The stripe-to-SAM transition corresponds to a decrease in the  $\langle \theta \rangle$  (Figure 3.8b). Figure 3.8c shows that the *Fraction* becomes greater than 0.8 within  $1 \times 10^4 \sigma(m/k_B T)^{1/2}$  time, which is much earlier than the stripe-to-SAM transition time indicating that the stripe configuration occupies the entire adsorbing surface. The distribution of  $\theta$  at different times during the adsorption is displayed in Figure 3.8d. The behavior of the distribution is similar to that in Figure 3.4d. At time  $t_1$  (corresponding to  $N \sim 110 - 122$ ), the distribution is peaked at  $\sim 80^\circ$ , which implies the presence of the stripe configuration. At  $t_2$  ( $N \sim 132 - 146$ ), there are peaks at  $\sim 30^\circ$  and  $\sim 80^\circ$  suggesting that the configuration is in the midst of the stripe-to-SAM transition. At times  $t_3$  ( $N \sim 166 - 176$ ) and  $t_4$  ( $N \sim 200$ ), the peak in the distribution is closer to  $\sim 30^\circ$  since a SAM configuration has formed. These results confirm the applicability of our theoretical model to surfactants of different alkyl tail lengths.

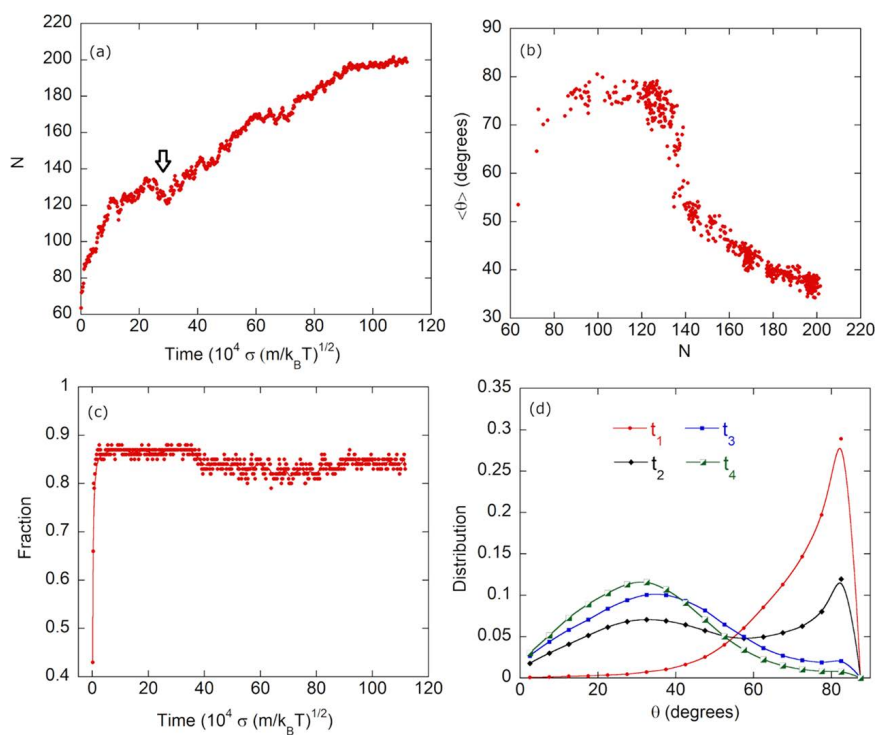


Figure 3.8: A simulation trajectory of 30-mer surfactant molecules with  $(\epsilon_{TS}, \epsilon_{HS}) = (0.4, 4.0)$ . (a)  $N$  as a function of time. (b)  $\langle \theta \rangle$  as a function of  $N$ . (c) Fraction as a function of time. (d) Distribution of  $\theta$  for different time periods  $t_4 > t_3 > t_2 > t_1$ , see text).

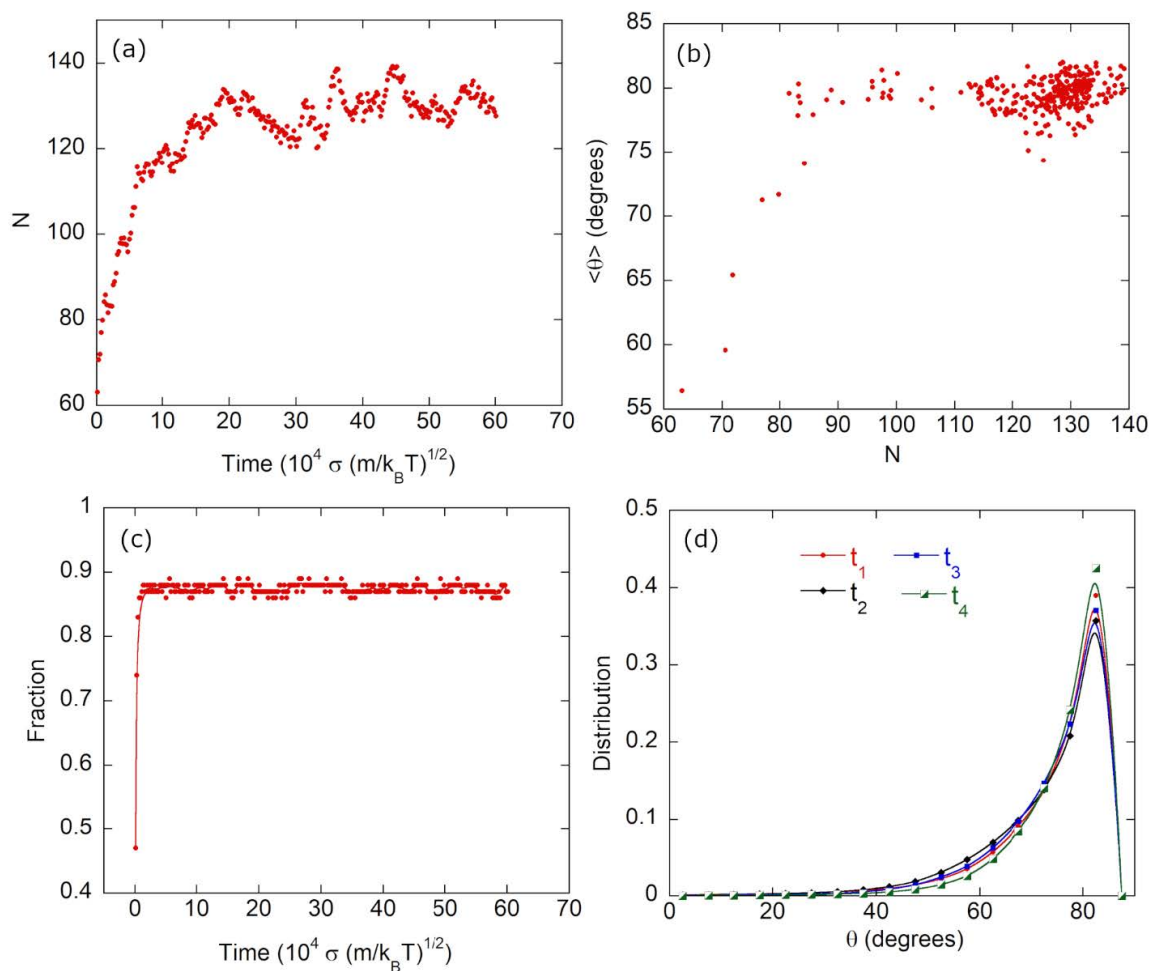


Figure 3.9: A simulation trajectory for 30-mer surfactant molecules with  $(\epsilon_{TS}, \epsilon_{HS}) = (0.5, 4.0)$  is shown. A stripe configuration is eventually formed. (a)  $N$  as a function of time. (b)  $\langle \theta \rangle$  as a function of  $N$ .  $\langle \theta \rangle$  increases with  $N$  indicating formation of the stripe configuration. (c) Fraction as a function of time. Maximum surface coverage is quickly attained. (d) The distribution of  $\theta$  for different time periods ( $t_4 > t_3 > t_2 > t_1$ ). Each time period spans  $4.3 \times 10^4 \sigma (m/k_B T)^{1/2}$  time. The distribution is always peaked near  $80^\circ$  showing that the adsorbed molecules remain lying-down on the surface.

### 3.4.4 Conditions for Validity of our Theoretical Model

Conditions for Validity of our Theoretical Model. We have provided a theoretical framework to predict equilibrium adsorbed configurations of linear surfactant molecules on polar surfaces. Our theory only considers energetic terms but ignores entropic changes during adsorption. Therefore, we would expect this theory to be valid for cases where significant adsorption, resulting in complete surface coverage, is observed. In cases of partial adsorption, a balance of the entropic and energetic terms between the bulk and adsorbed states is expected to exist, and our theory will fail to explain these scenarios. Furthermore, even though tail-tail interactions do not enter in our equations, our theory is expected to be applicable for cases where these interactions are significant so that stable SAM and stripe configurations are formed. While these conditions are the limits on the applicability of our theory, it still encompasses a large number of systems of interest, such as surfactants adsorbing on metal and polar surfaces in aqueous media.

In this work, the theoretical model is validated by performing implicit solvent Langevin dynamics simulations of a coarse-grained model of surfactant molecules. This system was selected because of its computational efficiency, which allowed us to sample numerous data points that were needed for proper validation of the model. Even with this coarse-grained description, the self-assembly of surfactants in organized layers was found to be a slow process, as can be seen from the kinetic results. Explicit treatment of water will have an effect on the adsorption behavior. Water adsorbs in layers on metal and polar surfaces and solvates polar heads of the surfactants[91]. As a result, along with direct interactions between the surfactants and the surface, there will be indirect, water-mediated interactions as well. For applying our theoretical model to a fully atomistic simulation, we will need to include these interactions by calculating the potential of mean force between different species. Furthermore, the presence of water may present free energy barriers to adsorption[91], which may affect the diffusion of surfactants toward the surface. The

application of our theoretical model on a fully atomistic system will be a subject of future research.

### 3.5 Conclusions

A theoretical model for predicting adsorbed configurations of linear surfactant molecules on polar surfaces have been developed. The predictions of the model have been validated by performing Langevin dynamics simulations. The model also shows that the ratio of energies associated with the lying down and standing-up configurations,  $\frac{E^L}{E^S}$  is a good indicator for predicting the kinetic pathway associated with SAM formation. In future work, this model will be extended for different surfactant geometries and anisotropic interactions.

## 4 A QUANTITATIVELY ACCURATE THEORY TO PREDICT ADSORBED CONFIGURATIONS OF ASYMMETRIC SURFACTANT MOLECULES ON POLAR SURFACES<sup>6</sup>

### 4.1 Introduction

Adsorption of surfactants on metal surfaces is useful in many applications, including inhibition of corrosion in oil and gas pipelines [92], modulating electrochemical reactions [3], tuning selectivity of chemical reactions [4] and synthesis of anisotropic metal nanoparticles of desired shapes and sizes [2]. The adsorption mechanism can be thought of as comprising of two processes: the diffusion of surfactants towards the surface, and the organization of adsorbed molecules. Surfactants aggregate as micelles above the critical micelle concentration (CMC), and experiments report a change in the adsorption kinetics above and below the CMC [93]. These results are rationalized via atomistic simulations that have shown that surfactant micelles have a free energy barrier to adsorption on metal surfaces, which is absent in the case of unaggregated molecules [76, 91, 94]. Upon adsorption, surfactant molecules are understood to organize themselves in various structures or morphologies, including planar films [20, 88], (hemi-) cylinders and (hemi-) spheres [56, 61, 62]. These morphologies are expected to affect the interfacial properties differently [14]. Therefore, understanding the factors that result in the formation of different adsorption morphologies will be useful for the purpose of rational design of surfactants for specific applications. A pioneering work focused on predicting the morphologies of adsorbed surfactants via macroscopic thermodynamic theory has been done by Nagarajan and coworkers [81, 82]. However, an encompassing theoretical framework that is able to

---

<sup>6</sup> Adapted with permission from Ko, X., & Sharma, S. (2020). A Quantitatively Accurate Theory to Predict Adsorbed Configurations of Asymmetric Surfactant Molecules on Polar Surfaces. *Journal of Physical Chemistry B*, 124(26), 5517-5524. Copyright(2020) American Chemical Society.

predict adsorbed morphologies of surfactants on polar surfaces directly from molecular properties and surfactant-surface interactions has not been established.

Experiments have shown that the organization of adsorbed surfactants on polar surfaces can occur via different kinetic pathways. The first kind of pathway, as reported for the adsorption of alkanethiols on gold [88, 89], comprises of two steps. In the first step, the molecules adsorb by lying flat with their axis parallel to the surface to form a stripes-like configuration. This is followed by an orientational transition wherein the molecules stand up on the surface, allowing for more molecules to adsorb [88, 89]. The second kind of pathway, for instance reported for the adsorption of octadecylphosphonic acid [86, 87] and octadecyltrimethyl ammonium bromide ( $C_{18}TAB$ )[84] on mica, involves nucleation of densely packed molecular islands on the surface. As the adsorption proceeds, these islands grow and coalesce to form a contiguous layer on the surface.

In our previous work, we developed a theoretical model for predicting adsorbed configurations of linear surfactant molecules on polar surfaces [95]. We demonstrated, via molecular simulations, that our theoretical model is quantitatively accurate in its predictions. However, an outstanding question remained if our model can be extended to asymmetrical surfactant molecules that form more complex, non-planar adsorption morphologies. In this work, we extend our theoretical model to asymmetric surfactant molecules that have a linear alkyl tail but the size of their polar head is larger than that of the alkyl groups. We have shown previously that such asymmetric surfactant molecules aggregate and adsorb in cylindrical and spherical morphologies on polar surfaces [95]. The basic principle behind our theoretical model is that upon adsorption, the most energetically favorable morphology is attained, which depends on the relative strength of interactions between the polar head and the alkyl tail with the surface. If the alkyl tails have appreciable affinity for the surface, then the molecules adsorb by “lying-down” on the surface. However, such a configuration occupies a larger surface area. Whereas,

a “standing-up” configuration with only the polar group in contact with the surface will allow more molecules to adsorb on the surface. Thus, by comparing the overall energetics associated with the two configurations that cover the entire adsorbing surface, one can predict the favorable adsorbed configuration in different cases [95]. In the case of asymmetric surfactant molecules, the standing-up configuration results in morphologies with signatures of full cylinders and the lying-down configuration shows signatures of partial spheres. In this chapter, we first describe our theoretical model and then discuss results of the simulations performed to check the validity of the model.

## 4.2 Theoretical Model

Consider a surfactant molecule with a polar head of size  $\sigma_p$  and comprising of  $n$  alkyl groups in the tail, with each alkyl group of size  $\sigma$ . Let  $\varepsilon_{HS}^S$  and  $\varepsilon_{TS}^S$  denote the interaction strengths of the polar head group ( $H$ ) and an alkyl tail group ( $T$ ) with the surface respectively in the standing-up ( $S$ ) configuration.  $\varepsilon_{HS}^L$  and  $\varepsilon_{TS}^L$  are analogously defined for the lying-down ( $L$ ) configuration. Let  $l$  be the length of the alkyl tail. For a configuration of molecules standing-up on the surface, the energy is given by,

$$E^S = \varepsilon_{HS}^S P^S \frac{A}{A_m^S} \quad (4.1)$$

Where,  $P^S$  is the packing fraction of the molecules adsorbed on the surface,  $A$  is the total area of the surface and  $A_m^S$  is the area occupied by a molecule in the standing-up configuration.  $P^S$  is given by,

$$P^S = N^S \frac{A_m^S}{A} \quad (4.2)$$

Where,  $N^S$  is the number of molecules adsorbed in the standing-up configuration. The energy associated with the lying-down configuration is given by,

$$E^L = (\varepsilon_{HS}^L + n\varepsilon_{TS}^L) P^L \frac{A}{A_m^L} \quad (4.3)$$

Where,  $P^L$  is the packing fraction of the adsorbed molecules and  $A_m^L$  is the area occupied by a molecule in the lying-down configuration.  $P^L$  is given by,

$$P^L = \frac{N^L A_m^L}{A} \quad (4.4)$$

Where,  $N^L$  is the number of molecules in the lying-down configuration in the first adsorbed layer on the surface. Area occupied per molecule in the two configurations can be calculated from the geometry of the molecule,

$$A_m^S = \pi \left( \frac{\sigma_p}{2} \right)^2 \quad (4.5)$$

$$A_m^L = l\sigma + \pi \left( \frac{\sigma_p}{2} \right)^2 \quad (4.6)$$

If the interactions of the polar head and the alkyl tail groups with the surface are independent of the adsorbed configuration, then the subscripts  $L$  and  $S$  can be dropped from the interaction energy terms. In that case, the ratio of energies in the two configurations is given by,

$$\frac{E^L}{E^S} = \frac{(\varepsilon_{HS} + n\varepsilon_{TS}) P^L A_m^S}{\varepsilon_{HS} P^S A_m^L} \quad (4.7)$$

Thus, the equilibrium adsorbed configuration depends on the strength of interactions of the polar head and the alkyl tail with the surface, as well as the molecular geometry. The model predicts that when  $E^L > E^S$ , the lying-down configuration is preferred over the standing-up configuration and *vice versa*. This theoretical model is valid under the conditions that the adsorption is strongly favored. So, one would expect the surface to be maximally covered and  $P^L \approx P^S$ . With the assumption that  $P^L \approx P^S$ , equation .4.7 can be

applied without determining the equilibrium number of adsorbed molecules per unit area, and thus precludes the need to fit any data to the model to make predictions. It should be noted that since our theoretical model is only based on molecular geometry, it does not require quantities needed to describe geometrical shapes of the adsorbed morphologies, unlike in previous works[81, 82]. So, while our theoretical model does not attempt to predict the overall adsorbed morphologies directly, it explains the configurations that are attained by individual adsorbing molecules, which in turn manifest different adsorbed morphologies.

### 4.3 Simulation System and Methods

To test the validity of our theoretical model, we have performed Langevin dynamics simulations of adsorption of asymmetric surfactant molecules on polar surfaces. Surfactant molecules are represented by a coarse-grained bead-spring model employed previously [90, 95], wherein the first bead represents the polar head group and the remaining beads represent the alkyl tail. The size of the polar head bead is taken as twice that of an alkyl bead, that is  $\sigma_P = 2\sigma$ . The alkyl tail is represented by  $n = 19$  alkyl beads connected to each other via harmonic bond and angle potentials with the equilibrium bond length of  $0.3\sigma$  and the equilibrium angle of  $180^\circ$ . The polar head bead is connected to the alkyl tail with a harmonic bond potential of equilibrium length of  $1.5\sigma$ . The interactions between the surface and the beads are modeled via a 9-3 potential, which is essentially an integrated Lennard-Jones (LJ) potential over a semi-infinite slab of LJ particles, which allows us to treat the surface as a smooth plane. The well-depth of the 9-3 potentials for the head bead and the alkyl tail beads are  $\epsilon_{HS}$  and  $\epsilon_{TS}$  respectively. Simulations are performed for different values of  $\epsilon_{HS}$  and  $\epsilon_{TS}$  in order to obtain the equilibrium morphologies and compare them against the predictions of our theoretical model. Interactions between any two alkyl beads are modeled via a LJ potential with the potential well-depth of  $\epsilon_{TT}$ .

Interactions between a polar bead and an alkyl bead are modeled via a purely repulsive Weeks-Chandler-Andersen potential. Solvent is treated implicitly in the simulations. The effect of solvent is incorporated by performing Langevin dynamics simulations. All quantities are reported in reduced units. Thermal energy,  $k_B T$  is taken as the unit of energy,  $\sigma$  is taken as the unit of length and the mass of an alkyl bead,  $m$  is taken as the unit of mass. To test the theoretical prediction, the  $\epsilon_{HS}$  is varied from 3 to 5  $k_B T$ . This range of values match the typical binding energies that have been calculated for polar groups on metal surfaces [69]. The  $\epsilon_{TS}$  is varied from 0 to 0.65  $k_B T$ . As in our previous work [95], the potential well-depth of the interaction between two alkyl beads is set to  $\epsilon_{TT} = 0.065 k_B T$ . For this value of  $\epsilon_{TT}$ , the overall hydrophobic interaction between two alkyl tails is of the order of a  $k_B T$  [96]. The time step and the damping parameter for the Langevin dynamics simulations is  $0.001 \sigma \left(\frac{m}{k_B T}\right)^{1/2}$  and  $0.1 \sigma \left(\frac{m}{k_B T}\right)^{1/2}$ . The force constants associated with the bond and angle harmonic potentials are  $100 k_B T / \sigma^2$  and  $50 k_B T / \text{radians}^2$  respectively. The size of the simulation box is  $26.93\sigma \times 26.94\sigma \times 40.0\sigma$ . These dimensions are chosen to ensure that the volume density of the surfactants in our system is equal to that in our previous work on symmetrical, linear surfactant molecules [95]. The total number of molecules in the simulation box is 400.

To apply the theoretical model [equation 4.7], one needs to determine the values of  $P^L$  and  $P^S$  from the simulations, which depend on the values of  $N^L$  and  $N^S$  respectively. The values of  $N^L$  and  $N^S$  are determined by counting the number of molecules in the first adsorbed layer of the two configurations when the surface is maximally covered by the molecules. In our simulations (discussed later), we find that  $P^L \approx P^S$ , and so equation 4.7 does not require any fitting parameters to be calculated from the simulations. The condition of  $P^L \approx P^S$  is not surprising because our theoretical model is valid under the assumption that the adsorption of molecules is strongly favored and as a result the surfaces is expected to be maximally covered [95].

## 4.4 Results and Discussion

### 4.4.1 Validating the Theoretical Model

In the first layer, the surfactant molecules may adsorb either in the lying-down or in the standing-up configuration depending on the strength of their interactions with the surface. Figure 4.1 shows results of the simulations performed by choosing different values of  $\epsilon_{HS}$  and  $\epsilon_{TS}$ . Every data-point in the figure corresponds to the equilibrium adsorbed configuration of the surfactant molecules for a given  $(\epsilon_{TS}, \epsilon_{HS})$ . The figure also shows prediction of the theoretical model [equation 4.7] for which  $E^L = E^S$ , that is, when the energy associated with the lying-down and the standing-up configuration is equal. For a given value of  $\epsilon_{TS}$ , if the  $\epsilon_{HS}$  is above the theoretical line, then the standing-up configuration is expected to be preferred over the lying-down configuration. Figure 4.1 shows that this is indeed the result that is obtained in our simulations, implying that our theoretical model is quantitatively accurate in predicting the adsorbed configurations of asymmetrical surfactant molecules on polar surfaces. Interestingly, for some data-points close to the theoretical line in Figure 4.1, the standing-up and the lying-down configurations co-exist. These data-points are labeled as “Mixed” in Figure 4.1.

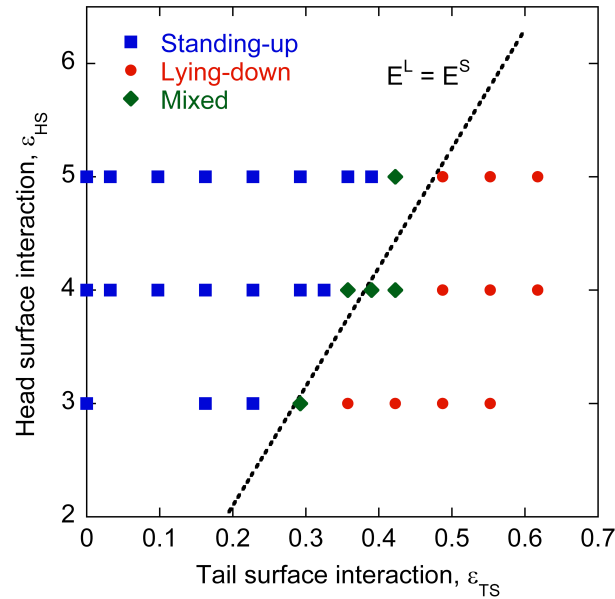


Figure 4.1: Results of equilibrium adsorbed configurations obtained in Langevin dynamics simulations performed for different values of  $(\epsilon_{TS}, \epsilon_{HS})$ . The theoretically predicted condition of  $E^L = E^S$  is also shown. The results from the simulations are found to be in quantitative agreement with the theory.

The standing-up and the lying-down configurations are identified from the significantly different orientational distributions of the adsorbed molecules. This is illustrated in Figure 4.2(a), which shows the distribution of angles in these two configurations. The angle  $\theta$ , is defined as the angle that the vector joining the terminal alkyl bead to the polar head bead forms with the plane of the surface. The distribution of  $\theta$  shown in Figure 4.2(a) has been normalized by  $\cos \theta$ . In the lying-down configuration, the distribution has a peak  $\theta \approx 7^\circ$ , which is as per our expectation because the surfactant molecule is  $7.2\sigma$  long and the polar head is  $1\sigma$  larger than the alkyl bead. On the other hand, in the standing-up configuration, the distribution is broad at  $\pm 90^\circ$ . For the standing-up configuration, the distribution does not go to zero for any  $\theta$ , implying that the adsorption morphology is like a (squished)

cylinder/sphere. Figure 4.2(b) shows distribution of the center-of-mass of the molecules in the two adsorbed configurations shown in Figure 4.2(a). The two configurations have different center-of-mass distributions as expected. The lying-down configuration has a sharp peak at  $1\sigma$  from the surface, whereas the standing-up configuration has a peak at  $5.4\sigma$  from the surface. The  $\theta$  - and the center-of-mass distributions of different  $(\epsilon_{TS}, \epsilon_{HS})$  close to the theoretical line are shown in the Figure 4.3, 4.4, 4.5. A snapshot of the adsorbed morphologies that result from the standing-up and the lying-down configurations is shown in Figure 4.6.

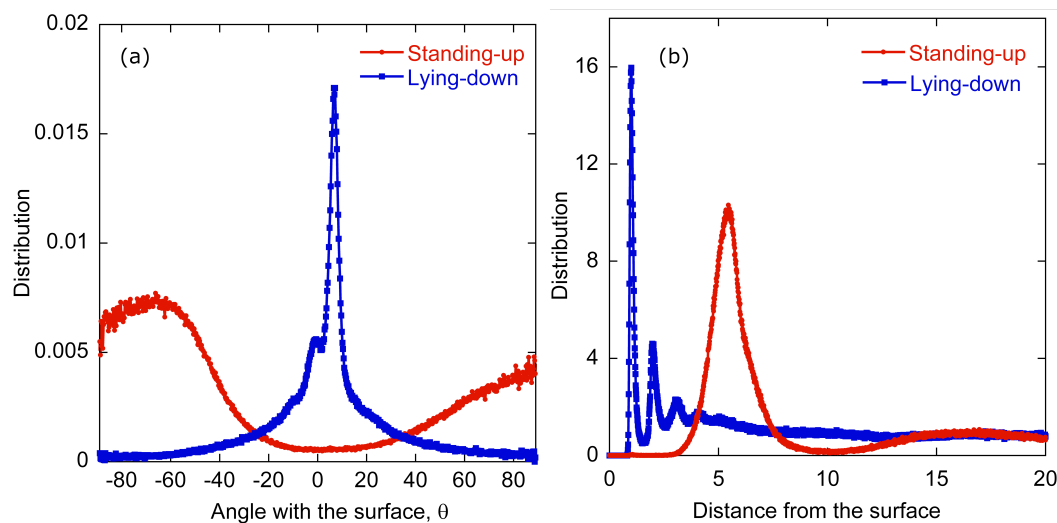


Figure 4.2: (a) Distribution of the angle that the adsorbed molecules make with the surface for  $(\epsilon_{TS}, \epsilon_{HS}) = (0.23, 5)$  (red color) and  $(\epsilon_{TS}, \epsilon_{HS}) = (0.55, 5)$  (blue color). For  $(\epsilon_{TS}, \epsilon_{HS}) = (0.23, 5)$ , the molecules attain a standing-up configuration, whereas for  $(\epsilon_{TS}, \epsilon_{HS}) = (0.55, 5)$ , the molecules attain a lying-down configuration. (b) Distribution of center-of-mass of the molecules from the surface for  $(\epsilon_{TS}, \epsilon_{HS}) = (0.23, 5)$  (red color) and  $(\epsilon_{TS}, \epsilon_{HS}) = (0.55, 5)$  (blue color). The lying-down configuration shows a sharp peak at  $1\sigma$ , while the standing-up configuration shows a peak at  $5.4\sigma$ .

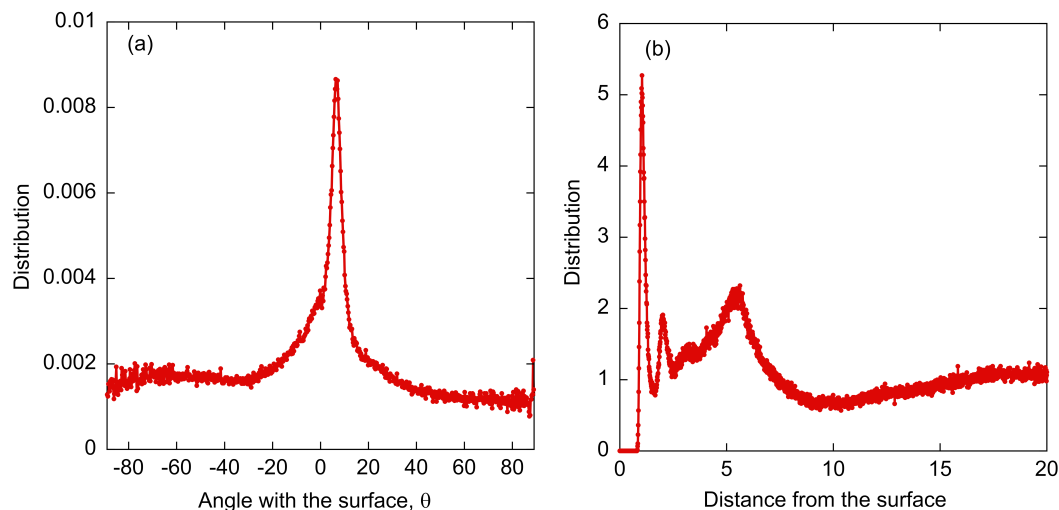


Figure 4.3: (a) Distribution of the angle that the adsorbed molecules make with the surface for  $(\varepsilon_{TS}, \varepsilon_{HS}) = (0.36, 3)$ . (b) Distribution of center-of-mass of the molecules from the surface for the same simulation point. This state-point shows formation of a lying-down configuration.

To visualize the adsorption morphologies, we have generated “instantaneous interfaces” snapshots of the adsorbed molecules [97] (Figure 4.7). In instantaneous interfaces, a continuous mass-density field is generated by applying a Gaussian distribution centered at the location of each particle in the system. At each point in space, contribution from these Gaussian distributions are added to determine the overall density field. Figure 4.7(a) and (b) show top-view snapshots obtained from instantaneous interfaces for the standing-up  $[\varepsilon_{TS}, \varepsilon_{HS} = (0.23, 5)]$  and the lying-down configurations  $[\varepsilon_{TS}, \varepsilon_{HS} = (0.55, 5)]$  respectively. Details of the parameters employed for generating these interfaces are discussed in the figure caption. In the standing-up configuration, the instantaneous interfaces show the morphology to be close to cylindrical, whereas in the lying-down configuration, the morphology more closely resembles spheres.

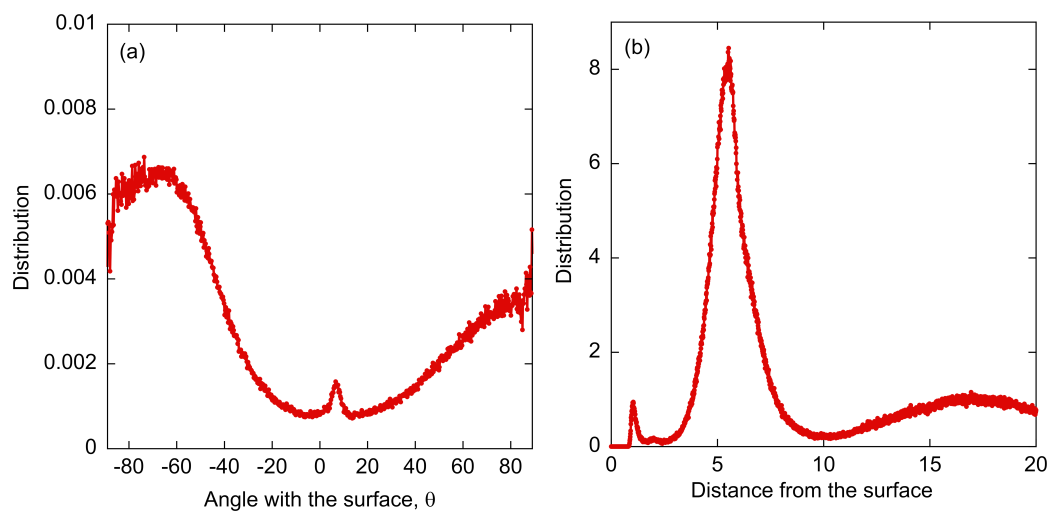


Figure 4.4: (a) Distribution of the angle that the adsorbed molecules make with the surface for  $(\varepsilon_{TS}, \varepsilon_{HS}) = (0.32, 4)$ . (b) Distribution of center-of-mass of the molecules from the surface for the same simulation point. This state-point shows formation of a standing-up configuration.

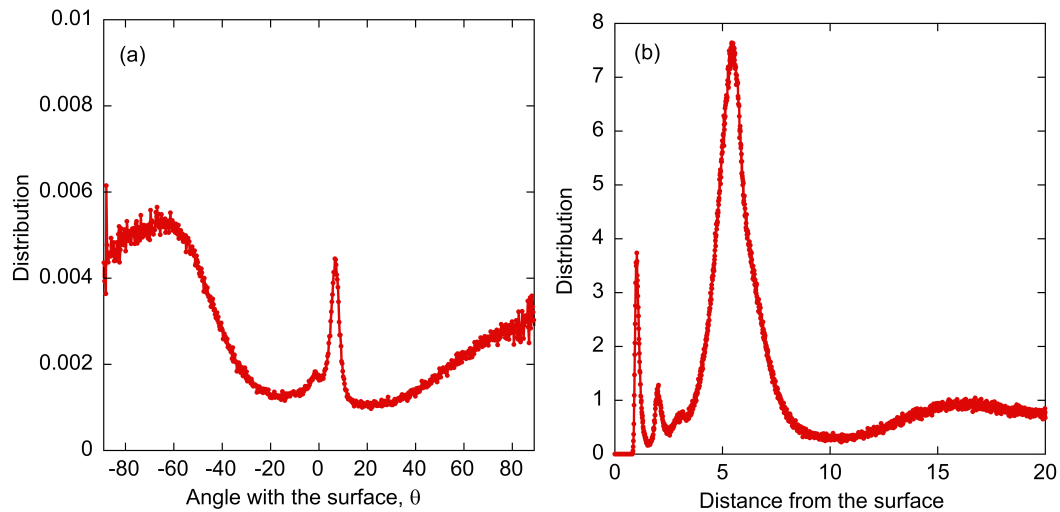


Figure 4.5: (a) Distribution of the angle that the adsorbed molecules make with the surface for  $(\epsilon_{TS}, \epsilon_{HS}) = (0.42, 5)$ . (b) Distribution of center-of-mass of the molecules from the surface for the same simulation point. This state-point shows formation of a mixed configuration.

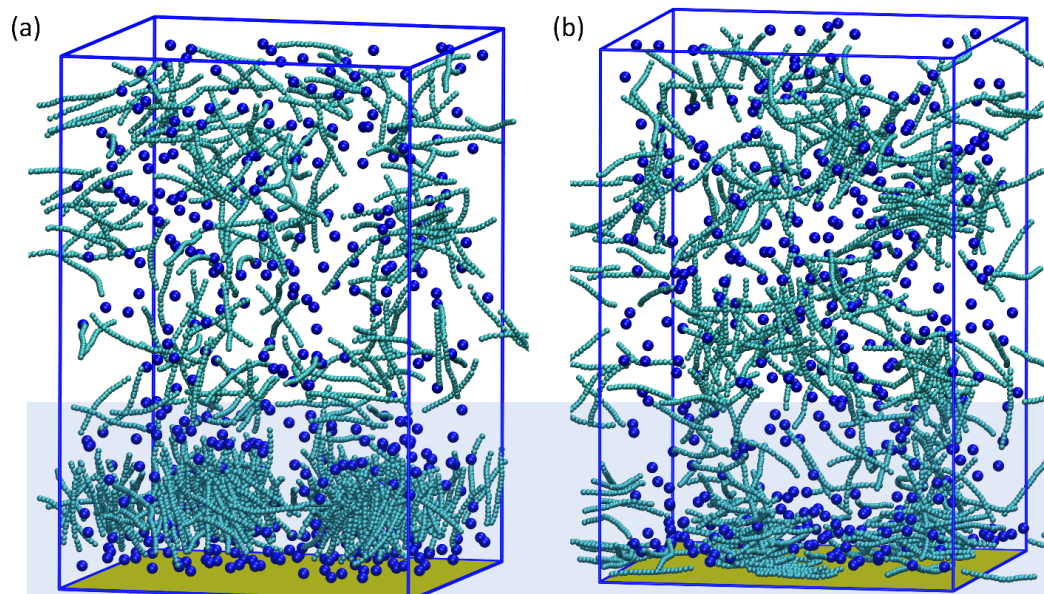


Figure 4.6: A snapshot of the equilibrated simulation system for (a)  $\varepsilon_{TS}, \varepsilon_{HS} = (0.23, 5)$  and (b)  $\varepsilon_{TS}, \varepsilon_{HS} = (0.55, 5)$  showing the standing-up and the lying-down configurations respectively. The region close to the surface has been shaded to highlight the adsorption region.

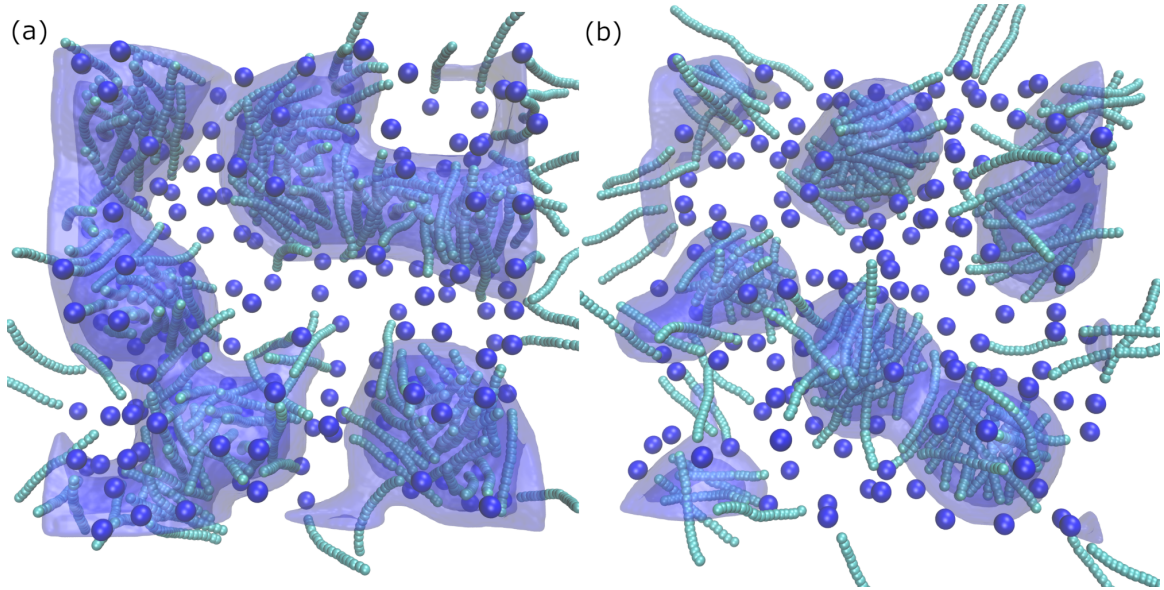


Figure 4.7: Top view of the adsorbing surface for (a)  $\varepsilon_{TS}, \varepsilon_{HS} = (0.23, 5)$  and (b)  $\varepsilon_{TS}, \varepsilon_{HS} = (0.55, 5)$ . To visualize the morphology, instantaneous interfaces (blue surfaces) are generated by coarse-graining the density field by placing a normalized Gaussian function,  $\phi(r; \zeta) = (2\pi\zeta^2)^{-3/2} e^{-r^2/2\zeta^2}$  centered at the location  $r$  of each bead. The density field at any location is the summation of the contribution from the different Gaussian distributions. For our calculations, we choose  $\zeta = 1.5\sigma$ . The interface is formed by setting the lower and the upper cutoff values of the density field as  $0.5\sigma^{-3}$  and  $0.7\sigma^{-3}$  respectively.

The kind of configuration that the surfactants attain upon adsorption affects the total number of adsorbed molecules  $\langle N \rangle$ . Figure 4.8 shows the  $\langle N \rangle$  for different values of  $\epsilon_{HS}$  and  $\epsilon_{TS}$ . In the standing-up configuration (shown by filled symbols), the number of molecules does not vary significantly with  $\epsilon_{TS}$  for a given value of  $\epsilon_{HS}$ . A sharp drop in  $\langle N \rangle$  is observed as the configurations transition from the standing-up to the lying-down state (shown by open symbols). Mixed configurations (shown by the cross symbol), in which the lying-down and the standing-up configurations coexist, have intermediate values of the  $\langle N \rangle$ . The  $\langle N \rangle$  is smaller for the lying-down configurations, because the molecules occupy more surface area and so fewer molecules adsorb. It is an important result in the sense that as the  $\epsilon_{TS}$  increases for a given  $\epsilon_{HS}$ , the total affinity of a surfactant molecule for the surface increases. However, our analysis shows that this increase in the affinity may result in a decrease in the  $\langle N \rangle$  if the adsorbed configuration of the molecules changes.

#### 4.4.2 Kinetic Pathways of Formation of Adsorption Morphologies

Previous experiments have suggested that the organization of adsorbed surfactants in different morphologies may follow two different kinetic pathways. In the first pathway, the molecules initially adsorb lying down on the surface and then as more adsorption occurs, they undergo an orientational transition to stand up on the surface. In the second pathway, the molecules adsorb in the standing-up configuration to form islands. These islands grow and eventually coalesce to form the adsorption layer. Both these kinetic pathways are observed in our simulations, and the preferred pathway depends on the relative magnitudes of  $\epsilon_{TS}$  and  $\epsilon_{HS}$ . Figure 4.9(a) shows distribution of the angle,  $\theta$  at different times during the adsorption process for the case when  $(\epsilon_{TS}, \epsilon_{HS}) = (0.39, 5)$ . For this set of interactions, the molecules are expected to attain the standing-up configuration as per the Figure 4.1. The first time-period,  $t_1$  shows the  $\theta$ -distribution to be sharply peaked at  $7^\circ$ , which is a

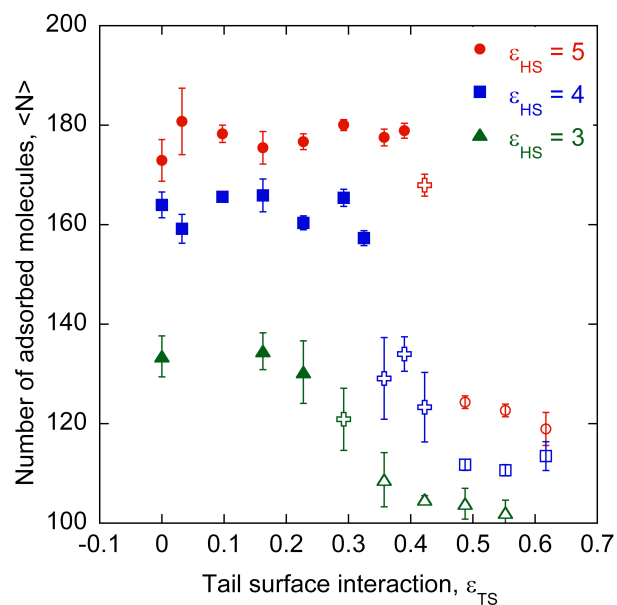


Figure 4.8: Equilibrium number of adsorbed molecules,  $\langle N \rangle$  as a function of  $\epsilon_{TS}$  for different values of  $\epsilon_{HS}$ . The standing-up configurations are shown by filled symbols, and the lying down configurations are shown by open symbols. The mixed configurations are shown by the  $\boxplus$  symbol. Error bars are the standard deviation calculated from four different simulations.

signature of the lying-down configuration. There is a fraction of the molecules is standing-up on the surface, as the distribution is non-zero at  $\theta = \pm 80^\circ$ . Figure 4.9(b) shows the distribution of the center-of-mass of the molecules from the surface. For the time-period  $t_1$ , the distribution in Fig. 6(b) has peaks at  $1\sigma$  and  $5.4\sigma$  from the surface, indicating that some molecules are lying-down, while some are standing-up on the surface. The time-period  $t_1$  is from time 0 to  $8.5 \times 10^4 \sigma \left(\frac{m}{k_B T}\right)^{1/2}$  wherein the number of adsorbed molecules,  $N$  increases from 0 to 150. The surface coverage from adsorbed molecules is close to 90% by the end of the  $t_1$  (4.10). In the second time-period,  $t_2$  (from  $8.5 - 17 \times 10^4 \sigma \left(\frac{m}{k_B T}\right)^{1/2}$ ), it is observed that the peaks corresponding to the lying-down configuration reduce in the Fig. 6(a) and (b), implying that more molecules now stand up on the surface. The  $N$  increases from 150 to 170 in this period. The period  $t_3$  is from  $25.5 - 34 \times 10^4 \sigma \left(\frac{m}{k_B T}\right)^{1/2}$ . It is observed that the signatures of the lying-down configuration are now absent, implying that all the adsorbed molecules are standing-up on the surface. Thus, for this value of  $(\epsilon_{TS}, \epsilon_{HS})$ , the kinetic pathway involves an initial adsorption of the surfactant molecules in the lying-down configuration, which is followed by a gradual orientational transition to the standing-up configuration. This kind of kinetic pathway is observed for the state-points that are close to the theoretical line of  $E^L = E^S$ . For such state-points, the lying-down configuration is energetically comparable to the standing-up configuration.

To observe the second kind of kinetic pathway, one can analyze the adsorption kinetics of a data-point for the standing-up configuration that is away from the theoretical line of  $E^L = E^S$ . Figure 4.11 shows distribution of the angle  $\theta$  at different times during the adsorption process for the case when  $(\epsilon_{TS}, \epsilon_{HS})=(0.23, 5)$ . In this case, the  $\theta$ -distribution at all time-periods ( $t_1 < t_2 < t_3$ ) and  $t_3$  match with that of a standing-up configuration. Thus, in this case, the kinetic pathway involves formation of islands of standing-up molecules. These islands grow and coalesce as the adsorption increases with time.

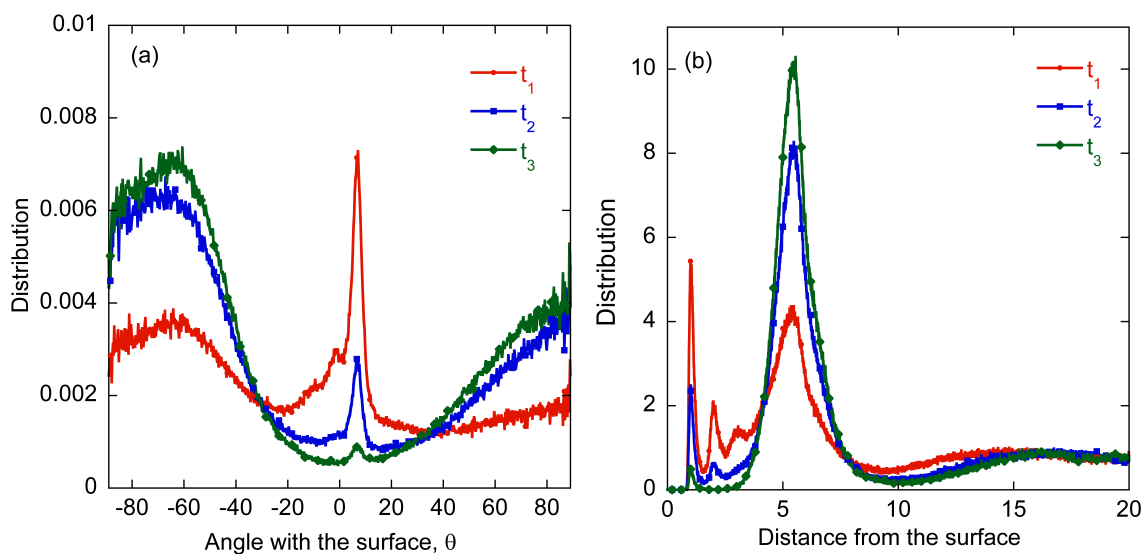


Figure 4.9: Kinetics of adsorption of the surfactants for  $(\epsilon_{TS}, \epsilon_{HS}) = (0.39, 5)$ . (a) shows the distribution of the angle that the molecules form with the surface,  $\theta$  at different time periods ( $t_1 < t_2 < t_3$ ). (b) shows the distribution of the distance of the center-of-mass of the molecules from the surface for the same time periods. These graphs show that the kinetics of adsorption involve a standing up to a lying down orientational transition.

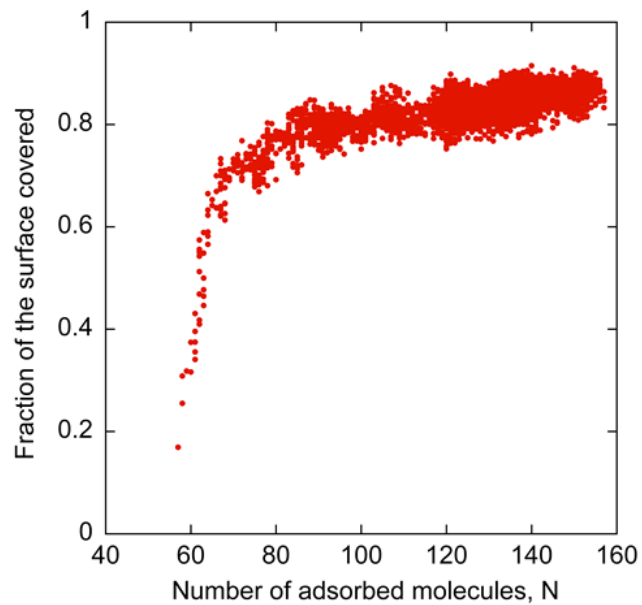


Figure 4.10: Fraction of the surface covered by surfactant molecules as a function of the number of adsorbed molecules,  $N$  for  $(\epsilon_{TS}, \epsilon_{HS}) = (0.23, 5)$ . The molecules adsorb in the standing-up configuration.

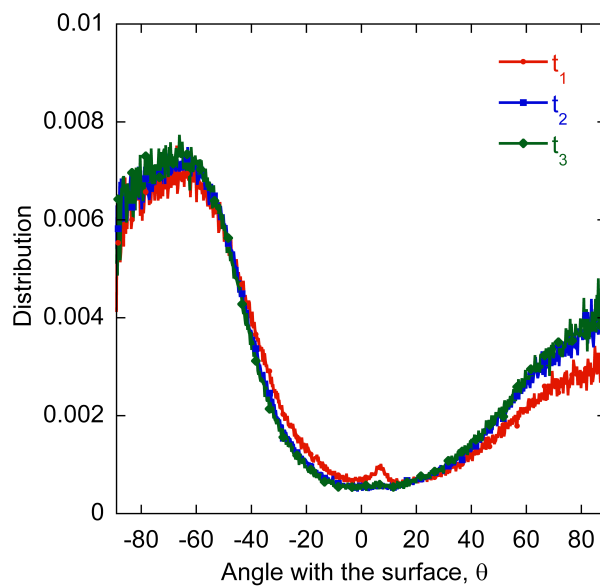


Figure 4.11: Kinetics of adsorption of the surfactants for  $(\varepsilon_{TS}, \varepsilon_{HS})=(0.23, 5)$ . The figure shows the distribution of the angle that the molecules form with the surface,  $\theta$  at different time periods ( $t_1 < t_2 < t_3$ ). At all times, the distribution of the  $\theta$  represents the standing-up configuration.

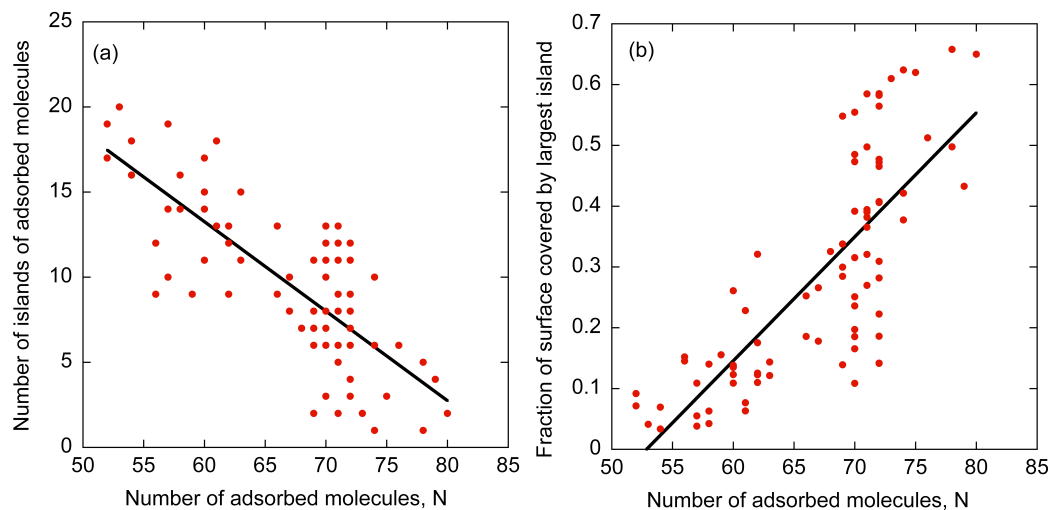


Figure 4.12: Formation of islands of adsorbed molecules during the adsorption process in the case of  $(\varepsilon_{TS}, \varepsilon_{HS}) = (0.23, 5)$ . (a) Number of islands as a function of the number of adsorbed molecules, N, and (b) fraction of the surface area covered by the largest island as a function of N. Linear, best fit lines are shown as a guide to the eye.

To identify the islands on the surface, the following procedure is employed: the surface is divided into cubes of side  $0.2\sigma$ . All alkyl beads within  $1.5\sigma$  and all polar beads within  $3\sigma$  from the surface are projected onto the plane of the surface. The cubes that are within  $0.8\sigma/0.8\sigma_P$  from the alkyl / polar beads are labeled as occupied. The adjacent occupied cubes are considered part of an island. Figure 4.12 illustrates the formation and growth of islands of adsorbed molecules for  $(\epsilon_{TS}, \epsilon_{HS}) = (0.23, 5)$ . Figure 4.12(a) shows the number of islands as a function of  $N$ . A large number of islands form on the surface initially. As  $N$  increases, these islands grow and coalesce into one-another. The large fluctuation in the number of islands for a given value of  $N$  indicates that many islands break and form during the course of adsorption. This is further evidenced in Figure 4.13 wherein the number of islands is plotted as a function of total surface coverage. It is observed that for a given surface coverage, there is fluctuation in the number of islands. For the same trajectory as shown in 4.12(a), 4.12(b) tracks the size of the largest island as a function of  $N$ . The size is shown in terms of the fraction of the total surface area covered by the largest island. It is observed that the largest island grows as  $N$  increases.

#### 4.5 Conclusions

In this work, we have developed a theoretical model to predict adsorbed configurations of surfactant molecules on polar surfaces. Asymmetric surfactant molecules that have a linear alkyl tail and a large polar head group is the main focus. The theoretical model is based on the principle that if the interactions of the polar head with the surface is much stronger than that of the alkyl tail with the surface, then the molecules attain a configuration in which they adsorb by standing-up on the surface. This adsorbed configuration allows more molecules to adsorb in comparison to the lying-down configuration and thus lowers the overall energy of the system. On the other hand, if the interactions of the alkyl tail with the surface are strong, the molecules adsorb in the lying-down configuration. Due to

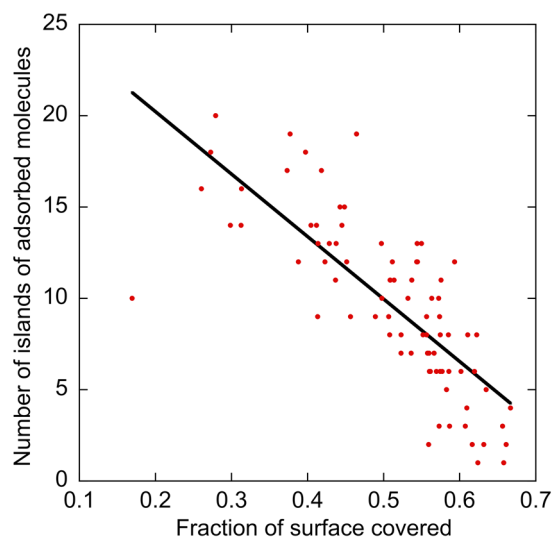


Figure 4.13: Number of islands of adsorbed molecules as a function of the fraction of the surface covered by surfactant molecules for  $(\varepsilon_{TS}, \varepsilon_{HS}) = (0.23, 5)$ . Fluctuations in the number of islands for a given coverage indicates that the islands coalesce and break apart on the surface.

the asymmetrical geometry of the surfactant molecules, the molecules attain a cylindrical morphology in the standing-up configuration and a spherical morphology in the lying-down configuration. Our simulations show that the theoretical model is quantitatively accurate in predicting adsorbed configurations of surfactant molecules.

## 5 EXPERIMENTS AND MOLECULAR SIMULATION STUDY OF HOW CO-ADSORPTION OF OIL MOLECULES IN ADSORBED CORROSION INHIBITORS IMPROVES CORROSION MITIGATION<sup>7</sup>

### 5.1 Introduction

Oil and gas transportation pipelines, made of mild steel, are prone to internal corrosion upon exposure to water, which is invariably present in oil and gas streams [98]. An efficient and cost-effective method of mitigating internal corrosion of these pipelines is to inject organic corrosion inhibitors in the fluid stream continuously at concentration levels of parts-per-million [5, 47]. Amphiphilic surfactant molecules have been found to be effective corrosion inhibitors [5, 16, 47]. Imidazole, quaternary ammonium, amide and amidoamine based surfactants are popular corrosion inhibitors due to their low toxicity and high efficacy [1, 16, 17]. These molecules consist of a hydrophobic tail (non-polar) and a hydrophilic head (polar) group. The hydrophobic tails are hydrocarbon chains comprised of usually 6 to 22 carbon atoms, while the hydrophilic heads are either non-ionic or ionic functional groups. The protective properties of these molecules are closely related to their adsorption at the metal-water interface [99].

Adsorption behavior as well as efficiency of corrosion inhibitors have been researched extensively in experimental and simulation studies [14, 91, 94, 100–102]. Most of these studies have focused on evaluating corrosion inhibition mechanism in aqueous phase devoid of any oil. A few researchers have studied the effect of oil wetting, and have reported that the presence of an oil phase improves corrosion inhibition efficiency of inhibitor molecules [103]. McMahon showed that the adsorption of oleic imidazoline

---

<sup>7</sup> This chapter has been published and is formatted to the requirements of Corrosion Journal. Ko, X., Olivo, J. D., Brown, B., Nešić, S., & Sharma, S. (2020). Experiments and Molecular Simulations to Study the Role of Coadsorption of Oil in Corrosion Inhibitor Films in Improving Corrosion Mitigation. *Corrosion*, 76(11). © NACE [2020], used with permission.

inhibitors onto oil-wet steel surfaces was fast and does not depend on the type of oil used to wet the surface. A monolayer of oleic imidazoline was found to adsorb on the oil-wet steel surface [5]. Improvement in corrosion inhibition due to oil has been reported in other studies [104]. Foss et al. studied the effect of corrosion inhibitors on the wettability of carbon steel [105], iron carbonate ( $\text{FeCO}_3$ ) covered steel surfaces [106], and ferric oxide covered steel surfaces [107], and found that both oleic imidazoline and phosphate ester altered the wettability of a bare steel surface from hydrophilic to hydrophobic, and the performance of oleic imidazoline and phosphate ester significantly increased after oil wetting of the bare steel surface and iron carbonate covered steel surface. By observing the water droplet contact angle as a function of inhibitor concentration, Li et al. [103] concluded that fatty amine-type inhibitor was more effective in altering the wettability from water-wet to oil-wet compared to quaternary ammonium chloride inhibitors, and direct exposure of the surface to oil enhanced the performance of the fatty amine-type inhibitor. Researchers have attributed this improved performance to co-adsorption of inhibitor and oil molecules at the metal-water interface. These experimental works provide evidence that the presence of oil has an effect on the adsorption and performance of corrosion inhibitors. So far, these experimental observations have only been explained by hypothesizing how oil molecules might be interacting with corrosion inhibitor molecules. There has been no direct investigation of the molecular-level interactions between oil and corrosion inhibitor molecules.

In this study, we have performed molecular simulations to understand how the presence of oil molecules affects the adsorption behavior of corrosion inhibitor molecules. We report that oil molecules get co-adsorbed in the corrosion inhibitor film due to lateral hydrophobic interactions between the oil molecules and the tails of inhibitor molecules. We find that the co-adsorbed oil molecules are able to change the morphology of adsorbed corrosion inhibitor films and can significantly enhance the structural ordering and hydropho-

bic character of the adsorbed films. This is the first ever study that has directly revealed molecular-level behavior of how oil molecules affect corrosion inhibitor films.

## 5.2 Scope of Work

### **Basic Ideas of Molecular Simulations:**

It is understood that any equilibrium thermodynamic state is essentially an ensemble of a large number of molecular configurations or microstates because molecules are in constant motion. To get a quantitative perspective, consider that the average speed of molecules, calculated via Maxwell-Boltzmann distribution, is  $\sim 500$  m/s at room temperature. At liquid state densities, the mean free path between the molecules is  $\sim 0.5$  nm, so one would expect close to  $10^{12}$  molecular collisions occurring per second per molecule. Consequently, thermodynamic properties are statistical properties of a large number of microstates. The relationship between molecular and thermodynamic properties is well established in the theory of statistical mechanics. In molecular simulations, microstates associated with a thermodynamic state are generated by simulating the motion of molecules, often by utilizing computational power of many processors operating in a parallel fashion in a computer cluster.

To simulate molecular motion, one needs to know the nature of atomic forces. Every atom in a system exerts a distance-dependent force on every other atom. These forces are electrostatic in nature and arise due to the interactions of electron clouds and nuclei. While calculation of electronic motion requires solving the equations of quantum mechanics, the motion of nuclei of atoms heavier than hydrogen can be well understood via classical Newtonian mechanics. The forces depend on the type of the atoms. For example, non-polar alkane molecules will predominantly interact via van der Waals forces. Polar and charged molecules will also have coulombic interactions. Distance-dependent forces between different atoms are represented via mathematical functions called force fields.

Therefore, to perform molecular simulations, one needs to generate an initial molecular configuration of the system, define the force field and define the thermodynamic state of the system, such as a constant number of molecules  $N$ , volume  $V$ , and temperature  $T$ . Starting from the initial molecular configuration, forces between all atoms is calculated. Numerical integration of classical equations of motion is then performed to generate molecular trajectories. The forces are calculated after every femto-second ( $10^{-15}$  s), because the forces depend on the distance between the atoms and therefore are continuously changing.

### 5.2.1 Simulation Setup:

Often, a useful approach to study molecular behavior is to employ a coarse-grained (CG) description of the molecules that comprise a system. In a CG description, instead of explicitly representing every atom in the simulation, a group of atoms are combined into a united atom or a CG bead, as shown schematically in Figure 5.1 [76]. As an example, an alkyl group can be represented by only one bead. This approach helps in significantly reducing the number of particles in the simulation system and thus makes the simulation computationally fast. In systems where a large number of molecules are needed, for example, in self-assembly or phase transitions, CG descriptions are useful to enable longer simulations.

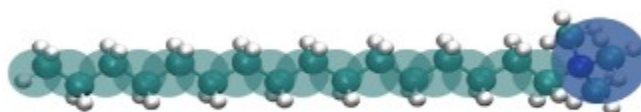


Figure 5.1: A schematic of the coarse-grained model of a corrosion inhibitor. The cyan colored beads represent the alkyl tail and the blue colored bead represents the polar head group.

In this study, corrosion inhibitor molecules are represented by a CG model, same as the one employed in our previous study [90]. A corrosion inhibitor molecule has a polar head group, which has strong affinity for the metal surface. Alkyl tails of corrosion inhibitor molecules have hydrophobic interactions between them. In this CG model, one terminal bead represents the polar head group, and all the other beads in the molecule are hydrophobic and represent the alkyl tail. Oil molecules are represented as linear chains of hydrophobic beads. Bonds between the connected beads in a molecule are modeled as harmonic potentials given by,

$$V_b(r) = k(r - r_0)^2 \quad (5.1)$$

where  $V_b(r)$  is the distance-dependent bond potential,  $k$  is the bond coefficient,  $r$  is the distance between the two connected beads and  $r_0$  is the equilibrium bond-length. The angle between two adjacent bonds in a molecule are restrained via harmonic potentials given by,

$$V_a(\theta) = k_\theta(\theta - \theta_0)^2 \quad (5.2)$$

where  $V_a(\theta)$  is the angle potential,  $k_\theta$  is the angle coefficient,  $\theta$  is the value of angle between the bonds and  $\theta_0$  is the equilibrium angle. The equilibrium angle is set to  $180^\circ$  to model linear corrosion inhibitor molecules. Interactions between all hydrophobic beads, that is, between the tail beads of inhibitor molecules, between the oil beads, as well as between the inhibitor tail and oil beads are modeled via Lennard-Jones (LJ) potential with the length parameter  $\sigma$ , and potential well-depth of  $\varepsilon$ ,

$$V_{LJ}(r) = 4\varepsilon \left( \frac{\sigma^{12}}{r^{12}} - \frac{\sigma^6}{r^6} \right) \quad (5.3)$$

The potential well-depth parameter  $\varepsilon$  determines strength of the attractive interaction. The parameter  $\sigma$  determines the effective diameter of the bead. In a LJ potential, at distances,  $r < 2^{1/6}\sigma$  the interaction potential becomes strongly repulsive, whereas, for distances,  $r > 2^{1/6}\sigma$  the potential is attractive. The LJ potential decreases at the rate of  $r^6$  and

therefore is a short-ranged potential. LJ potential is employed to model van der Waals and hydrophobic interactions between species. Interactions between the polar head beads and the hydrophobic beads are modeled by purely repulsive Weeks-Chandler-Anderson (WCA) potential [66]. WCA potential is a truncated and shifted LJ potential that includes only the repulsive part of LJ potential, with the LJ length parameter  $\sigma_p$  determining the effective diameter of the polar bead. The functional form of WCA potential is given by,

$$V_{WCA}(r) = 4\varepsilon \left( \frac{\sigma_p^{12}}{r^{12}} - \frac{\sigma_p^6}{r^6} \right) + \varepsilon \text{ for } r < 2^{1/6}\sigma_p \text{ and } 0 \text{ otherwise} \quad (5.4)$$

In effect, the WCA potential models the excluded volume interactions between species. In an aqueous environment, polar head groups are solvated and thus do not have a net interaction with other polar head groups apart from excluded volume because of their size. The metal surface is represented by a smooth, two-dimensional surface occupying the bottom face of the simulation box at  $z = 0$ . The strong attractive interactions between the polar head beads and the surface are modeled via a 9-3 potential with the well-depth of  $\varepsilon_S$ . A 9-3 potential is obtained with the LJ potential and is integrated over a semi-infinite slab made of LJ particles [41]. The functional form of 9-3 potential is given by,

$$V_{9-3}(z) = \varepsilon_S \left( \frac{2}{15} \frac{\sigma_S^9}{z^9} - \frac{\sigma_S^8}{z^8} \right) \quad (5.5)$$

where  $z$  is the distance between the beads and the surface. The hydrophobic beads have only repulsive, hard sphere interactions with the surface. Water is treated implicitly in the simulation. The effect of water is taken into account by including an attractive hydrophobic interaction between the alkyl beads. In addition, the motion of the molecules is modeled via Langevin dynamics (discussed later). The simulation box is periodic in the X and Y dimensions. To keep a constant simulation volume, reflective boundary conditions are applied to all beads at the side opposite of the  $z = 0$  surface of the simulation box.

All quantities in this study are defined using reduced units [41]. In reduced units, the units of energy, mass, length are defined so as to save computational costs in simulations

and can be easily converted into real units. In this system, the unit of energy is taken as thermal energy,  $k_B T$  ( $k_B$  is Boltzmann constant and  $T$  is the temperature), which is set to 1. The potential well-depth,  $\varepsilon$ , has units of energy, and therefore is specified with respect to  $k_B T$ . For instance, an  $\varepsilon = 0.5$  implies that the potential well-depth is half of the thermal energy. The mass of each bead is set to 1, and the size of each hydrophobic bead,  $\sigma$ , is set to 1 in reduced units. Kindly refer to our previous publication for more details on reduced units [76].

### 5.2.2 Simulation Details:

Langevin dynamics simulations are performed to study adsorption behavior of corrosion inhibitor and oil molecules on the surface. In Langevin dynamics, the motion of molecules is modeled to mimic their interactions with solvent molecules. This is incorporated by applying a Gaussian-distributed random force and a frictional force in the direction opposite of the velocity to the molecules [41]. In our simulations, the temperature of 1.0 and damping constant of 0.1 (time units,  $(\varepsilon/m\sigma^2)^{0.5}t$ ) is used [41]. The LJ well-depth parameter for the interaction between hydrophobic beads,  $\varepsilon$  is set to  $0.065k_B T$ . The well-depth of the 9-3 potential for interaction between polar head groups and surface is chosen to be  $\varepsilon_S = 5k_B T$ . The value of  $\varepsilon$  was chosen to ensure that hydrophobic interactions between alkyl tails are of the order of thermal energy [68], and that of  $\varepsilon_S$  was chosen to match the strong affinity of polar head group for the metal surface, obtained from density functional theory (DFT) calculations [69]. We have shown previously that for  $\varepsilon = 0.065k_B T$ , the corrosion inhibitor molecules form a self-assembled monolayer (SAM) on the surface [90]. To study the effect of the length of oil molecules, oil molecules comprised of 10, 19 and 25 alkyl beads per molecule were studied. The length of inhibitor molecules was kept fixed at 20 beads with 1 polar bead and 19 alkyl beads in each molecule. All simulations were performed using the Large-scale Atomic/Molecular Massively Parallel

Simulator (LAMMPS) MD simulations package [70]. For each data point, the simulations were performed in parallel on eight processors or on a Graphic Processing Unit (GPU). Equilibrium was obtained after  $3 \times 10^9$  to  $4 \times 10^9$  MD time-steps.

### 5.3 Results and Discussion

#### 5.3.1 Presence of Oil Molecules Promotes Adsorption

To investigate the effect of oil molecules on adsorption of inhibitor molecules, 400 inhibitor molecules (20mers) and 400 oil molecules (19mers) are inserted at random locations in the simulation box. The diameter of the polar head group of inhibitor molecules is  $\sigma_p = 2\sigma$ . It was shown in our previous study [90, 108] that when  $\sigma_p = 2\sigma$ , that is, when the polar head is twice the size of a hydrophobic bead, the inhibitor molecules tend to aggregate in cylindrical micelles in the bulk and the adsorbed phase. The size of the simulation box is  $27\sigma \times 27\sigma$  in the XY direction and  $80\sigma$  in the Z direction. As a reference system, we first study the adsorption behavior of 800 inhibitor molecules (and no oil molecules). 5.2(a) shows a representative snapshot of the equilibrium state of the pure inhibitor system. It is observed that the inhibitor molecules with  $\sigma_p = 2\sigma$  tend to aggregate in cylindrical micelles on the surface. An enlarged snapshot of the adsorbed film is shown in Figure 5.2(b). Figure 5.2(c) shows distribution of the angle made by the molecular axes of adsorbed molecules with the surface normal,  $\theta$ .  $\theta = 0^\circ$  implies that an adsorbed molecule is lying-flat on the surface, and  $\theta = -90^\circ$  means that an adsorbed molecule is “standing” on the surface with the polar group pointing towards the surface. The distribution of  $\theta$  in Figure 5.2(c) is non-zero for all values, with higher values close to  $-60^\circ$  and  $70^\circ$ , which indicates that the adsorption morphology is like that of a squashed cylinder. Due to the asymmetric geometry of the molecules, the distribution does not peak at  $\pm 90^\circ$ . Such adsorption morphologies have been reported in many AFM studies [62].

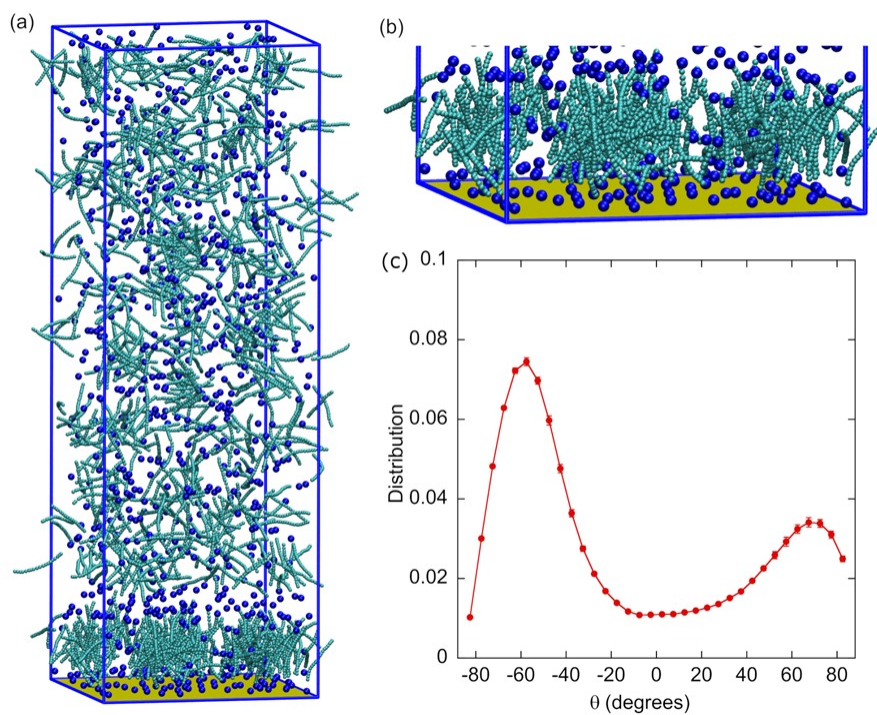


Figure 5.2: (a) A snapshot of an equilibrium configuration of the pure inhibitor system ( $\sigma_p = 2\sigma$ ). (b) An enlarged snapshot of adsorbed film of the pure inhibitor system ( $\sigma_p = 2\sigma$ ). Blue colored beads are the polar head groups, and cyan colored beads are the hydrophobic tails. (c) Distribution of angles,  $\theta$ , that adsorbed molecules make with the surface normal.

Figure 5.3(a) shows a representative snapshot of the equilibrated system when oil is added to the inhibitors with  $\sigma_p = 2\sigma$ . Figure 5.3(b) shows an enlarged image of the adsorbed layer. It is clearly seen that oil molecules are co-adsorbed in the inhibitor layer and the cylindrical morphology of the film transforms into a planar morphology. Interestingly, a large number of oil molecules are in the adsorbed layer even though the oil molecules have no affinity for the metal surface. The entrainment of oil molecules is driven by the hydrophobic interactions between inhibitor tails and oil molecules. The distribution of angles,  $\theta$  that adsorbed molecules make with the surface normal now has two sharp peaks at  $\pm 90^\circ$  and no value for intermediate angles indicating that the adsorbed molecules form a planar self-assembled monolayer (SAM). Therefore, a dramatic change in the adsorbed morphology of inhibitor molecules is observed with the introduction of oil molecules.

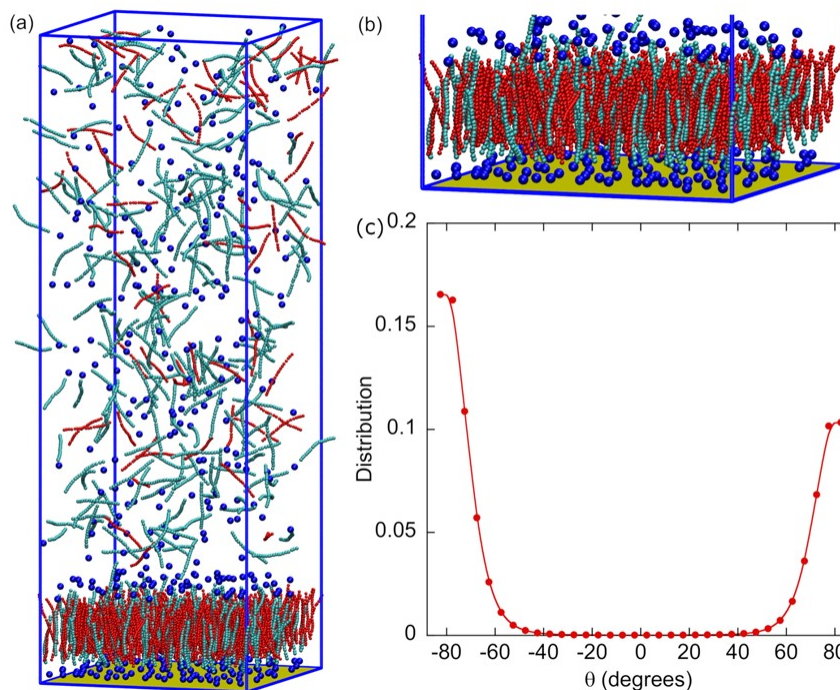


Figure 5.3: (a) A snapshot of an equilibrium configuration of the inhibitor+oil system ( $\sigma_p = 2\sigma$ ). (b) An enlarged snapshot of configuration of the inhibitor+oil system ( $\sigma_p = 2\sigma$ ). Blue colored beads are the polar head groups, cyan colored beads are the hydrophobic tails, and the red colored beads represent the oil molecules. (c) Distribution of angles,  $\theta$ , that adsorbed molecules make with the surface normal.

Next, the adsorption behavior of inhibitor molecules with  $\sigma_p = 2\sigma$  is discussed. These inhibitor molecules have been shown to form a well-packed planar SAM on the surface [90, 95]. To study the effect of oil molecules on adsorption, we introduce oil molecules in the system of inhibitor molecules with  $\sigma_p = 2\sigma$ . In these simulations, the simulation box is  $20\sigma \times 20\sigma$  in the XY direction and  $80\sigma$  in the Z direction to keep volume fraction of the system the same as the  $\sigma_p = 2\sigma$  case. 400 inhibitor molecules (20mers) and 400 oil molecules (19mers) are randomly inserted into the simulation box. Figure 5.4(a) shows a representative snapshot of an equilibrium state of the reference system

with only inhibitor molecules present. Figure 5.4(b) shows a snapshot of the system with oil molecules introduced. Both systems show that the adsorbed layer is a SAM. A good fraction of oil molecules gets co-adsorbed along with the corrosion inhibitors because of hydrophobic interactions between the oil molecules and the inhibitor tails. Figure 5.4(c) shows the distribution of  $\theta$  for the two systems. Both the systems show signatures of a planar SAM on the surface.

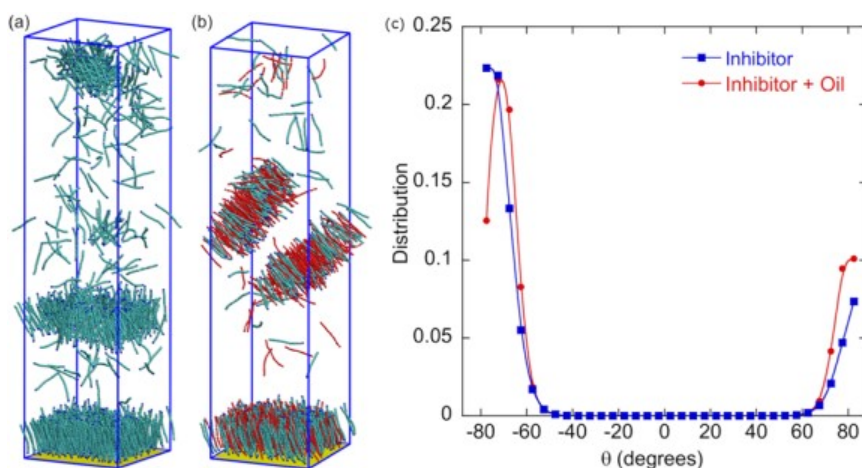


Figure 5.4: (a) A snapshot of an equilibrium configuration of the pure inhibitor system ( $\sigma_p = \sigma$ ). (b) A snapshot of equilibrium configuration of the inhibitor+oil system ( $\sigma_p = \sigma$ ). Oil molecules are in red and inhibitor molecules are in cyan with a blue colored polar head group. (c) Distribution of angles,  $\theta$ , that adsorbed molecules make with the surface normal for  $\sigma_p = \sigma$  with oil and without oil molecules present.

To quantitatively compare changes in the adsorbed film upon the introduction of oil molecules, the number of molecules adsorbed per unit area at equilibrium,  $\rho$  is plotted in Figure 5.5. For the  $\sigma_p = 2\sigma$  case, the addition of oil molecules promotes adsorption. Entrainment of oil molecules transforms the cylindrical morphology of adsorbed inhibitor film into a planar SAM. This results in a higher concentration of molecules that are tightly

packed on the surface. For the  $\sigma_p = 2\sigma$  case, the overall adsorption amount does not change significantly as the inhibitor molecules by themselves are able to adsorb in a tightly packed planar SAM. However, the composition of the adsorbed film changes with a good fraction of oil molecules are co-adsorbed in the film, even when the oil molecules and the metal surface do not have any attractive interactions in our model.

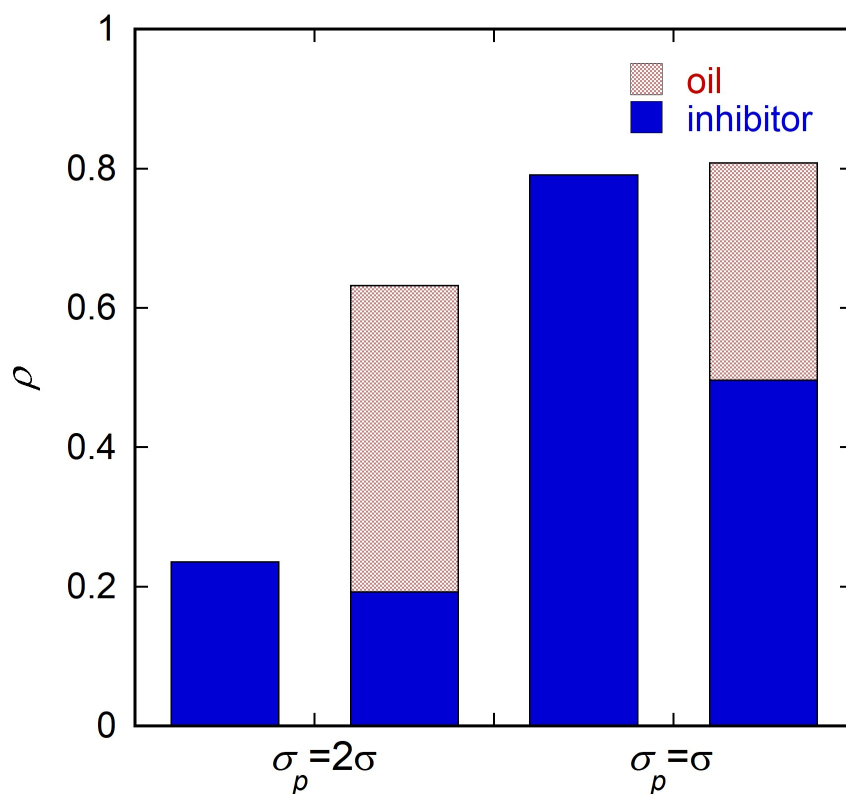


Figure 5.5: Number of molecules adsorbed per unit area,  $\rho$  for  $\sigma_p = 2\sigma$  and  $\sigma_p = \sigma$  with oil and without oil molecules present. Error is of the order  $10^{-4}$ .

Our simulation results show that oil molecules have a tendency to be co-adsorbed in the inhibitor films due to hydrophobic interactions. Interestingly, the entrainment of oil molecules may result in changing the adsorbed morphology of the adsorbed inhibitor film, which can result in enhanced adsorption.

### 5.3.2 Presence of Oil Molecules Improves Corrosion Inhibition Properties of Adsorbed Films

How the structural properties of the adsorbed inhibitor films are affected by the entrainment of oil molecules was also analyzed in this research. The local structural arrangement of molecules in the adsorbed film was studied by calculating radial distribution function along the plane of the film, the XY plane,  $RDF_{xy}(r)$ .  $RDF_{xy}(r)$  shows the local density of molecules around a given molecule divided by the density expected in a uniform distribution. Therefore,  $RDF_{xy}(r) = 1$  implies that there is no preferential arrangement of molecules (ideal gas behavior).

Figure 5.6(a) shows the  $RDF_{xy}(r)$  of adsorbed molecules for the pure inhibitor system and for the inhibitor + oil system for the  $\sigma_p = 2\sigma$  case. The  $RDF_{xy}(r)$  of the inhibitor only system shows a peak and a shoulder followed by a depletion region indicating that the molecules are aggregated in micellar structures. On the other hand, for the inhibitor + oil system, the  $RDF_{xy}(r)$  shows regular peaks, indicating presence of a much more ordered structure in the film. For the  $\sigma_p = \sigma$  case (5.6(b)), the  $RDF_{xy}(r)$  of the pure inhibitor system shows regular peaks, a signature of an ordered SAM. Interestingly, for the inhibitor + oil system, the peaks of the  $RDF_{xy}(r)$  become larger indicating that in the presence of oil molecules, the film becomes more ordered.

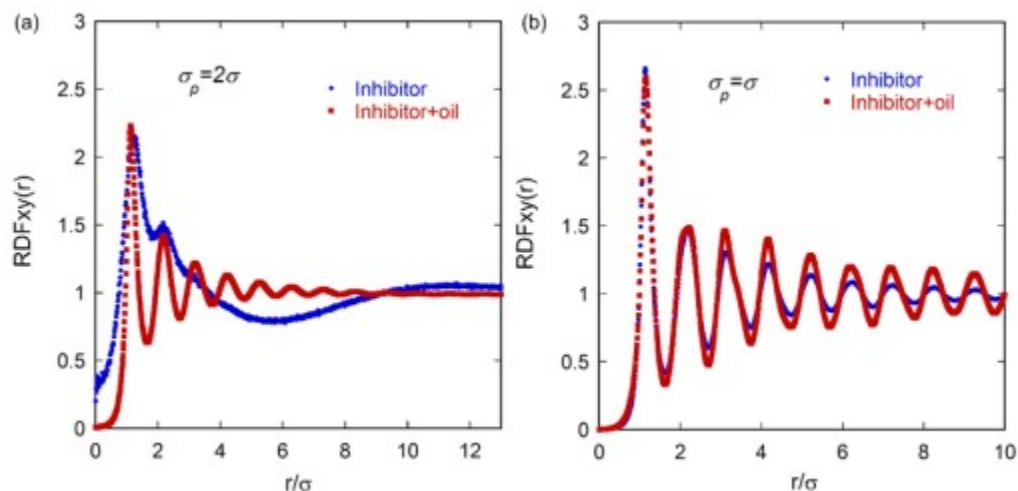


Figure 5.6: Radial distribution function in the XY plane,  $RDF_{xy}(r)$ , of adsorbed molecules in pure inhibitor system (blue) and in inhibitor+oil system (red) for (a)  $\sigma_p = 2\sigma$  and (b)  $\sigma_p = \sigma$ .

It is understood that adsorbed inhibitor films form a hydrophobic barrier over the metal surface and mitigate corrosion. Thus, a larger hydrophobic barrier of the films is preferable. A simple molecular measure of film hydrophobicity can be defined as the fraction of adsorbed molecules with their alkyl tails exposed to the solution. Figure 5.7 shows film hydrophobicity for  $\sigma_p = 2\sigma$  and  $\sigma_p = \sigma$  for the systems with and without oil molecules. It is seen that in a pure inhibitor system, film hydrophobicity is around 0.7, indicating that about 30% of the molecules are adsorbed with their polar head group pointing away from surface. It is often presumed that a SAM layer of adsorbed molecules forms a uniformly hydrophobic layer. Contrary to this, our simulations show that the adsorbed film of inhibitor molecules is patchy with some fraction of polar groups towards the solution. The film hydrophobicity increases to  $\sim 0.9$  with the addition of oil molecules.

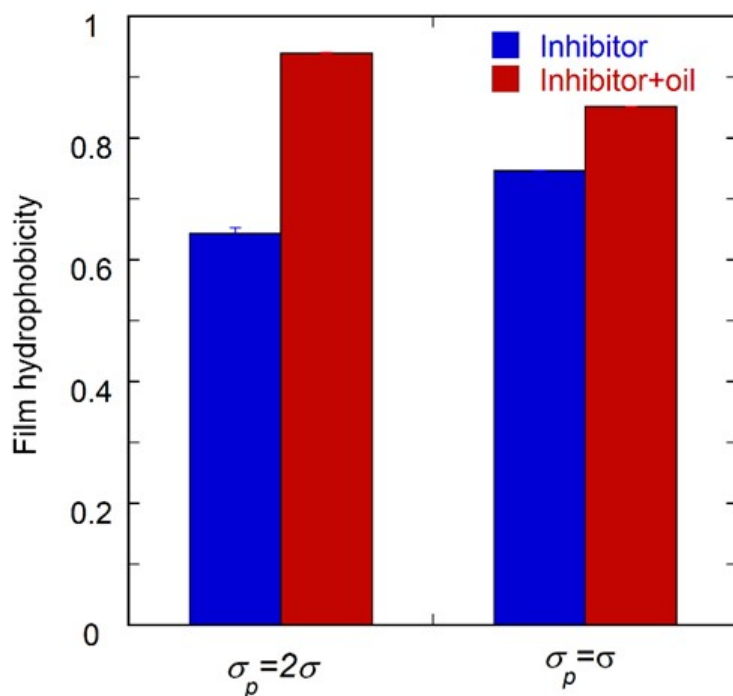


Figure 5.7: Comparison of film hydrophobicity for  $\sigma_p = 2\sigma$  and  $\sigma_p = \sigma$  with oil and without oil molecules present.

The above results show that the entrainment of oil molecules changes the properties of adsorbed films, making them structurally more ordered and more hydrophobic. Thus, our simulation results indicate that the efficiency of corrosion inhibitors should increase when the adsorbed inhibitor films are exposed to oil.

### 5.3.3 Effect of Length of Oil Molecules

In reality, oil molecules in contact with an inhibitor in an aqueous environment are of different molecular sizes. In this section, we discuss the results of how the length of oil molecules affects the entrainment behavior. In these simulations, oil molecules with three different tail lengths, comprising of 10, 19 and 25 beads are compared (oil10, oil19, oil25). The polar head group size is set to  $\sigma_p = \sigma$ . The simulation box is  $20\sigma \times 20\sigma$  in

the XY direction and  $80\sigma$  at the Z direction. 400 inhibitor molecules (20mers) and 400 oil molecules are randomly inserted into the simulation box.

Figure 5.8 shows the total number of molecules adsorbed on the surface at equilibrium. In the system with oil10 and oil19 molecules, the equilibrium adsorption amount is comparable to the pure inhibitor case. However, in the system with oil25 molecules, the total number of adsorbed molecules decreases. This decrease in adsorption is due to aggregation of oil molecules in the bulk phase. With longer tail lengths, the overall interaction between the tails of inhibitor molecules and the oil molecules are stronger, which results in aggregation in the bulk. Although the oil10 and the oil19 systems have similar total adsorption amount, the composition of the adsorbed film is different. Smaller oil molecules have lower hydrophobic interactions, and therefore fewer number of oil10 molecules are co-adsorbed in the corrosion inhibitor layer in comparison to the oil19 system.

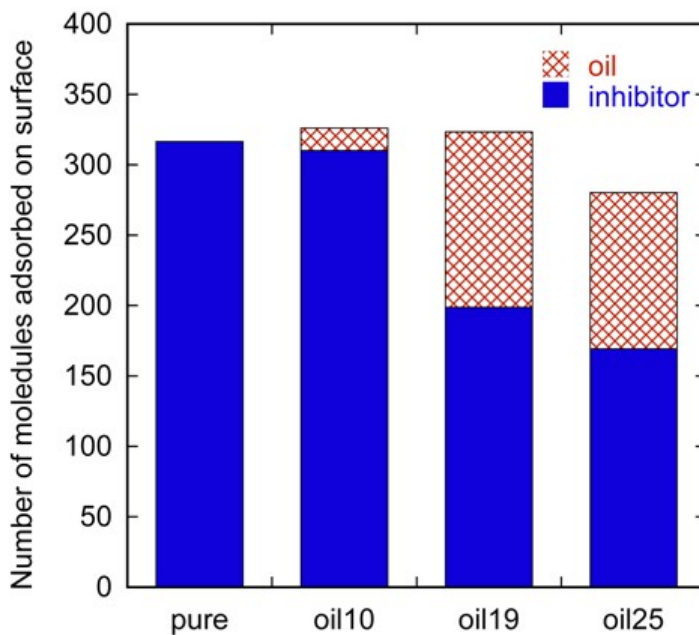


Figure 5.8: Number of inhibitor molecules adsorbed on the surface at equilibrium for a pure inhibitor system, or with oil at molecule chain lengths of 10, 19, and 25.

### 5.3.4 Experimental Confirmation

In 2018, a proprietary project at the ICMT was conducted concurrently with the above mentioned molecular simulations, which focused on comparison of testing methodology, inhibitor efficiency, and inhibitor adsorption/desorption. Information from laboratory testing of a commercial inhibitor (henceforth referred to as proprietary corrosion inhibitor), with and without the presence of hydrocarbon, is provided for tests focused on efficiency and persistency under a specific set of environmental conditions.

In order to test the influence of a hydrocarbon on the efficiency and persistency of corrosion inhibitors, one set of tests was completed without a hydrocarbon present and the second set of tests contained a 1000ppm concentration (2 ml) of LVT 200 oil added on top of the 2 liters of brine used in each experiment. Each experiment was conducted

using a test configuration as shown in Figure 5.9. The system was designed so that a CO<sub>2</sub> purged brine could be pumped from the solution reservoir to the working cell and gravity drained into a CO<sub>2</sub> purged cell. Operating procedures were developed so that the working electrode (RCE) would always remain 100% wetted and never come into direct contact with the oil layer (if present) on top of the brine. The brine, with an ionic strength of 0.5 and temperature of 80°C, was sparged in both glass cells with CO<sub>2</sub> for 2 hours prior to the test to remove oxygen. The brine in both glass cells was adjusted to pH of 6.0 using 1 M NaHCO<sub>3</sub> during the deoxygenation.

Corrosion rate testing was conducted with a mild steel rotating cylinder electrode (RCE) in the 2-liter “working glass cell” (Figure 5.9). The RCEs were made from an API 5L X65 material; each had dimensions of 12 mm outside diameter ×14 mm height, were polished to a 600-grit finish and cleaned in an ultrasonic isopropyl alcohol bath before the tests. In each experiment, the RCE was placed into the glass cell with the purged brine, the CO<sub>2</sub> purged LVT 200 oil was injected on top of the brine (if used), and then rotation was set at ~4000 rpm for a 20 Pa wall shear stress (WSS). Electrochemical connections were made to conduct linear polarization resistance (LPR) measurements for corrosion rate and electrochemical impedance spectroscopy (EIS) measurements were used to determine solution resistance.

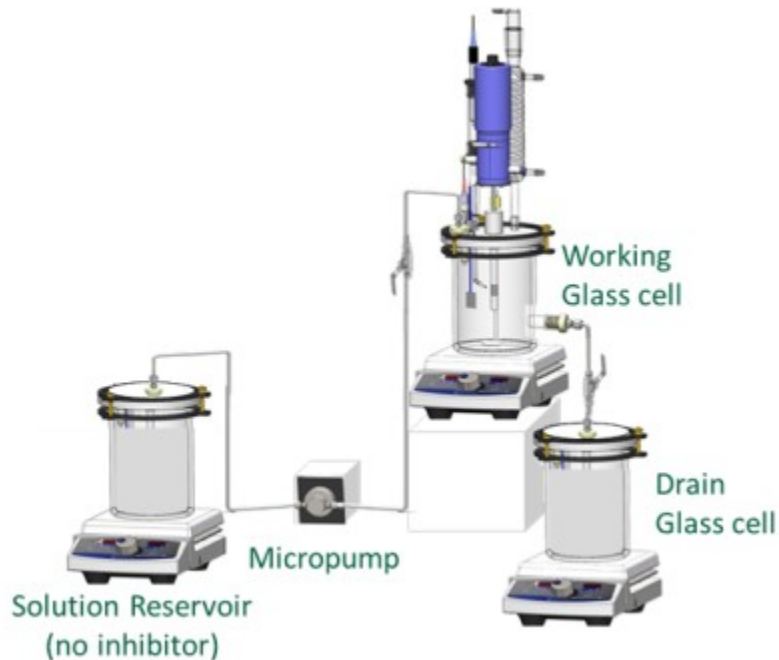


Figure 5.9: Experimental configuration for testing inhibitor efficiency and persistency.

The small amount of oil injected on top of the solution would be partially dispersed into the solution as small droplets at the high rotational speed, but would immediately separate and return to the top of the solution when the rotation was stopped. Experiments conducted without inhibitor added showed no influence of the dispersed LVT oil on the baseline corrosion rate as compared to similar experiments with no inhibitor and no LVT oil present.

EIS measurements were performed at the open circuit potential (OCP) using a potential perturbation with an amplitude of 10 mV root mean squared at a frequency range between 1 Hz to 5 kHz to determine the solution resistance at the beginning of each experiment. Polarization resistance was obtained from LPR. The working electrode was polarized from -5 mV to +5 mV with respect to the OCP at a scan rate of 0.125 mV/s with a sampling period of 2 seconds. Then, the charge transfer resistance (RCT) was obtained

by subtracting the solution resistance from the polarization resistance. Subsequently, corrosion current densities,  $i_{corr}$  were obtained by using a classical Stern-Geary Equation resulting in [109]:

$$i_{corr} = \frac{B}{R_{CT}} \quad (5.6)$$

Where  $B$  is a constant (26 mV/decade for CO<sub>2</sub> corrosion). The current density was then converted into mm/year by using Faraday's law [110]. In the case of the steel corrosion (iron dissolution), the corrosion rate is, CR (mm/year) = 1.159  $i_{corr}$ .

Each test began with 4 hours of pre-corrosion with or without the presence of oil. Electrochemical measurements were started within 10 minutes after the RCE was inserted into solution, as soon as the OCP became stable. After the last LPR measurement for the 4-hour pre-corrosion, the commercial inhibitor was injected on top of the solution for a 100 ppm concentration in the total liquid volume. Each test then continued for an additional 20 hours to observe the decreasing trend of the corrosion rate until a steady state corrosion rate was obtained. The data from this part of the test would be used to focus on inhibitor adsorption and inhibitor efficiency. At 20 hours, the RCE was stopped, stir bar rotation was started in the cell to maintain a fully mixed solution, and increments of ~ 200 ml of brine would be drained and refilled in the working glass cell to achieve a 5 ppm concentration of inhibitor while keeping the RCE continuously water wetted but never directly exposed to the oil layer. The change in inhibitor concentration by this dilution procedure was calculated based on assuming a fully mixed solution after each step in the dilution process. After the drain and re-fill procedure was complete, which required about 5 minutes, the stir bar was stopped and RCE returned to the 20 Pa WSS setting.

Electrochemical measurements for LPR were then continued until a stable corrosion rate was achieved ( $\Delta CR < \pm 0.002 \text{ mm/yr/hr}$ ). The data from this part of the test would focus on inhibitor persistency and final corrosion rate. Each test, with and without a

hydrocarbon present, was repeated twice and the graphic results shown in Figure 5.10 and Figure 5.11 represent the average of the two experiments with appropriate error bars.

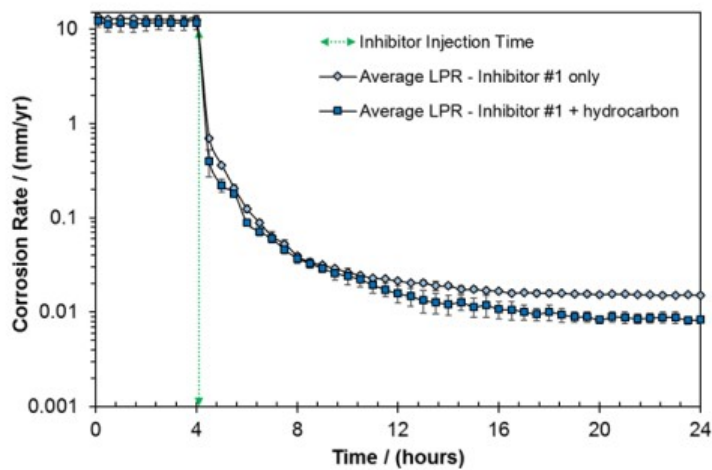


Figure 5.10: Inhibitor adsorption experiments with Inhibitor # 1 conducted with and without the presence of a hydrocarbon (80°C, pH 6.0, 0.5 ionic strength brine, RCE at 20 Pa WSS, 1000 ppm LVT 200).

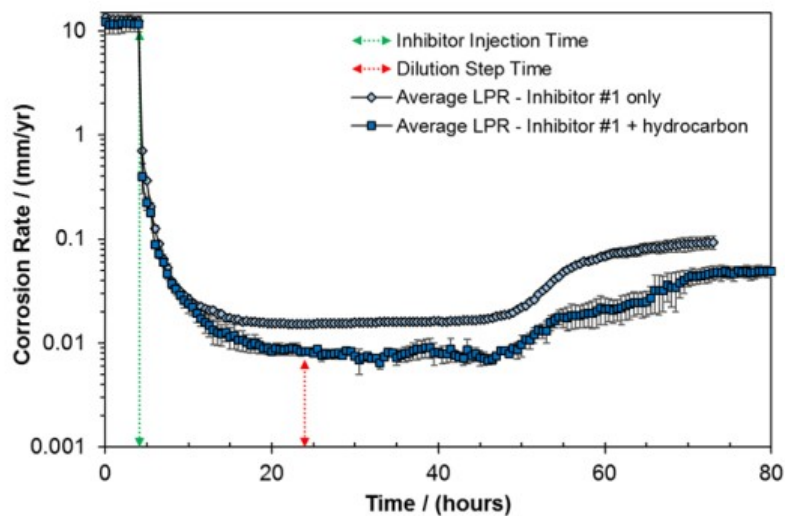


Figure 5.11: Inhibitor adsorption and dilution experiments with Inhibitor #1 conducted with and without the presence of a hydrocarbon (80°C, pH 6.0, 0.5 ionic strength brine, RCE at 20 Pa WSS, 1000 ppm LVT 200).

The data for the proprietary corrosion inhibitor tests is shown in Figure 5.10, Figure 5.11, and the composition as provided in the Material Safety Data Sheet (MSDS) is shown in Table 5.1.

Table 5.1: Proprietary corrosion inhibitor MSDS listed components

| <b>Inhibitor #1 components</b> | <b>% content</b> |
|--------------------------------|------------------|
| Methanol                       | 30% - 60%        |
| Substituted aromatic amine     | 10% - 30%        |
| Quaternary ammonium compound 1 | 10% - 30%        |
| Fatty acid                     | 5% - 10%         |
| Quaternary ammonium compound 2 | 5% - 10%         |
| 2-mercaptoethanol              | 5% - 10%         |
| Diethanolamine                 | 1% - 5%          |
| Isopropanol                    | 1% - 5%          |
| Oxyalkylate                    | 1% - 5%          |
| Heavy aromatic naphtha         | 1% - 5%          |
| Naphthalene                    | 0.1%- 1%         |

The data in Figure 5.10 shows the trend for the addition of the proprietary corrosion inhibitor. Without the hydrocarbon present, the addition of the inhibitor provided a corrosion inhibition efficiency of 99.88%. The average corrosion rate during pre-corrosion for the experiments without hydrocarbon was  $12.4 \pm 1.6$  mm/year and the inhibited corrosion rate was  $0.015 \pm 0.001$  mm/yr. With the hydrocarbon present, the addition of inhibitor provided a corrosion inhibition efficiency of 99.93%. The average corrosion rate during pre-corrosion for the experiments with hydrocarbon was  $11.7 \pm 1.9$  mm/year and the inhibited corrosion rate was  $0.008 \pm 0.001$  mm/year. The presence of LVT 200 decreased the corrosion rate in the presence of an inhibitor film from  $0.015 \pm 0.001$  mm/yr to  $0.008 \pm 0.001$  mm/yr, which is a decrease in the corrosion rate by 46.7%.

The data in Figure 5.11 shows both the addition and dilution parts of the full experiment. The dilution procedure was carried out to obtain approximately 5 ppm of proprietary corrosion inhibitor. The final corrosion rate after dilution to 5 ppm for experiments without hydrocarbon were  $0.093 \pm 0.013$  mm/year, while in those same type of tests with hydrocarbon present, it was lower approximately by a factor of two:  $0.049 \pm 0.006$  mm/yr. In terms of inhibitor efficiency, the experiment with hydrocarbon had a 99.58% efficiency as compared to a 99.25% efficiency without hydrocarbon present.

Persistency of the inhibitor in these tests was defined by when the corrosion rate begins increasing much more than the random variation of the stable corrosion rate measured before the dilution procedure. For proprietary corrosion inhibitor, the persistency of the inhibitor without hydrocarbon present was about 22 hours while the persistency of the inhibitor with hydrocarbon present was about 26 hours. One can also argue that both tests with proprietary corrosion inhibitor show a continued persistency as previous tests with addition of only 5 ppm of proprietary corrosion inhibitor had a stable corrosion rate of  $0.140 \pm 0.001$  mm/year after 20 hours. This could also be an indication of the precision of the dilution procedure, which is very similar in the tests with no hydrocarbon, where the tests with hydrocarbon could indicate some influence of partitioning equilibrium between the oil phase and the solution occurred.

#### **5.4 Conclusion**

Previous experimental results have shown that the addition of oil molecules can reduce corrosion rate by enhancing the efficiency of an inhibitor film, although these tests did not provide any molecular-level understanding of why and how these oil molecules influence corrosion inhibitor adsorption for mitigation of corrosion. In this study, we have used molecular simulations to study how oil molecules affect adsorption behavior and characteristics of adsorbed inhibitor films. We found that, even though oil molecules

do not interact with the metal surface, they can be co-adsorbed in the inhibitor layer because of lateral hydrophobic interactions between the oil molecules and the alkyl tails of inhibitor molecules. In addition, we observed an interesting morphological transition in the adsorbed films wherein cylindrical micelles of adsorbed inhibitors get transformed into planar SAMs. This transition results in a significant increase in the adsorption of molecules on the surface. Different lengths of oil molecules have different entrainment tendencies. Large oil molecules lead to aggregation of molecules in the bulk phase, thereby reducing adsorption, while smaller oil molecules have little tendency to be co-adsorbed in the inhibitor film. Our experiments have revealed that the presence of a hydrocarbon phase is beneficial in corrosion mitigation for a commercial inhibitor. In the experiments, the inhibitor layer adsorbed at the metal surface would be expected to contain some of the hydrocarbon phase because of the increase in the final inhibition efficiency. Since the molecular model is focused on the diffusion boundary layer right next to the metal surface, the mechanisms portrayed by the molecular model are confirmed to be correct.

**Acknowledgement.** This work was supported by the NSF CBET grant 1705817. The experiments were performed as part of a proprietary British Petroleum (BP) project at the Institute of Corrosion and Multiphase Technology (ICMT) that focused on comparison of testing methodology, inhibitor efficiency, and inhibitor adsorption/desorption, which produced a proprietary document: J. Dominguez Olivo, C. Prieto, B. Brown, S. Netic, Testing Methodology for Inhibitor Evaluation, Proprietary testing on inhibitor persistency. Since the project also included the testing of commercial inhibitors in the presence of oil, permission for publication was requested and was granted by the proprietary project lead at BP, Will Durnie, who is the Principle Corrosion Engineer of BP with research focus on inhibitor use, efficiency and persistency. The authors are grateful to BP for granting us the permission to include these experimental results in this publication. The authors also thank researchers at the ICMT for useful discussions. XK thanks the support of Ohio University

Graduate College Fellowship for the year 2018-19. Computational resources for this work were provided by the Ohio Supercomputer Center and NSF XSEDE grant DMR190005.

## 6 ADSORPTION BEHAVIOR OF CORROSION INHIBITORS ON HETEROGENEOUS METALLIC SURFACES STUDIED USING MOLECULAR SIMULATIONS

### 6.1 Introduction

In previous work, adsorption of surfactants was studied on a uniform metal surface. However, in field conditions, the steel surface is not uniform as it is often covered by a layer of corrosion products formed as a consequence of the corrosion process [111]. As a result, the performance of corrosion inhibitors varies with different microstructures of the corrosion products as well as in varying field conditions [112–114]. While most studies have reported that an increase in the pre-corrosion time results in the decrease of corrosion efficiency [112, 113, 115], synergistic interactions between the corrosion inhibitor and corrosion product that help with erosion-corrosion protection have also been reported [116]. To better understand how pre-corrosion or a non-uniform metal surface changes the adsorption behavior of corrosion inhibitors from a molecular perspective, heterogeneous surfaces are introduced in the simulation system.

### 6.2 Simulation System and Methods

The same coarse-grained bead-spring model of corrosion inhibitor molecules is used as in our previous studies [90]. All quantities used in the simulation system are defined in reduced units [65], and the thermal energy  $K_B T$  is taken as the unit of energy,  $K_B T = 1$  and the size of the alkyl tail bead,  $\sigma$  is taken as the unit of length. The simulation box is of the size  $20 \times 20$  and periodic in the  $x$ – $y$  directions. The metal surface is at  $z = 0$ , and the box size is 40 at the  $z$  direction. 400 inhibitor molecules are randomly inserted into the simulation box. To model a heterogeneous surface, part of it is modeled as a metal patch with attractive interactions with the polar bead of the corrosion inhibitor molecules as before. The rest of

the surface is considered to have no interactions with the molecules except for their hard wall repulsion. The attractive interaction between the metal patch and the polar bead of the inhibitor molecule is modeled by a 9-3 interaction potential. Two systems are studied: in the first system, one circular-shaped metal patch is considered. In the second system, many circular metal patches are considered. In fact, because of periodic boundary conditions in the  $x$ - $y$  directions, the two systems are actually the same system but with the metal patches at different distances from each other. All simulations are conducted using the Large-scale Atomic/Molecular Massively Parallel Simulator (LAMMPS) package [70].

## 6.3 Results and Discussion

### 6.3.1 Single Metal Patch System

The circular-shaped metal patch is placed at the center of the  $z = 0$  face of the simulation box. The radius of the patch is varied from 1 to 4.

#### 6.3.1.1 Adsorbed Amount

Figure 6.1 shows the total number of molecules adsorbed on surface at equilibrium as a function of the area of the metal patch. The blue line shows the simulation results, and the red line shows the theoretical estimate of the adsorption amount, wherein it is assumed that the corrosion inhibitor molecules only adsorb on the metal patch with the packing density equal to that of the SAM [90]. It is observed that the number of adsorbed molecules is significantly larger than the theoretical estimate. Since the surface other than the metal patch has no interaction with the corrosion inhibitor molecules, this result indicates that the molecules can adsorb outside of the metal patch due to the lateral tail-tail interactions.

Figure 6.2(a) shows the percentage of surface covered by inhibitor molecules as a function of the metal patch surface area. As the size of the metal patch increases, the coverage also increases, and at  $r = 4$ , full coverage is achieved. It is interesting to observe

that even with a small metal patch, the inhibitor molecules are able to fully adsorb onto the surface and form a SAM. Figure 6.2(b) shows a snapshot of the equilibrium configuration of the SAM with the metal patch shown in yellow.

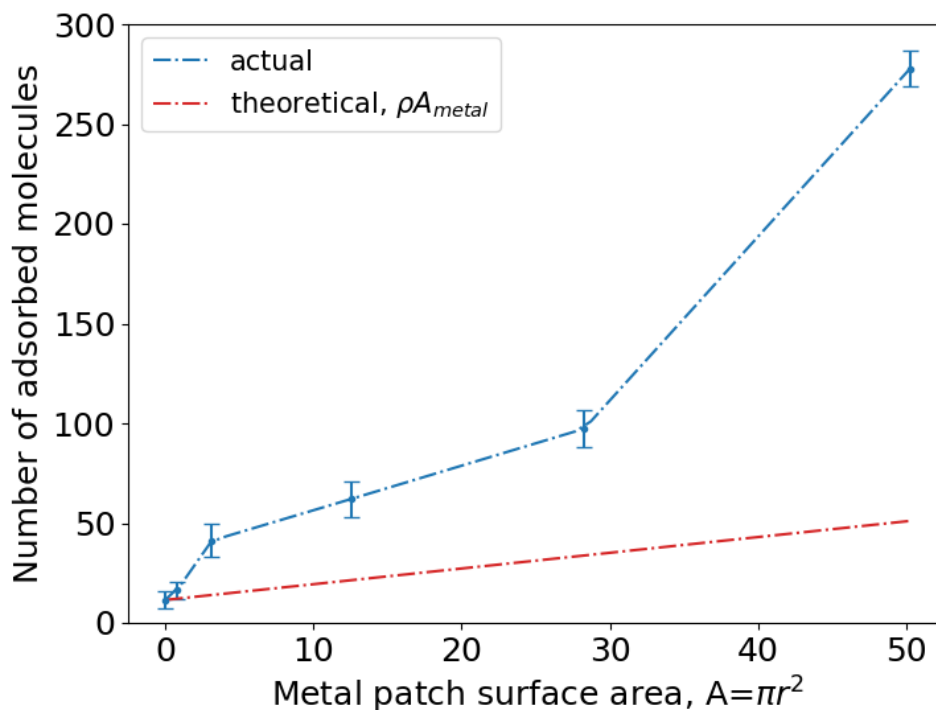


Figure 6.1: Number of adsorbed molecules  $N$ , as a function of the surface area of the metal patch. The theoretical line shows the number of molecules that would adsorb if they only adsorb on to the metal patch area.

### 6.3.1.2 Structure of the Adsorbed Corrosion Inhibitor Film

Figure 6.3 shows the fraction of adsorbed molecules with their polar group pointing toward metal surface,  $f$ , as a function of the radius of the metal patch. Inhibitor molecules form a SAM in both systems shown here. For the metal patch, the  $f$  decreases as

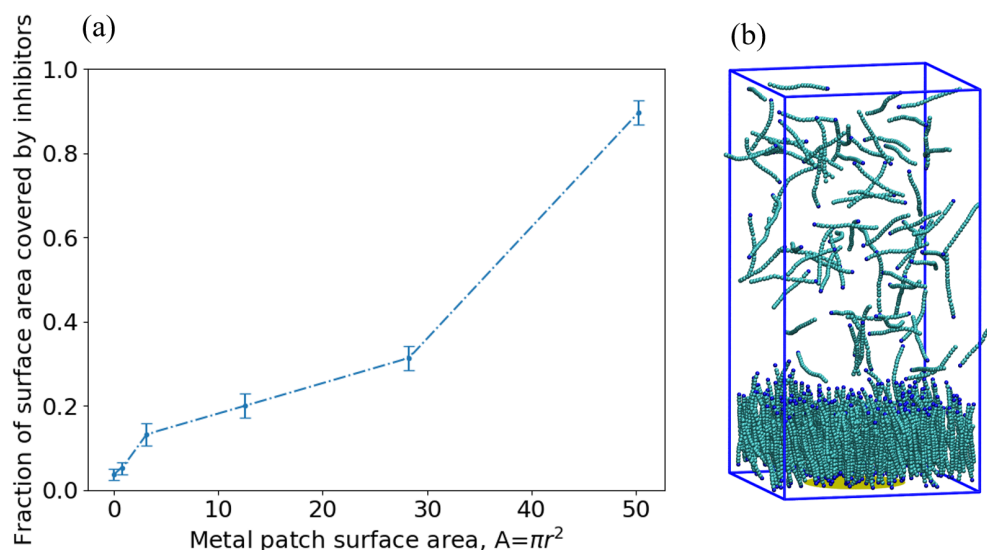


Figure 6.2: (a) Fraction of the surface covered by inhibitor molecules as a function of the surface area of the metal patch.(b) Snapshot of the equilibrium configuration for the metal patch with radius  $r = 4$ .

compared to the full metal surface. This is expected as in the case of the metal patch, the molecules outside of the patch adsorb due to the lateral tail-tail interactions, and therefore are indifferent as to the orientation in which they adsorb in the SAM.

## 6.3.2 Multi-patch System

In this section, we discuss results of the system in which there are four circular-shaped metal patches of radius 0.5 or 1 in the simulation box.

### 6.3.2.1 Adsorbed Amount

Figure 6.4 shows a bar plot of the number of adsorbed molecules on metal surface as a function of the metal patch surface area. Comparing to results from the bulk simulation where the surface has no interaction with corrosion inhibitor molecules, the adsorption

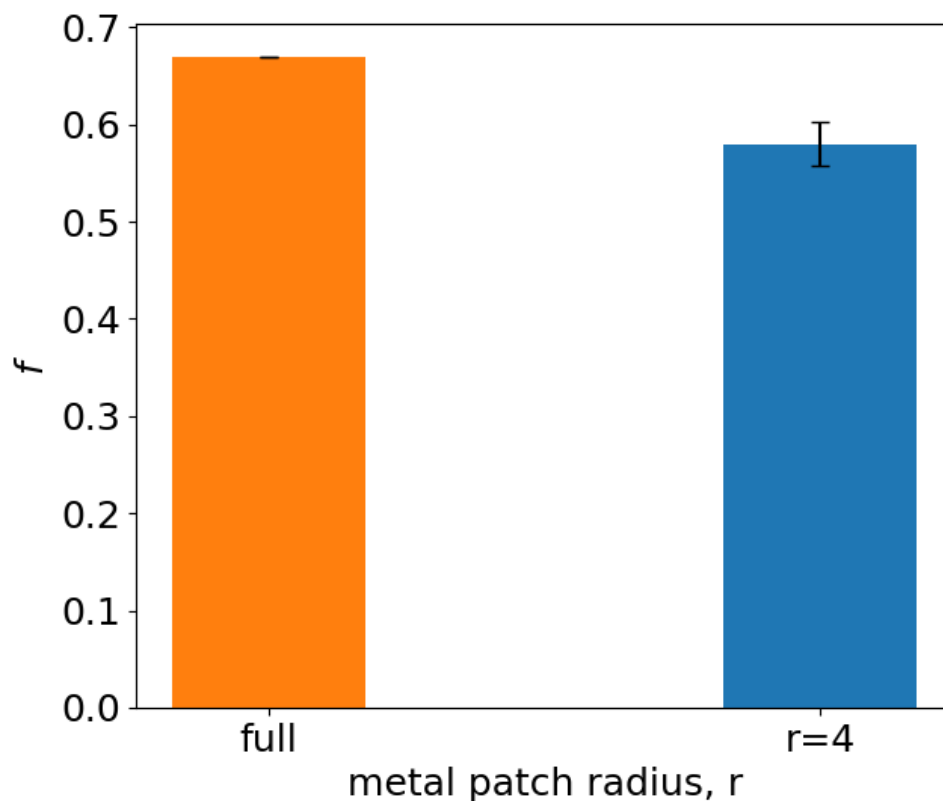


Figure 6.3: Fraction of adsorbed molecules with their polar group pointing toward surface.

amount in these systems shows that with a very small metal patch area as well, corrosion inhibitor molecules can adsorb, eventually forming a SAM and covering the entire surface. The diameter of the polar bead of the inhibitor molecule is  $\sigma = 1$ , so for a metal patch of radius = 0.5, only one inhibitor molecule should be able to adsorb onto the patch. However, a SAM forms on the surface. This indicates that inhibitor molecules can adsorb even when there are a few anchoring sites on the surface, and the lateral hydrophobic interactions are helping the inhibitor molecules to adsorb onto the surface.

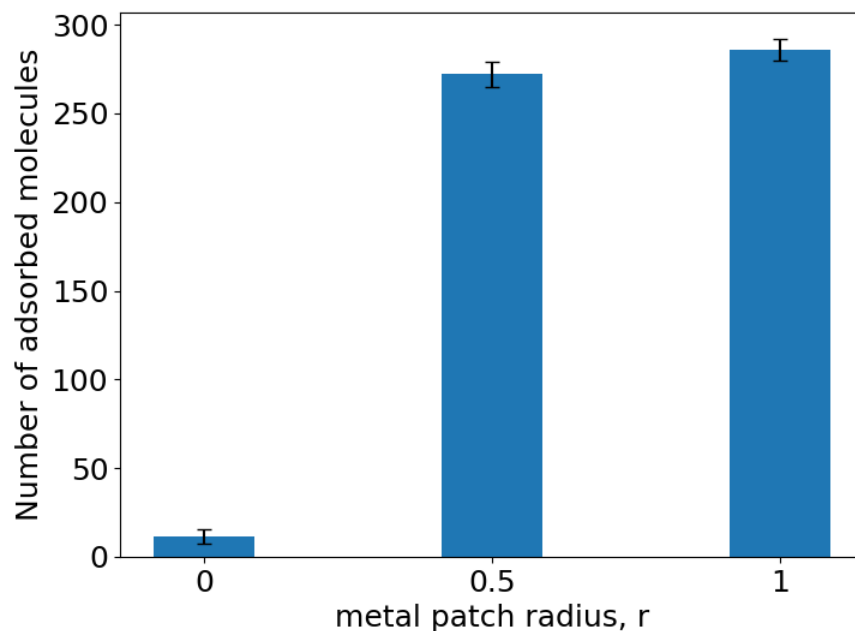


Figure 6.4: Number of adsorbed molecules  $N$ , as a function of the surface area of the metal patch.

### 6.3.2.2 Film Structure

Figure 6.5 shows the fraction of adsorbed molecules with their polar group pointing toward metal surface,  $f$ , as a function of the radius of the metal patch. Compared to the full metal surface,  $f$  decreases and is only around 0.5. This is because with only a few small metal patches on the surface, there is no preference for the molecules to adsorb with their polar head pointing toward surface. The adsorbed molecules have equal probability to be pointing toward surface or the solution.

### 6.3.3 Distance between Metal Patches Play an Important Role in Adsorption

Due to the periodic boundary conditions applied in both systems, the two systems basically represent the same system wherein there are circular metal patches at certain

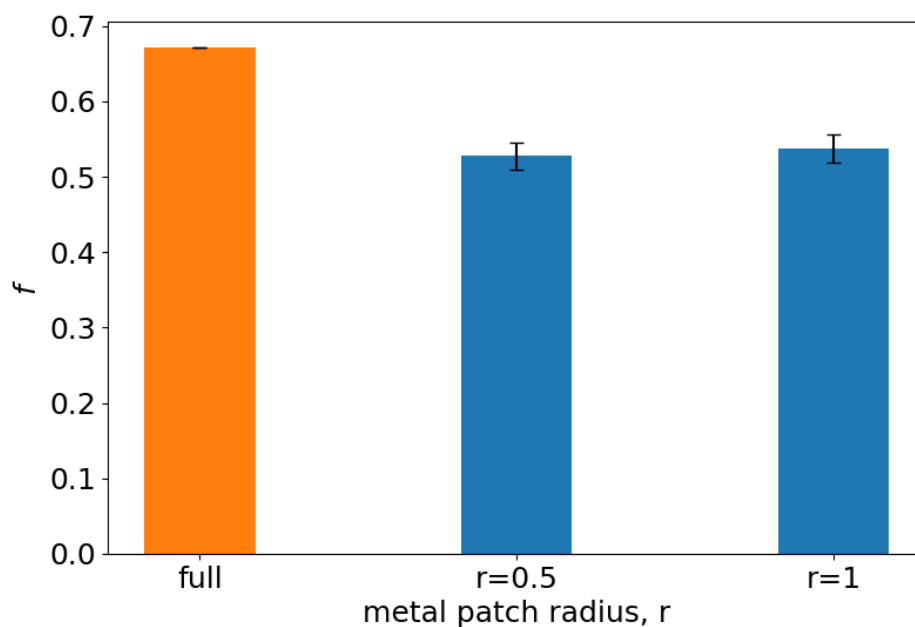


Figure 6.5: Fraction of molecules with their polar group pointing toward surface.

distances from each other. From the above analysis, it is observed that the inhibitor molecules can form SAM in the multi-patch system even when the radius of the metal patch is small. Therefore, the distance between the metal patches may be playing an important role in governing the formation of the SAM. To investigate the effect of distance, the number of adsorbed molecules in both the system are plotted together as a function of the distance between the metal patches, as shown in Figure 6.6. In the Figure 6.6, it is observed that the when the metal patches are close to each other, a SAM of inhibitor molecules is formed. The size of the metal patch is less significant. Molecules initially adsorb on the metal patch(es) due to the strong affinity between the polar head and the patch. After the initial adsorption, the lateral hydrophobic interaction between the alkyl tails drive the adsorption. If the metal patches are close to each other, then as long as there are a few anchoring sites on the surface (metal patch area), the molecules can adsorb due

to the lateral tail-tail interactions. Also because the metal patch regions are close to each other, the inhibitor molecule clusters that is already formed on the surface can merge and fully cover the surface.

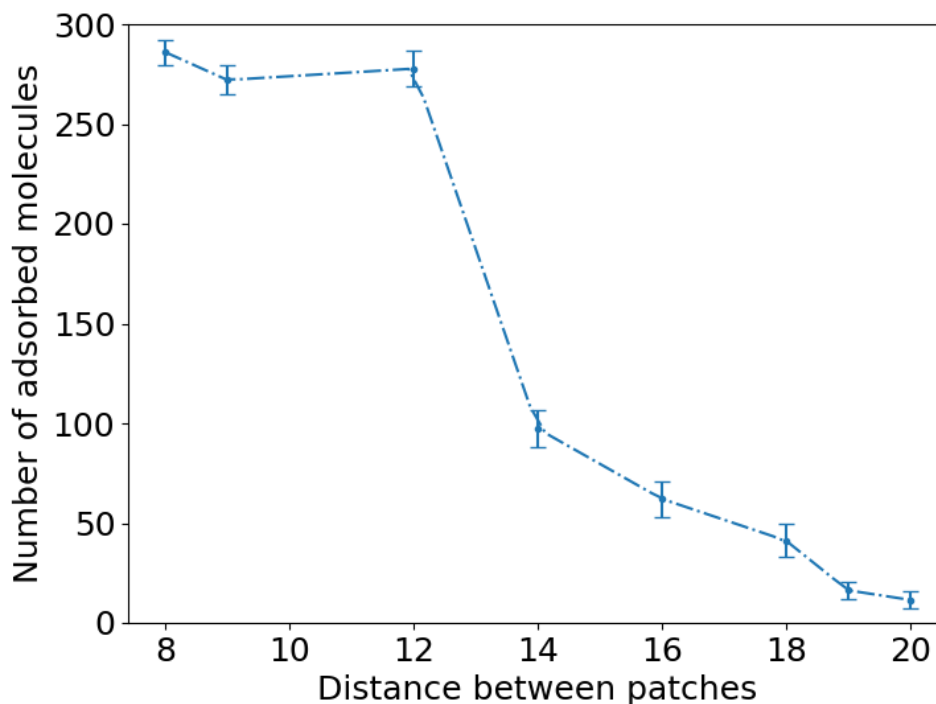


Figure 6.6: Number of adsorbed molecules as a function of distance between patches.

#### 6.4 Conclusion

Previous studies have shown that when a surface is pre-corroded and/or nonuniform, the inhibition efficiency is different as compared to a pristine metal surface. In this study, a heterogeneous surface is introduced to study the adsorption of inhibitor molecules on such surfaces and the characteristics of the adsorbed inhibitor films. It was found that, even though large parts of the surface do not have direct affinity for the inhibitor molecules,

the molecules can still achieve full adsorption coverage because of the lateral hydrophobic interactions between their alkyl tails. In addition, the SAM formed has a good fraction of molecules pointing toward the solution. Furthermore, we find that the distance between the metal patches is an important factor governing the adsorption amount. When the distance between metal patches is small, inhibitor molecules have a tendency to form SAM. Finally, the size of metal patches is found to be not as important. In the atomic force microscopy experiments conducted at ICMT, it has been reported that inhibitor molecules do adsorb on the parts of the surface with a corrosion product. Furthermore, different magnitude of force is required to remove inhibitor molecules from the corrosion product part and the metal part of the surface. Our molecular simulation work provides insights as to how inhibitor molecules are able to adsorb on areas with the corrosion product. Furthermore, since the lateral hydrophobic interactions are weaker than the direct interaction between the inhibitor molecules and the metal surface, these molecules are removed relatively easily.

## 7 SALT- AND pH-DEPENDENT VISCOSITY OF SDS/LAPB SOLUTIONS: EXPERIMENTS AND A SEMIEMPIRICAL THERMODYNAMIC MODEL<sup>8</sup>

### 7.1 Introduction

A large number of commercial personal care formulations (e.g., shampoos, body-washes) use a combination of an anionic surfactant like sodium lauryl or laureth sulfate (SLS or SLES) with the zwitterionic cocamidopropyl betaine (CAPB) as a co-surfactant (10-20% of the total amount of surfactant). In recent years, the push for milder, sulfate-free and natural surfactants has expanded the formulation space to a much larger chemical space [117, 118]. A model based way to develop formulations is therefore critical for rapid and efficient prototyping. Importantly, successful commercial formulations have to be optimized for multiple endpoints - suitable viscosity and rheology, lather, cleansing efficiency, coacervation phase behavior with cationic polymers [119–122], etc. Hence, a suite of theoretically rigorous models that are also practical enough to be used in industry are needed - by practical, we mean that it requires relatively few parameters, and that it should be easy to measure/infer these parameters in an industrial setting for a wide range of surfactant combinations and ratios, pH, and ionic strength.

In this contribution, we focus on an important metric for the consumer acceptability of commercial formulations - the zero shear viscosity, which is a measure of product texture. For historical SLS rich formulations (with some CAPB), simple salt (NaCl) is used to thicken formulations and achieve a desired viscosity. Salt reduces electrostatic repulsion between the surfactant headgroups, which promotes the elongation of surfactant micelles,

---

<sup>8</sup> Adapted with permission from Jamadagni, S. N., Ko, X., Thomas, J. B., & Eike, D. M. (2021). Salt- and pH-Dependent Viscosity of SDS/LAPB Solutions: Experiments and a Semiempirical Thermodynamic Model. *Langmuir*, Copyright(2021) American Chemical Society.

and transforms spherical micelles to worm-like micelles [123, 124]. At sufficiently high salt concentrations, the worm-like micelles transform into branched micelles and the viscosity again reduces [125–127]. While these principles are well understood, we lack a quantitative model to predict viscosity as a function of composition, especially over a wider range of SLS/CAPB ratios (where as we discuss below, pH effects also become important).

The rheology of worm-like micellar solutions depends on the structure and dynamics of the elongated micelles, similar to those of long polymers [128, 129]. Extending the work of Cates and collaborators [128], Ron Larson and co-workers have developed sophisticated models of the full frequency dependent linear visco-elastic spectrum [*i.e.*,  $G'(\omega)$ ,  $G''(\omega)$ ] as a function of structural and dynamical parameters such as the micelle persistence length and radius, and the micelle breakage and reptation time scales [130, 131]. These models can be used in forward (*i.e.*, use those parameters to predict the linear viscoelastic spectrum) or in reverse modes (*i.e.*, use rheological measurements to infer those parameters using the POINTER algorithm [130]). However, linking the structural and dynamical parameters of the micelle to its chemical composition in an easily accessible framework to enable product development is difficult. Explicit all-atom [132, 133] and coarse-grained molecular dynamics (MD) [134, 135] and dissipative particle dynamics (DPD) simulations [136–141] have shown promise; but the ability to use them for rapidly scanning a large formulation space remains challenging for two reasons: the parameterization of surfactant headgroups and the well-known limitations of the lengthscales and timescales accessible to molecular and coarse-grained simulations.

Hence, fast, non-simulation based methods are attractive; two of the most popular approaches are the regular solution theory (RST) approach pioneered by Holland and Rubingh [142, 143] and the more complex molecular thermodynamic (MT) approach pioneered by Nagarajan and co-workers [144, 145] and Blankschtein and co-workers [146–148]. In the simpler RST approaches, the excess chemical potentials of the surfactants in

the micellar pseudo-phase are modeled with a simple Margules model, parameterized by a single  $\beta$  parameter between each pair of surfactants that captures the non-ideality of the interactions. The  $\beta$  parameter can be estimated by fitting experimental CMC or surface tension data to the theory.

In the MT approach, the transfer free energy of a surfactant molecule from its monomeric state in aqueous solution into the micelle is modeled. For this, the transfer free energy is broken up into different contributions - entropy of the alkyl tails, hydrophobic, steric, an interfacial tension etc. and each term modeled suitably. In a series of recent papers, Danov et. al. [149–152] have used a sophisticated version of such a theory to calculate the transfer free energy into the hemispherical end-cap and cylindrical region of a non-ionic and ionic spherocylindrical micelles. The difference,  $\mu_{sph} - \mu_{cyl}$ , is the driving force for micelle elongation. This approach is promising but could be challenging to extend to complex mixtures of ionic surfactants, and to model the effect of pH (for titrable surfactants). Further, it also requires a large number of parameters (e.g., to describe tail and headgroup geometry, chain packing, ion condensation in the Stern layer, activity coefficient models for ions at high ionic strengths in the micelle hydration shell etc.) which can be challenging to obtain for different surfactant architectures. Hence, as described below, we have chosen the simpler RST of Rubingh and Holland [142] to model the thermodynamics of mixed micelles, with the  $\beta$  parameter determined experimentally or estimated using suitable heuristics.

In this chapter, we show that we can link the zero shear viscosity to composition (surfactant ratios, pH, salt) explicitly using an extended or augmented RST model, where RST is extended with (i) the Henderson-Hasselbalch equation to describe the pH dependent protonation-deprotonation equilibria of monomers in solution (as in Rathman and Christian for pure dodecyl amine oxide) [153] and (ii) the effect of salt is handled at a simple Poisson-

Boltzmann level. While we have used RST as the thermodynamic framework here MT or other simulation based approaches can also be used in principle.

In the framework of Cates and co-workers, the zero shear viscosity is determined by the timescales for relaxation of micelles by reptation (akin to normal polymers) and breakage, and is dominated by the smaller of these timescales [128, 154]. Since (i) breakage rates are more amenable to relate to a molecular thermodynamic framework (discussed below) and (ii) fits of rheological data by the POINTER algorithm [130] by our collaborators, Vu et. al. [155] showed that small changes in composition, pH and salt that affect viscosity significantly is because of changes in the dynamics of micelle breakage, we explored the correlation between thermodynamic parameters that affects micelle breakage with the experimental zero shear viscosity measurements.

A historically relevant work on micelle breakage is the theoretical framework of breakage of single component spherical micelles by Aniansson and Wall [156, 157]. Aniansson and Wall use the analogy of a driven diffusion in the micelle aggregation number space to describe the population flux between surfactant monomers and full micelles. In this model, both surfactant monomers and fully formed micelles exist in large numbers. However, micelles form and break up by step-wise association/dissociation of individual surfactant monomers, and the concentration of these pre-micellar aggregates is very small and there exists pre-micellar aggregates of a critical size that are the ‘transition state’. If the aggregation number exceeds this, the process proceeds to form full micelles; otherwise the pre-micellar aggregate disintegrates into monomers again [158]. Importantly, due to the diffusion-driven nature of micelle formation, the rate of micelle breakage (with a time constant commonly referred to as  $\tau_2$ ) depends strongly on the free monomer concentration (which is the same as the critical micelle concentration (CMC) for single surfactants) - i.e.,  $\tau_2 \sim CMC^{-n}$  with  $n > 1$ . We anticipate that the breakage of worm-like micelles may show a similar relationship with a thermodynamic parameter like the CMC, and indeed there is

evidence that this is true in simple systems [159, 160]. This motivated the development of a thermodynamic model for activity coefficients and free monomer concentrations of the different surfactants in mixed micelles as a function of the pH and salt and an attempt to correlate these quantities with the zero shear viscosities.

The rest of the paper is organized as follows. First we describe our thermodynamic model for surfactant activity coefficients. We then present experimental results of the salt and pH dependent viscosity of SDS/LAPB mixtures over a wide range of SDS/LAPB ratios, and associated NMR experiments that track the protonation state of the zwitterionic betaine. We then show that the excess free energies of the surfactants is an excellent predictor of the viscosity of these solutions. Finally, we suggest ways to generalize this approach using Bayesian models.

## 7.2 Thermodynamic Model

In this section, we briefly review the RST theory for mixed micelle thermodynamics, and then describe our thermodynamic model in detail. If titrable surfactants are present, the model provides the activity coefficients as well as the amounts of the deprotonated and protonated states of the surfactant - i.e., the complete composition of the micelle. A summary of the different physical relationships is provided in Table 7.1 with further details discussed below.

### 7.2.1 Overview of Mixed Micelle Thermodynamics

The basics of this theory for mixtures of non-titrable surfactants has been covered in detail in many papers starting with Holland and Rubingh [142, 143]. Since we are concerned with prediction of micellar properties at high surfactant concentrations, we assume that overall composition ( $\alpha_i$  in the notation of Holland et. al. [142]) and micellar composition ( $x_i$ ) are identical. At low total surfactant concentrations ( $\sim$ CMC),

an additional mass balance constraint has to be used to solve the set of equations below as the mole fractions in the micelle and solution pseudo-phases can differ significantly.

At equilibrium the thermodynamic activities of the surfactant in the monomer and the micellar phase are equal.

$$a_{i,mon} = a_{i,mic} \quad (7.1)$$

The activity in the micelle is calculated using the ‘ $\beta$ ’ parameter model for the activity coefficient,  $\gamma_i$ .

$$a_{i,mic} = \gamma_{i,mic} x_{i,mic} \quad (7.2)$$

where  $x_i$  is the mole fraction of the  $i$ th surfactant in the micelle. The  $\beta$  parameter model is essentially a multi-component Margules model for the excess Gibbs free energy:

$$\frac{G^{ex}}{RT} = \sum_{i<j}^n \beta_{ij} x_i x_j \quad (7.3)$$

$$\ln(\gamma_i) = \left( \sum_{j=1, j \neq i}^n \beta_{ij} x_j \right) - \frac{G^{ex}}{RT} \quad (7.4)$$

The activity of the surfactant monomer is given by:

$$a_{i,mon} = \frac{c_{i,mon}}{CMC_i} \quad (7.5)$$

where  $CMC_i$  is the CMC of the  $i$ th surfactant. If there are no titrable surfactants and the concentration of surfactants is high, the mole fraction of surfactants in the micelle,  $x_{i,mic}$ , is the same as the overall composition. Then, Eqn. 7.2 and Eqn. 7.3-7.4 can be used to calculate the activities of the surfactant and Eqn. 7.5 can be used to calculate the free monomer concentrations if the CMCs of the pure surfactants are known.

## 7.2.2 Titrable Surfactants at High Total Surfactant Concentration

If the surfactant blend contains one or more titrable surfactants, the mole fractions of the protonated ( $HS$ ) and deprotonated ( $S^-$ ) surfactants in the micelle depend on pH.

Thus solving for the composition of the micelle requires a self-consistent solution of the following equations for each titrable species. The activities of the monomer in the solution phase are given by [142]:

$$a_{S_j^-,mon} = \frac{c_{S_j^-,mon}}{CMC_{S_j^-}} \quad (7.6)$$

$$a_{HS_j,mon} = \frac{c_{HS_j,mon}}{CMC_{HS_j}} \quad (7.7)$$

The activities of surfactants in the micellar phase can be calculated via the  $\beta$  parameter model with the pH dependent mole fractions  $x_{S_j^-,mic}$  and  $x_{HS_j,mic}$  being the unknowns to solve for. The mass balance constraint implies  $x_{S_j^-,mic} + x_{HS_j,mic} = x_{S_j^{total},mic}$  - *i.e.*, there is only one non-trivial unknown for each titrable species ( $x_{S_j^-,mic}$ ). These set of equations can be closed by equating the chemical potentials in the micellar and monomer phase using the bulk  $pK_a$  and the Henderson-Hasselbalch Equation:

$$\frac{c_{S_j^-,mon}[H^+]}{c_{HS_j,mon}} = K_a \quad (7.8)$$

$$\implies \frac{c_{S_j^-,mon}}{c_{HS_j,mon}} = 10^{pH-pK_a} \quad (7.9)$$

This yields the closure for the self-consistent solution of the  $\beta$  parameter model:

$$\frac{a_{S_j^-,mon}}{a_{HS_j,mon}} = \frac{a_{S_j^-,mic}}{a_{HS_j,mic}} = \left( \frac{CMC_{HS_j}}{CMC_{S_j^-}} \right) 10^{pH-pK_a} \quad (7.10)$$

Equations 7.2, 7.3, 7.4 and 7.10 can thus be solved with an iterative least-squares solver to yield the pH dependent composition of a mixed micelle comprising an arbitrary number of titrable components, and the free monomer concentrations can then be obtained from Eqn. 7.5.

### 7.2.3 Effect of Added Salt

To model the effect of added salt, we need to consider its effect on the excess chemical potential (or activity coefficient) of both surfactants in their monomers (and corresponding

pure micellar phases) and in the mixed micellar pseudo-phase. We begin with the effect on the surfactant monomers:

### 7.2.3.1 Pure Component CMCs

The CMC and therefore the free monomer concentrations of ionic surfactants reduces with increasing salt concentration, and this is primarily an electrostatic effect (the hydrophobic driving force for micellization also increases slightly with increasing salt level). Following Healy et al.[161], the effect of added salt can be modeled by considering the change in *electrochemical* potential of the ionic surfactant in the pure micelle when salt is added:

$$\delta\mu^{ex} \approx zF\delta\psi \quad (7.11)$$

and  $z$  is the valence and  $F = eN_a = 96,485$  C/mol is the Faraday constant and  $\delta\psi$  is the change in the electric potential at the micelle water interface. There will be much smaller, secondary contributions to  $\delta\mu^{ex}$  from changes to the micelle shape and aggregation number that affect the entropy of surfactant tails and possibly changes to the hydrophobic hydration of methyl groups near the surfactant headgroup that we have not included in this model. Integrating Eqn. 7.11 [and since  $\Delta\mu^{ex} = RT\ln(CMC/CMC_0)$ ], we get:

$$\ln\left(\frac{CMC}{CMC_0}\right) = \frac{zF(\psi - \psi_0)}{RT} \quad (7.12)$$

where  $CMC_0$  is the CMC with zero-added salt and where  $\psi$  and  $\psi_0$  are the electric potential at the micelle water interface in the presence of and with no added salt respectively. The electric potential at the micelle water interface,  $\psi$  (or  $\psi_0$ ) can be calculated by solving the non-linear Grahame Equation [162]

$$\frac{\sigma^2}{2\epsilon\epsilon_0k_bT} = \sum_i c_i \exp [(-z_i e\psi/k_bT) - 1] \quad (7.13)$$

where  $\sigma$  is the charge density and the summation runs over all ions (this form of the Graham equation is valid for a flat interface; so using it here is an approximation). For a spherical micelle, the charge density can be estimated as:

$$\sigma \approx \frac{N_{agg}ze(1-\alpha)}{4\pi r_m^2} \quad (7.14)$$

where  $N_{agg}$  is the aggregation number of the micelle, and  $r$  is the radius of the micelle. For a micelle formed by SDS surfactants at room temperature,  $z = -1$ ,  $e = 1.609 \times 10^{-19}\text{C}$ , and  $\alpha \approx 0.25$  is the degree of counterion condensation within the Stern layer [163], and  $N_{agg} \approx 60$ , this yields  $\sigma \approx 0.09$  and  $0.063 \text{ C/m}^2$  for  $r = 2.5$  and  $3.0 \text{ nm}$  respectively. Healy et al.[161], report that  $\psi \approx -130$  to  $-140 \text{ mV}$  for pure SLS micelles with no added electrolyte. To be consistent with this measurement, Fig. 7.1 suggests  $\sigma \approx 0.05 - 0.06 \text{ C/m}^2$ . Fig. 7.1 also shows that the exact choice of  $\sigma$  doesn't matter much for how salt affects the CMC ratio at low salt levels or if the charge density is sufficiently high ( $\sigma > 0.06 \text{ C/m}^2$ ). Finally Fig. 7.1 also shows that the predicted CMC reduces as a function of added salt for anionic micelles, with a slope of  $\approx 0.75$  on the log-log plot, which is close to the experimental results (a slope of  $\approx 0.8$ ) from Naskar et al. [164].

### 7.2.3.2 Effect of Salt on Activity Coefficients in the Micelle

We propose that the change in the excess (electro) chemical potential of a surfactant in the mixed micelle due to added salt can similarly be modeled as:

$$\ln(\gamma_i) = \ln(\gamma_{i,0}) + (\psi - \psi_0(\{x_{i,0}\}, c_{salt} = 0))z_i e/kT \quad (7.15)$$

where  $\ln(\gamma_{i,0})$  is the no-added salt activity coefficient and  $\psi_0$  is the salt free electric potential and is again calculated via the Grahame Equation. The charge density of the mixed micelle is given by:

$$\sigma = \frac{N_{agg}e(1-\alpha)}{4\pi r^2} \sum x_i z_i \quad (7.16)$$

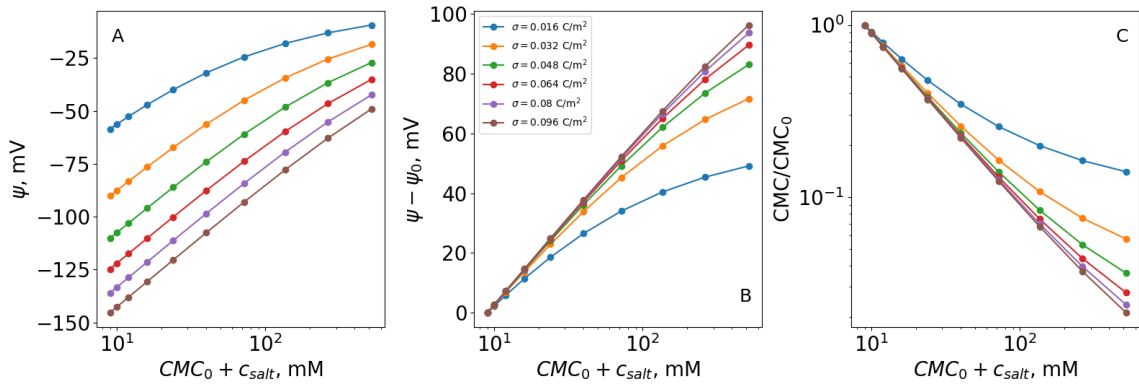


Figure 7.1: (A) Effect of salt on the electric potential,  $\psi$  (from Eqn. 7.13), (B) the change in the electric potential compared to the no-added salt case and (C) the effect on the CMC (from Eqn. 7.12) for anionic micelles of different charge densities. The CMC with no added salt,  $CMC_0 = 8$  mM in this example calculation.

However, in the absence of knowing  $N_{agg}$ ,  $r$  and  $\alpha$  for arbitrary blends of anionic, titrable and zwitterionic surfactants as a function of pH, we propose to scale the charge density by that of a fully anionic micelle. Thus:

$$\sigma \approx \sigma^* \sum x_i z_i \quad (7.17)$$

with  $\sigma^* = 0.064$  C/m<sup>2</sup>. An alternative form to make the model more chemistry specific could be something like:

$$\sigma \sim \frac{\sum (x_i z_i)}{\sum (x_i A_i)} \quad (7.18)$$

where  $A_i$  is the headgroup size, in combination with a heuristic for  $A_i$  (e.g.,  $A_i = A_0 (MW/MW_0)^{2/3}$ , where  $MW$  is the molecular mass of the headgroup and  $A_0$  an  $MW_0$  are the values for a reference headgroup). For now, we will use Eqn. 7.17. We also note that  $x_i$  is a function of the micelle water electric potential,  $\psi$  and hence is a function of  $c_{salt}$ .

For micelles that contain a high fraction of zwitterionics or titrable anionic surfactants near their pKa,  $\sum (x_i z_i)$  can be small, ranging from -0.3 to -0.5 leading to  $|\sigma| < 0.03$ .

Since commercial formulations can contain between 1-3 wt% NaCl (170-500 mM), these compositions are in the regime where  $\Delta\psi = \psi - \psi_0$  deviates substantially from the limiting case of very high charge density shown in Fig. 7.1B.

#### 7.2.4 Final Algorithm

Combining everything above, we have the following numerical workflow to calculate the thermodynamic state (mole fractions, activities etc) for any composition, pH and salt concentration as:

1. Solve the set of coupled equations for the mole fractions of the titrable species as outlined in Sec. 1.1 and 1.2 for the no-added salt case ( $\{x_{i,0}\}$ ). Set  $\sigma_0 = \sigma^* \sum(x_{i,0}z_i)$  (Eqn. 7.17) and calculate  $\psi_0$  by solving Eqn. 7.13 with  $c_{salt} = 0$ .
2. Solve the following set of coupled equations for any added salt concentration ( $c_{salt}$ ):

$$\ln [\gamma_{i,mic} (\{x\}, c_{salt})] = \ln [\gamma_{i,mic} (\{x\}, c_{salt} = 0)] + \Delta\psi(\sigma, c'_{\pm}) \frac{z_i F}{RT} \quad (7.19)$$

$$\sigma = \sigma^* \sum (x_i [c'_{salt}] z_i) \quad (7.20)$$

$$c'_+ = c_{salt} + \sum_j \text{Na}_{i,surf} \quad (7.21)$$

$$c'_- \approx c_{salt} + \sum_j \text{CMC}_{0,S_j^-} \quad (7.22)$$

where  $\Delta\psi = \psi - \psi_0$  and  $\psi(\sigma, c'_{\pm})$  is again calculated *via* Eqn. 7.13. The expression for  $c'_+$  includes the sodium counterions that come with the surfactant. The expression for  $c'_-$  is an approximation because the CMC also changes with added salt. But, it's accurate at low salt levels, and at high salt levels, the first term on the RHS dominates the second. Finally, we also have the Henderson-Hasselbalch closure equation for the ratio of the activities of the protonated and deprotonated surfactants.

$$\frac{a_{S_j^-,mic}}{a_{HS_j,mic}} = \frac{x_{S_j^-,mic}\gamma_{S_j^-,mic}}{x_{HS_j,mic}\gamma_{HS_j,mic}} = \left( \frac{CMC_{HS_j}}{CMC_{S_j^-}(c_{salt})} \right) 10^{pH-pK_a} \quad (7.23)$$

## 7.2.5 Example Calculations with the Model

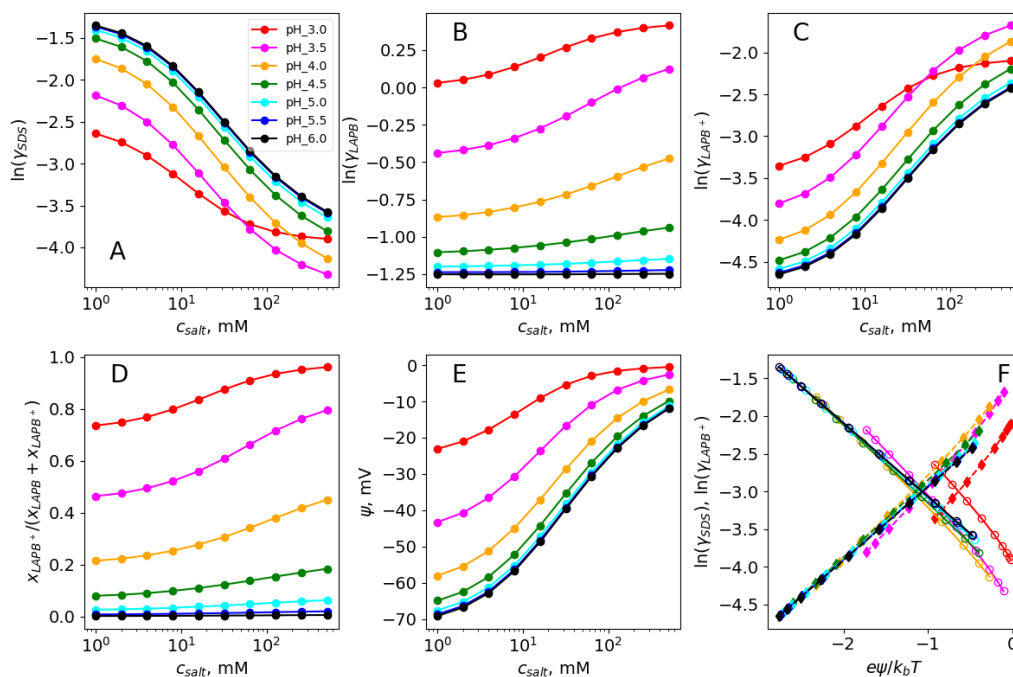


Figure 7.2: Thermodynamic properties of a 50/50 (equimolar) SDS/LAPB micelle as a function of pH and salt. The top three panels shows the excess chemical potentials,  $\ln(\gamma_i)$  of the three surfactants. Note that the Y-axis scales are not the same for different panels. Panel D shows the fraction of LAPB that is protonated and panel E shows the micelle-water electric potential. Panel F shows how  $\ln(\gamma_i)$  of the two charged species, SDS (open circles) and  $LAPB^+$  (filled diamonds) vary with  $e\psi/k_bT$ .

Before using the thermodynamic model to interpret experimental viscosity measurements, we first present calculations for an equimolar and a 80/20 SDS/LAPB mixture as

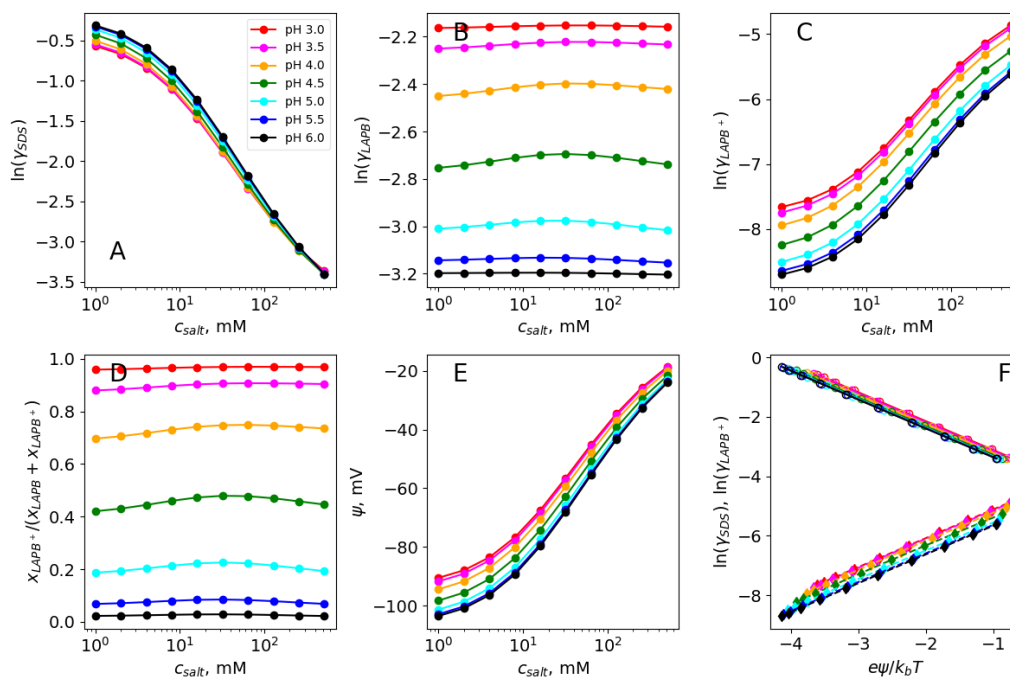


Figure 7.3: Same as Fig. 7.2 but for an 80/20 SDS/LAPB mixture.

a function of pH and salt. In all of the analysis, we take  $\text{CMC}_{SDS} = 8$  mM,  $\text{CMC}_{LAPB} = 2.0$  mM,  $\text{CMC}_{LAPB,+} = 1.9$  mM as mentioned in Table 1.  $\sigma^* = 0.064$  C/m<sup>2</sup>.  $\beta$  parameters was set at  $\beta_{LAPB/LAPB^+} = -2.5$ ,  $\beta_{SDS/LAPB} = -5.0$ , and  $\beta_{SDS/LAPB^+} = -11.6$ . (The choice of these  $\beta$  parameters is explained after we discuss results from the NMR experiments). For an equimolar mixture we observe several interesting features in Fig. 7.2:

- $\ln(\gamma_{SDS})$  decreases with increasing  $\ln(c_{salt})$ , and also reduces with decreasing pH.  $\ln(\gamma_{LAPB^+})$  shows the opposite trends - increasing with added salt and reducing with increasing pH.
- The behavior of both  $\ln(\gamma_{SDS})$  and  $\ln(\gamma_{LAPB^+})$  can be understood by examining how the micelle/water potential,  $\psi$  changes with pH and salt (panel E). As expected, increasing salt screens electrostatic interactions and reduces the magnitude of  $\psi$ .

Similarly, as the pH is reduced and some of the zwitterionic LAPB becomes protonated and cationic, the net charge on the micelle becomes less negative, which again reduces the magnitude of  $\psi$ . The change in the excess chemical potential of the charged species is dominated by this electrostatic effects:  $\Delta \ln(\gamma) \approx ze\Delta\psi/k_bT$ , and since  $z = -1$  for SDS and  $+1$  for the protonated LAPB, and hence they respond in opposite directions to changes in pH and salt concentrations. Panel F where  $\ln(\gamma)$  is plotted against  $\psi$  makes this clear.

- Zwitterionic LAPB:  $\ln(\gamma_{LAPB})$  of the neutral species is independent of the salt concentration at high pH and increases slightly with increasing salt at low pH. It also increases with increasing pH, as the concentration of the protonated LAPB increases. However, in general the magnitude of the charges are small compared to that for the charged surfactants (Panels A, B and C are not on the same scale).
- Finally, the data at pH 3.0 appears to show qualitatively different trends at high salt concentrations which can be rationalized as follows: at such a low pH, as Panel D shows, almost all the LAPB is protonated at high salt concentrations. Since we have an equimolar SDS/LAPB mixture, the micelle is thus net charge neutral at high salt concentrations (Panel E shows  $\psi \approx 0$  at pH 3 and  $c_{salt} > 10^2$  mM). Consequently, as Panels A and C show,  $\mu^{ex}$  of SDS and protonated LAPB no longer change with additional salt.

In contrast, Fig. 7.3 shows that when the total mole fraction of LAPB in the micelle is lower (0.2)  $\ln(\gamma_{SDS})$  and  $\psi$  both show a much smaller pH dependence. However, because the micelle contains more anionic surfactant,  $\ln(\gamma_{LAPB^+})$  is much more negative. Finally, comparison of Panel F of Figs. 7.2 and 7.3 show the same qualitative behavior (or slope) of  $\ln(\gamma)(e\psi/k_bT)$ , but the curves are shifted.

## 7.3 Materials and Methods

### 7.3.1 Materials

We used reagent grade SDS from Sigma Aldrich. The usual industrial/commercial grade CAPB comes with a significant amount of sodium chloride as it is a byproduct of the surfactant making process (5-6 wt% salt in the 30 wt% surfactant solution). It also has a broad alkyl tail length distribution ( $C_{12} \approx 50\%$ ). We therefore used a low salt version of the zwitterionic surfactant, Lauramidopropyl betaine(LAPB) from Solvay (Commercial name: Mackam DAB ULS IS), where the excess salt is removed by dialysis, and the surfactant has a much narrower tail length distribution ( $> 95\% C_{12}$ ). This surfactant is supplied as a 30 wt% solution and contains less than 0.5 wt% NaCl.

### 7.3.2 Sample Preparation

Surfactant solutions containing a total of 12 wt % surfactant were prepared with different SDS/LAPB weight ratios (9:3, 8:4, 6:6, 3:9). The corresponding molar concentrations and mole fractions are given in Table 7.2. Stock solutions of each SDS/LAPB system were prepared by first combining 20 wt% SDS and LAPB stock solutions and diluting them with deionized water to the desired surfactant concentration in each system. Citric acid or hydrochloric acid was used to lower the pH. All solutions were equilibrated for 24 hours at room temperature before any viscosity measurements were conducted.

### 7.3.3 Viscosity Measurements

The shear viscosity were measured for these formulations in pH range of 4.5-6.0 and added salt of up to 2 wt% using a TA Discovery HR-3 rheometer. An additional set of experiments were performed with no added salt exploring the low pH range (up to pH  $\sim 2.0$ ). The viscosities were measured at 26°C over a range of 0.1 to 100 s<sup>-1</sup> using a cone

and plate geometry ( $2^\circ$  cone angle, 40 mm diameter). The viscosity of worm-like micellar solutions usually shows a plateau region at low shear rates ( $\approx < 1 s^{-1}$ ) and a power-law shear thinning behavior at higher shear rates, and eventually plateauing again at very high shear rates. The zero shear viscosity was therefore obtained by fitting a Carreau model that captures these features to the experimental data using the TRIOS software package from TA Instruments.

### 7.3.4 NMR Measurements

Starting surfactant solutions as described in Materials section were 30 wt% in  $H_2O$  for LAPB and reagent grade SDS powder. Diluted surfactant solutions were then made with  $D_2O$  and 1mM sodium 2,2-dimethyl-2-silapentane-5-sulfone (DSS) as internal reference standard. The resulting solution was therefore a surfactant solution in a  $H_2O/D_2O$  mixture. A series of solutions for each surfactant (surfactant mixture) were prepared in increments of 1 pH value by adjusting solution pH with either sodium deuterioxide or deuterium chloride solutions. Solution samples were then transferred to 5-mm NMR tubes filled to a 5-cm sample height. The  $^1H$  NMR experiments were performed at  $25^\circ C$  and recorded at 600 MHz on a Bruker Avance III spectrometer equipment with 5 mm Broadband Prodigy Probe. A  $\pi/2$  pulse length of  $12 \mu s$  was used for all  $^1H$  NMR experiments, using standard water suppression (noesypr1d) with presaturation frequency of 4.7 ppm, 40s delay 8 scans and 2.7s acquisition time. NMR data was processed using MestReNova software (Mestrelab Research, S.L., Santiago de Compostela, Spain). All spectra were then referenced to DSS at 0 ppm. The ppm value was then recorded for peaks of interest at various pH values for all solutions analyzed.

## 7.4 Experimental Results

### 7.4.1 Viscosity Measurements

#### 7.4.1.1 Effect of Added Salt

Fig. 7.4 shows the results of the first set of experiments where viscosities of each formulation in pH range 4.5-6.0 and added salt of up to 2 wt% were measured. Several interesting observations can be made: (i) The sensitivity of viscosity to added salt is very strongly composition dependent - the viscosity increases moderately with salt in SDS rich formulation (9 wt% SDS/3 wt% LAPB) but increases more rapidly with increasing levels of LAPB up to 50% LAPB. (ii) The salt sensitivity is maximal for the 6 wt% SDS/6 wt% LAPB mixture, with the viscosity increasing by 5 orders of magnitude with just 0.5 wt% added salt. (iii) The salt sensitivity reduces with even higher levels of betaine (3 wt% SDS/9 wt% LAPB), although these formulations have a much higher viscosity with no added salt. The viscosity shows a fairly weak pH dependence in this range. Beyond betaine weight fractions of 80%, there is a sudden drop in the viscosity with no salt thickening (data not shown as the viscosities are too low to be measured reliably).

The effect of the fraction of LAPB on the viscosity of SDS/LAPB mixtures is very similar to that reported by Christov et. al. [165] - they also observed a very marked reduction in the sphere-to-rod concentration as the fraction of betaine increases from zero to about 50%, with a broad plateau there and increasing again for highly betaine rich mixtures. The viscosity, and micelle size (from light scattering) also showed a corresponding non-monotonic behavior - increasing rapidly with increasing levels of betaine and reducing at very high levels of betaine. Thus, a novel feature of this dataset is the systematic study of the effect of salt, in combination with using a low-salt LAPB to start with (Christov et. al. [165] had used a more typical high salt version of CAPB in their study).

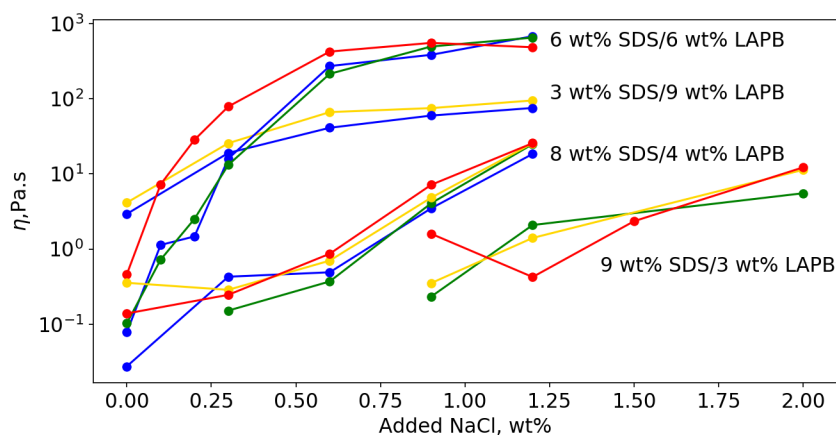


Figure 7.4: Viscosity of 12 wt% SDS/LAPB mixtures as a function of added salt in the pH range of 4.5-6.0. The corresponding molar compositions and mole fractions of the surfactants are in Table. 7.2. Different colors represent data at different pH: pH 4.5 (red), pH 5.0 (yellow), pH 5.5 (green), pH 6.0 (blue).

#### 7.4.1.2 Effect of pH

Fig. 7.5 shows the results of the next set of experiments at lower pH (combined with the zero-added salt data from Fig. 7.4). The key highlights are the following: (i) If the pH is low enough, the viscosity of SDS/LAPB solutions also becomes pH dependent. (ii) This pH dependence of the viscosity becomes apparent at higher pHs with increasing level of betaine. Formulations containing >50% betaine show a marked pH response for pH < 5 which is close to the typical pH of commercial products (5.0-7.0).

#### 7.4.2 NMR Titration of LAPB

The most likely explanation for the pH dependence of viscosity for SDS/LAPB solutions is the changing protonation state of the surfactants. The sulfate group in SDS is a very strong electrolyte with a pKa  $\sim$ 3 and is unlikely to become partially protonated

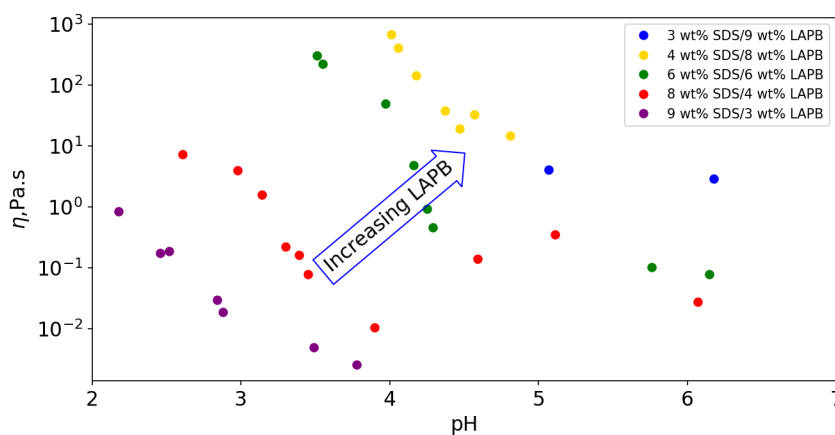


Figure 7.5: Viscosity of 12 wt% SDS/LAPB mixtures as a function pH with no added salt.

as the pH is lowered. The  $pK_a$  for the carboxylic group of LAPB has been reported to be 1.9 by Weers et al.[166]. However, we may reasonably expect that the  $pK_a$  will be shifted higher in a mixed micelle containing anionic surfactants [167] - this is simply due to favorable electrostatics between the protonated (and hence cationic) betaine with the negatively charged SDS surfactants. To confirm this, we used proton NMR to probe the protonation state of pure LAPB and 2:1 SDS/LAPB mixtures at two different total surfactant concentrations. Peaks susceptible to changes in electron density due to protonation-deprotonation as a result have an observable shift in position. In particular, one can track peak positions as a function of pH by referencing NMR spectra to internal reference standard such as an unreactive silane molecule (DSS, Disodium silanol) [168]. In Fig. 7.6, the position of two regions associated with the molecular structure of LAPB are tracked over a wide pH range. The resulting titration curves as well as the comparison with the thermodynamic model are shown in Fig. 7.7.

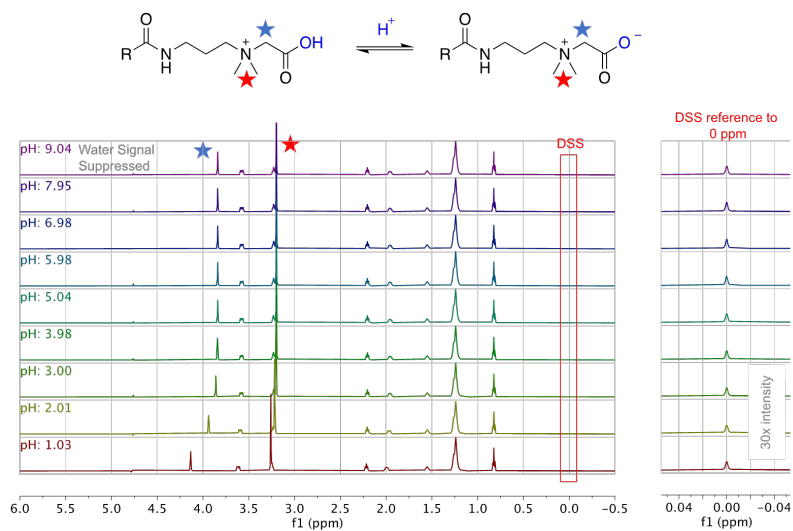


Figure 7.6: Top: Structure of LAPB (R = C<sub>12</sub>) and the chemical moieties tracked by <sup>1</sup>H NMR: the methyls (red star) attached to the nitrogen in the region of 3.2 - 3.3 ppm and with the the methylene singlet (blue star) in the region of 3.8-4.2 ppm show pH dependence on their peak position when referenced versus a standard (Due to the low level of DSS used, expansion of -0.04-0.04 ppm with 30x intensity to show DSS referenced to 0 ppm for all spectra.). Bottom: NMR spectra as a function of pH: the dynamic range of the measurement is larger in the 3.8-4.2 ppm range, and was used to track the protonation state of LAPB (data shown for 2 wt % LAPB).

| Symbol   | Meaning  |
|--|--|
| $\{CMC_i\}, \quad i = 1, N$  | Input: Set of pure component CMCs of each type of surfactant   |
| $\{X_i\}, \quad i = 1, N_{surf}$   | Input: Set of mole fractions of each surfactant type in the micelle (e.g., SDS and total LAPB). At concentrations far above the CMC, this is assumed to be representative of the composition of the system.                    |
| $\{x_i\}, \quad i = 1, N$  | Set of mole fractions of each surfactant type (including protonated/deprotonated forms) in the micelle. If none of the surfactants are titrable, $N = N_{surf}$ and $x_i = X_i$ . In this report, $N_{surf} = 2$ and $N = 3$ . |
| $\{\mu_i^{ex} = RT \ln(\gamma_i)\}, \quad i = 1, N$                              | Set of excess chemical potentials or activity coefficients of the surfactants in the micelle.  |
| $\{g_i^{ex} = RT x_i \ln(\gamma_i)\}, \quad i = 1, N$                            | Set of excess free energies of each surfactant in the micelle  |
| $\{a_i = x_i \gamma_i\}, \quad i = 1, N$   | Set of thermodynamic activities of each surfactant in the micelle (and monomer) phases   |
| $\{c_{i,mon} = CMC_i a_i\}, \quad i = 1, N$                                      | Set of free monomer concentration of each surfactant.  |
| $CMC_{mix} = \left[ \sum \left( \frac{x_i}{\gamma_i CMC_i} \right) \right]^{-1}$ | Mixed CMC of the surfactant mixture  |
| $q = \sum_i^N x_i z_i$   | Micelle charge/Aggregation number ( $z_i$ is the charge of each surfactant type)   |
| $\phi$   | Electric potential at the micelle/water interface  |

Table 7.1: Different outputs from the thermodynamic micelle model. The top two rows are inputs to the model, along with the pH and salt levels. Additional physical property inputs are pure component  $pK_a$  for each titrable surfactant (e.g., 1.9 for LAPB), and the micelle charge densities of the each pure component micelle. In the calculations below, that is set to  $0.064z$  C/m<sup>2</sup> where  $z$  is the charge of the surfactant.  $CMC_{SDS} = 8$  mM,  $CMC_{LAPB} = 2.0$

| SDS, wt% | LAPB, wt% | SDS mM | LAPB   | Total  | $x_{SDS}$ | $x_{LAPB}$ |
|----------|-----------|--------|--------|--------|-----------|------------|
| 3        | 9         | 104.17 | 263.16 | 367.32 | 0.28      | 0.72       |
| 4        | 8         | 138.89 | 233.92 | 372.81 | 0.37      | 0.63       |
| 6        | 6         | 208.33 | 175.44 | 383.77 | 0.54      | 0.46       |
| 8        | 4         | 277.78 | 116.96 | 394.74 | 0.70      | 0.30       |
| 9        | 3         | 312.50 | 87.72  | 400.22 | 0.78      | 0.22       |

Table 7.2: Surfactant compositions tested in wt%, mM and mole fraction (in the micellar phase). The molecular weight of SDS is 288 g/mol and that of LAPB is 342.5 g/mol.

### 7.4.2.1 pKa of Pure LAPB

We find that in line with the measurements of Weers et al. [166], pure LAPB has a  $pK_a \sim 1.9$ . The reason that the  $pK_a$  for the carboxylic group is so low is due to the quaternary nitrogen that is just 2 carbons away (see structure in Fig. 7.6). Indeed, Weers et al. show that as the carbon spacing between the quaternary nitrogen and carboxylic group increases, the  $pK_a$  approaches a more typical value of  $\approx 4.5$ , comparable to the  $pK_a$  of small carboxylic acids, e.g. acetic acid.

### 7.4.2.2 pKa of LAPB in LAPB/SDS Micelles

The left panel of Fig. 7.7 shows that as anticipated, there is a large  $pK_a$  shift (of 1.8 units) in the presence of anionic SDS. Thus, a reasonable fraction of the betaine could be cationic at pH ranges of 4.0-5.0 and cationic synergy can increase the viscosity of those solutions if the betaine fraction is high enough. It is well known that mixtures of cationic and anionic surfactants can show very high viscosities.

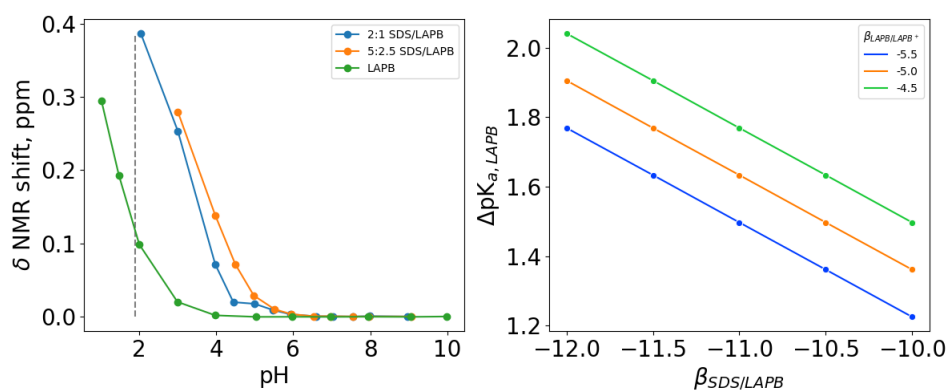


Figure 7.7: Left: pH dependent NMR shift of LAPB in pure LAPB and in a 2:1 SDS/LAPB solutions. Right: Theoretical predictions of the  $pK_a$  shift using the pH-dependent regular solution theory model of mixed micelles for different choices of  $\beta_{SDS/LAPB}$  and  $\beta_{SDS/LAPB^+}$ , and with  $\beta_{LAPB/LAPB^+} = -2.5$ .

To qualitatively test this, the viscosity of SDS/LAPB solutions (with no added salt) as a function of the betaine NMR shift is plotted in Fig. 7.8. It is clear that for a given SDS/LAPB ratio, the fraction of the betaine that is protonated as measured by the NMR shift is an excellent predictor of the solution viscosity. Further, the datasets for each SDS/LAPB ratio are roughly parallel to each other suggesting some universality in this. This also suggests that carefully tracking the pH dependent protonation state of other zwitterionic and titratable surfactants in micelles of different composition *via* NMR will be important for developing a deeper understanding of micellar rheology when one of the surfactants is titratable.

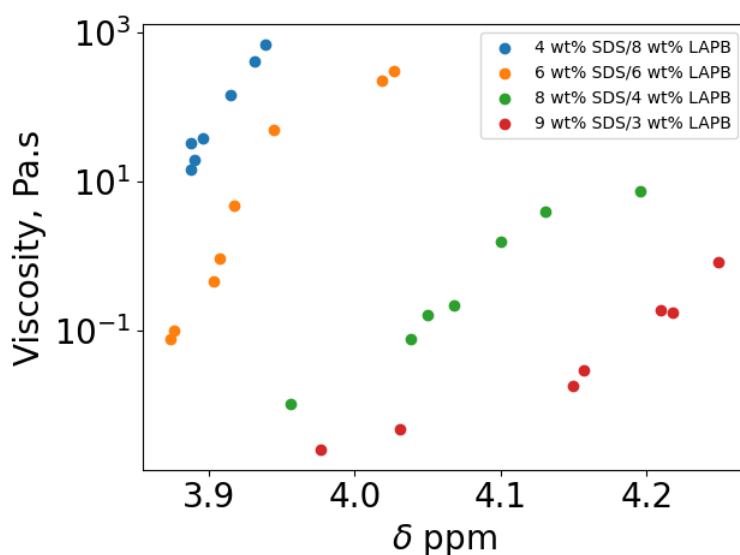


Figure 7.8: Correlation between measured NMR shift of LAPB with solution viscosity. The NMR shift was not measured for each composition; instead the pH dependent NMR shift of the betaine in the 2:1 SDS/LAPB mixture (Fig. 7.7), interpolated at the pH for which the viscosity was measured is used for this comparison.

### 7.4.2.3 Parameterizing $\beta$ parameters with the pKa shift

The SDS/LAPB system is characterized by 3 beta parameters:  $\beta_{SDS/LAPB}$ ,  $\beta_{LAPB/LAPB^+}$ , and  $\beta_{SDS/LAPB^+}$ .

- In principle, we can characterize  $\beta_{LAPB/LAPB^+}$  from the titration curve of pure LAPB at a concentration above the CMC. However, pure LAPB has a pKa  $\sim 1.9$ , and one will need to go to a very low pH  $\approx 0$  to observe the full titration curve which is hard to do. A negative value of  $\beta_{LAPB/LAPB^+}$  will manifest as broadening of the titration curve (above the CMC) relative to that predicted by the Henderson-Hasselbalch form, as shown by Rathman and Christian [153] for the zwitterionic surfactant, Dodecyl Amino Oxide (DDAO, which has a pK<sub>a</sub>  $\approx 5.0$ ). Rathman and Christian report  $\beta$  parameters of -2.8 to -3.0 between the the protonated and deprotonated form of amine oxide. Hence, we set  $\beta_{LAPB/LAPB^+} \approx -2.5$ .
- The synergy between SDS and betaine in the context of CMC depression has been studied by Iwasaki et. al. [169] and also modeled using MT approaches by Shiloach and Blankschein[170]. Shiloach and Blankschein also compared the  $\beta$  parameter obtained by the MT approach with the  $\beta$  parameter from mixed CMC measurements and found that  $\beta_{SDS/LAPB} \approx -5.0$  described the data well. Note that they considered LAPB to be purely zwitterionic - and hence needed only a single  $\beta$  parameter to describe the SDS/LAPB system. This approach is valid at pH  $> 5.5 - 6.0$  when the fraction of protonated, cationic LAPB is negligible. We thus also set  $\beta_{SDS/LAPB} = -5.0$  in our model.
- We expect  $\beta_{SDS/LAPB^+}$  to be significantly negative due to highly favorable electrostatic effects between a cationic and an anionic surfactant ( $\approx -10$  to  $-15$  [171]). Since the thermodynamic model predicts the pH titration state of LAPB,  $\beta_{SDS/LAPB^+}$  can be optimized by comparing model predictions to the NMR data. We set  $\beta_{LAPB/LAPB^+} =$

-2.5 and calculated the  $\text{pK}_a$  shift of LAPB in 2:1 SDS/LAPB mixtures as a function of  $\beta_{\text{SDS/LAPB}^+}$  for  $\beta_{\text{SDS/LAPB}} = -4.5, -5.0$  and  $-5.5$  (right panel of Fig. 7.7). For  $\beta_{\text{SDS/LAPB}} = -5.0$ ,  $\beta_{\text{SDS/LAPB}^+} \approx -11.6$  yields a  $\text{pK}_a$  shift consistent with the experimental measurements shown in the left panel of Fig. 7.7.

Finally, although  $\beta$  parameters are usually quantified via mixed CMC or surface tension measurements, using NMR, as we demonstrate here, is an attractive alternative, especially for commercial surfactants which will have small levels of surface-active impurities and a tail length distribution which makes CMC and surface tension measurements challenging. Another advantage of NMR titration over conventional titration is that the protonation states of different surfactants can be tracked individually if needed (e.g., a combination of LAPB with amino-acid based surfactants like Lauroyl sarcosinate [172, 173] or Lauroyl alaninate that have a titrable carboxylic group).

## 7.5 A Semi-empirical Model of Viscosity

In this section, we demonstrate the use of the thermodynamic model to model and interpret the zero shear viscosity measurements. Fig. 7.9 shows scatter plots of key explanatory variables - the surfactant excess chemical potentials,  $\mu_i^{\text{ex}}/k_bT = \ln(\gamma_i)$ , and the micelle water electric potential against each other and against the measured zero shear viscosity. The corresponding correlation coefficients are reported in Table. 7.3. We observe several interesting trends:

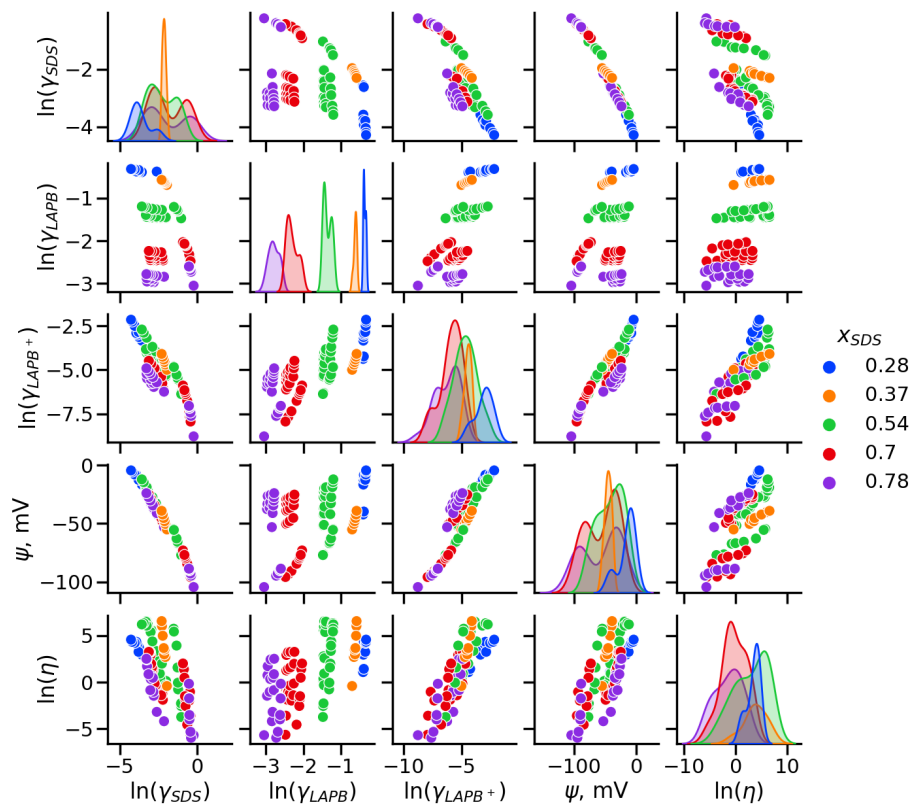


Figure 7.9: A pair-plot of the correlations between calculated  $\ln(\gamma_i)$ , the micelle water electric potential,  $\psi$  and the measured zero shear viscosity for different SDS/LAPB ratios and variable salt levels. The correlation coefficients are also reported in Tab. 7.3. The points are colored by the mole fraction of SDS.

This micelle/water potential,  $\psi$  is very negative ( $\sim -100$  mV) for pure SDS micelles and reduces with added salt or with adding LAPB. It also seems to be a much better predictor of the viscosity than the  $\log(\text{CMC})$  or the micelle charge ( $q = \sum x_i z_i$ ) (see Fig. S1 and Fig. S2 in the Supporting Information); in fact, although statistically,  $\ln(\gamma_{LAPB,+})$  is the single best predictor of viscosity, from a mechanistic perspective, it could be argued that  $\psi$  is the most interpretable explanatory variable (especially since both  $\ln(\gamma_{SDS})$  and  $\ln(\gamma_{LAPB,+})$  are highly correlated with  $\psi$ , Table 7.3). Reducing the magnitude of  $\psi$  makes it easier

|                        | $\ln(\gamma_{SDS})$ | $\ln(\gamma_{LAPB})$ | $\ln(\gamma_{LAPB^+})$ | $\psi$ , mV | $\ln(\eta)$ |
|------------------------|---------------------|----------------------|------------------------|-------------|-------------|
| $\ln(\gamma_{SDS})$    | 1.0                 | -0.32                | -0.83                  | -0.99       | -0.67       |
| $\ln(\gamma_{LAPB})$   | -0.32               | 1.0                  | 0.74                   | 0.37        | 0.6         |
| $\ln(\gamma_{LAPB^+})$ | -0.83               | 0.74                 | 1.0                    | 0.88        | 0.85        |
| $\psi$ , mV            | -0.99               | 0.37                 | 0.88                   | 1.0         | 0.74        |
| $\ln(\eta)$            | -0.67               | 0.6                  | 0.85                   | 0.74        | 1.0         |
| $x_{SDS}$              | 0.4                 | -0.98                | -0.75                  | -0.44       | -0.58       |

Table 7.3: Correlation coefficients between modeled surfactant excess chemical potential, micelle water electric potentials and experimentally measured viscosities.

free energetically to incorporate the majority ionic species into the micelle and increase the viscosity. In the SDS/LAPB system, that majority ionic species is SDS. If we were in a system that contained a cationic surfactant (e.g., CTAB) along with a titrable surfactant that switched between anionic and neutral with pH, we anticipate that the relationship would be reversed, and an increase in viscosity being correlated with an increase in the chemical potential of the anionic species.

That the electric potential determines the energetics of micelle elongation in primarily ionic surfactant systems and therefore of viscosity is also intuitive to understand. Importantly, the correlation with the surface potential appears to hold even though the viscosity is changing by many orders of magnitude - i.e., as we traverse micelle structures spanning from just elongated to partially entangled to highly entangled. Finally, although challenging, it is nevertheless possible to measure it experimentally (by e.g., zeta potentials, potentiometric probes) for some systems and hence, it is a testable hypothesis. It also offers a clear target for more sophisticated, chemistry specific theoretical models to model a range of surfactants and their blends.

### 7.5.1 A Bayesian Model for $\ln(\eta)$ based on Surfactant Chemical Activity Coefficients

$\gamma_i$

We next explored whether a simple linear model of the form:

$$\ln(\eta) = C + \sum w_i \ln(\gamma_i) \quad (7.24)$$

where the summation extends over the three types of surfactants, SDS, LAPB and LAPB<sup>+</sup> can be used to model the experimental viscosity measurements. However, instead of using a conventional regression, we use Bayesian regression (with the python package, pyMC3 [174]) to estimate the coefficients,  $w_i$  and  $C$  with the following weakly informative priors:

$$C \sim \text{Normal}(\mu = 0, \sigma = 10.0) \quad (7.25)$$

$$w_i \sim \text{Normal}(\mu = 0, \sigma = 5.0) \quad (7.26)$$

and the following likelihood function:

$$s \sim \text{HalfNormal}(\sigma = 2.0) \quad (7.27)$$

$$\text{Probability}(\ln(\eta)|C, \{w_i\}) \sim \text{Normal}(\mu = C + \sum w_i \ln(\gamma_i), \sigma = s) \quad (7.28)$$

Fig. 7.10 shows the results of the Bayesian regression and shows that simple semi-empirical models can be useful to model these complex systems. A Bayesian approach provides several advantages over a conventional regression:

- **Uncertainty quantification:** The posterior provides the joint distribution of the parameters,  $\theta = \{C, \{w_i\}\}$  instead of point estimates and hence the uncertainty in the predictions can be quantified.
- **Philosophically,** the Bayesian approach treats ‘data’ and ‘parameters’ on an equal footing, recognizing that they both have uncertainties and that there is no single ‘true’ parameter value[175]. In a model such as Eqn. 7.24,  $C$  and  $w_i$  are not

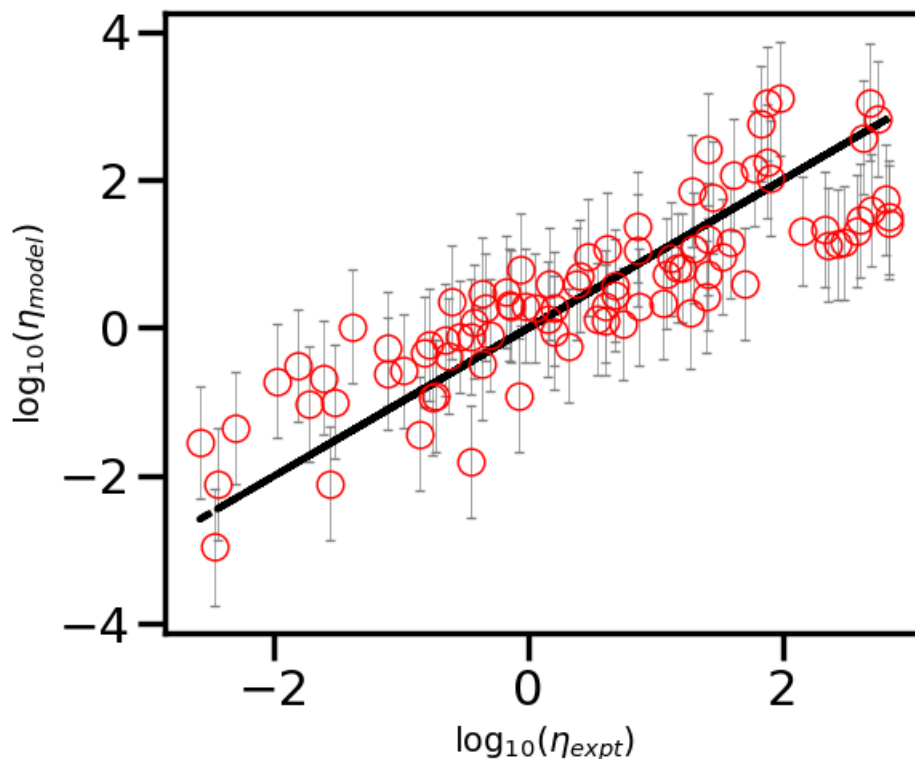


Figure 7.10: Results of the Bayesian regression: the solid line is the  $X = Y$  line; error bars show the 1 standard deviation prediction interval. The  $R^2$  for the model mean is 0.746. The marginal parameter estimates and the standard deviations are:  $C = 1.13 \pm 0.18$ ,  $w_{SDS} = 1.48 \pm 0.54$ ,  $w_{LAPB} = -1.18 \pm 0.45$  and  $w_{LAPB^+} = 4.85 \pm 0.76$ , and  $s = 1.69 \pm 0.13$ .

the only parameters that have to be estimated;  $\ln(\gamma_i)$  are complex functions of the thermodynamic parameters (e.g.,  $\beta$  parameters, CMCs etc), and there is uncertainty in our estimates of these parameters as well (indeed, even the RST model augmented with electrostatics at the Poisson-Boltzmann level is only an approximation). In effect, as a practical approach for computational efficiency, we have fixed those parameters to our best estimates and are assigning all the uncertainty to our estimates of  $C$  and  $w_i$ .

- Extension to other surfactant systems: Bayesian models lend themselves very naturally to a ‘hierarchical’ or ‘multi-level’ model structure[175]. For small changes to the surfactant architecture, it might be a reasonable approximation to leave the thermodynamic parameters fixed if they are not known (or update them as best as possible with heuristics and available experimental measurements) and model the experimental viscosities with slightly different  $\{C, \{w_i\}\}$  such that most of the essential physics is still captured. And in a hierarchical model, the parameters  $C^k, \{w_i^k\}$  for different surfactant blends can be drawn from corresponding parent distributions (or hyperparameters,  $C^{global}, \{w_i^{global}\}$ ) so that a diverse data set with multiple surfactant blends can be analyzed robustly.

Finally, we comment on the difference between the approach presented here and that presented recently in e.g., Danov et. al., [149–152] or in Christov et. al., [165] where micelle elongation (which can perhaps eventually be related to viscosity) was modeled by calculating the difference in the excess chemical potentials of the surfactants in the cylindrical vs the spherical endcaps - *i.e.*,  $\Delta\mu = \mu_{cyl} - \mu_{sph}$ . This difference for an individual surfactant is small,  $\sim 0.05 - 0.1k_bT$ , but the net driving force becomes large as this is multiplied by the aggregation number,  $N \sim 10^2 - 10^3$ . Nevertheless, since  $\Delta\mu$  is small, the fidelity needed from a model will be challenging to achieve while simultaneously being able to handle a wide-range of surfactant headgroup chemistries with accuracy - definitely beyond the capabilities of a relatively simple RST-based approach. However, this simpler framework is a scalable and practical approach in an industrial setting where predictions have to be made on a diverse set of industrial grade raw materials with impurities, and somewhat broad chain length distributions.

## 7.6 Conclusion

In this paper, we have presented new experimental data of the viscosity of SDS/LAPB mixtures over a range of salt and pH levels. The results are consistent with the strong ‘synergy’ seen for SDS/LAPB mixtures reported in earlier studies [165, 170, 176] and results on the effect of salt and especially pH are new. That LAPB, with a pKa of 1.9 can become partially cationic in a mixed micelle with anionic surfactants and the importance of this for micelle elongation and viscosity is a novel finding, as is our use of NMR experiments to obtain  $\beta$  parameters between surfactants.

Our approach of using a relatively simple thermodynamic model to calculate the pH, composition and salt concentration dependent activity coefficients of surfactants in a Bayesian framework to semi-empirically model the viscosity of these micellar solutions is a good example of combining theoretical rigor with pragmatism for industrial or commercial applications. It provides a facile and extensible way to combine molecular information with experimentally measured macroscopic properties. Beyond viscosity, we anticipate that such a Bayesian semi-empirical approach can be used for modeling other macroscopic properties - e.g., relating model-derived surfactant activity coefficients (and other quantities such as the micelle/water electric potential and micelle charge densities) to experimental measurements of lather volume or longevity under different conditions, phase behavior with polyelectrolytes, and other applications. The thermodynamic framework can be made more rigorous if needed while striking a balance between complexity and practicality.

**Acknowledgement.** Xueying Ko’s internship at P&G was funded by NSF Grant CBET 1705817. The authors thank Peter Koenig, Ahmad Ghobadi, Jessa Meyers, Geoffrey Reynolds and Howard Hutton at P&G for many useful discussions during Xueying’s internship. The authors also thank Brandon Illie and Geoffrey Reynolds for their valiant efforts to measure zeta potentials of SDS/LAPB micelles to complement the NMR measurements but which turned out to be more challenging than initially anticipated. The

authors thank Dr. Ron Larson (U. Michigan) and Dr. Vivek Sharma (U. Illinois, Chicago) for useful discussions and comments on early versions of this manuscript. The authors appreciate Dr. Sumit Sharma's (Ohio University) comments on the final versions of the manuscript.

## 8 CONCLUSIONS AND FUTURE WORK

The main focus of this research has been to understand the adsorption and self-assembly of surfactant molecules at metallic surfaces using molecular simulations. For this purpose, we have developed a coarse-grained model of surfactant molecules and have studied various aspects of the adsorption phenomena.

### 8.1 Summary of Results

Our results not only provide a molecular-level understanding of the adsorption of corrosion inhibitor molecules on metal surfaces, but they also test currently held assumptions on the nature of adsorption of these molecules and help in providing new insights. Our work also proposes a new theoretical model to predict adsorption morphologies of these molecules on surfaces. The main findings of this work are listed below.

- It is found that the hydrophobic interactions between alkyl tails of corrosion inhibitor molecules plays an important role in the adsorption and self-assembly of adsorbed molecules in ordered configurations. When hydrophobic interactions between the alkyl tails are turned weak, the molecules do not form highly packed SAM on the surface even when the polar group has strong affinity for the surface. The other end of the spectrum is when the hydrophobic interactions are made quite strong. In such a scenario, the molecules aggregate in the bulk and thus the adsorption amount on the surface reduces.
- It is shown that the geometry of the inhibitor molecules is an important determinant of the adsorption morphology. The molecules with a larger polar head beads are found to adsorb as cylindrical and spherical micelles.

- The strength of the affinity of metal surfaces for polar beads alter the kinetics of adsorption. However, eventually a SAM is achieved if the affinity is above a critical value because after the initial adsorption, the latter adsorption regimes are dictated by lateral tail-tail interactions.
- We find that oil molecules of some optimum length are able to co-adsorb with the corrosion inhibitor films. Interestingly, it is observed that co-adsorbing oil molecules result in transforming a cylindrical morphology of the corrosion inhibitor film into a planar morphology, thereby making the inhibitor film more densely packed and more hydrophobic. Experiments have shown that presence of oil molecules, either in the aqueous phase, or via exposing the film to oil results in better corrosion inhibition efficiency.
- We have developed a theoretical model that is able to predict the adsorption morphology of corrosion inhibitor molecules on the metal surface. Our simulation results show that our model is quantitatively accurate in the predictions and does not require any fitting parameter. This model will be quite useful in predicting the adsorption morphology without the need to perform simulations.
- We show that inhibitor molecules are able to achieve full adsorption coverage even when the surface is heterogeneous with large areas that are not attractive to the molecules. Full coverage is achieved because of the lateral hydrophobic interactions between the molecules.

## **8.2 Future work**

The research presented in this dissertation has revealed many interesting insights into the adsorption of surfactant molecules on polar surfaces, but at the same time, many aspects

have not been addressed. I would like to propose a few potential areas of extension of the work discussed in this research.

- **Study of co-adsorption of inhibitor molecules with different tail lengths.** In our simulations, the inhibitor molecules used in each system are of same size. However, in field conditions, inhibitors in the commercially available inhibitor package are presumably of varying tail lengths. Therefore, it will be interesting to study if mixtures of inhibitors improves the adsorption behavior of these molecules via some synergistic effect.
- **Estimating the free energy of different adsorbed configurations.** In our studies, we have not compared the free energies between various adsorbed configurations. By generating a free energy landscape as a function of some appropriate order parameter, say the number of adsorbed molecules, will provide insights into meta-stable as well as globally stable configurations.
- **Exploring adsorption in different surface chemistry and including roughness.** In our simulation system, the metal surface was modeled as a smooth surface with a Lennard Jones interactions. The current system can be extended where the metal surface is modeled as a lattice of atoms, and furthermore, one can consider the effects of nanometer-sized roughness on the adsorption behavior.

## REFERENCES

- [1] A. Edwards, C. Osborne, S. Webster, D. Klenerman, M. Joseph, P. Ostovar, and M. Doyle, "Mechanistic studies of the corrosion inhibitor oleic imidazoline," *Corrosion Science*, vol. 36, no. 2, pp. 315–325, 1994.
- [2] C. J. Murphy, T. K. Sau, A. M. Gole, C. J. Orendorff, J. Gao, L. Gou, S. E. Hunyadi, and T. Li, "Anisotropic metal nanoparticles: synthesis, assembly, and optical applications," *The Journal of Physical Chemistry B*, vol. 109, no. 29, pp. 13857–13870, 2005.
- [3] J. Li and A. E. Kaifer, "Surfactant monolayers on electrode surfaces: self-assembly of a viologen derivative having a cholesteryl hydrophobic residue," *Langmuir*, vol. 9, no. 2, pp. 591–596, 1993.
- [4] S. T. Marshall, M. O'Brien, B. Oetter, A. Corpuz, R. M. Richards, D. K. Schwartz, and J. W. Medlin, "Controlled selectivity for palladium catalysts using self-assembled monolayers," *Nature materials*, vol. 9, no. 10, pp. 853–858, 2010.
- [5] A. McMahon, "The mechanism of action of an oleic imidazoline based corrosion inhibitor for oilfield use," *Colloids and surfaces*, vol. 59, pp. 187–208, 1991.
- [6] G. Koch, J. Varney, N. Thompson, O. Moghissi, M. Gould, and J. Payer, "International measures of prevention, application, and economics of corrosion technologies study," *NACE International*, p. 216, 2016.
- [7] G. H. Koch, M. P. Brongers, N. G. Thompson, Y. P. Virmani, and J. H. Payer, "Corrosion cost and preventive strategies in the united states," tech. rep., 2002.
- [8] C. G. Dariva and A. F. Galio, "Corrosion inhibitors—principles, mechanisms and applications," *Developments in corrosion protection*, vol. 16, pp. 365–378, 2014.
- [9] M. Fontana, *Corrosion Engineering*. McGraw-Hill series in materials science and engineering, Tata McGraw-Hill, 2005.
- [10] E. McCafferty, *Introduction to corrosion science*. Springer Science & Business Media, 2010.
- [11] S. Papavinasam, "67: Evaluation and selection of corrosion inhibitors," 1999.
- [12] M. Finšgar, "2-mercaptobenzimidazole as a copper corrosion inhibitor: Part i. long-term immersion, 3d-profilometry, and electrochemistry," *Corrosion Science*, vol. 72, pp. 82–89, 2013.
- [13] M. Finšgar, J. Kovač, and I. Milošev, "Surface analysis of 1-hydroxybenzotriazole and benzotriazole adsorbed on cu by x-ray photoelectron spectroscopy," *Journal of the Electrochemical Society*, vol. 157, no. 2, p. C52, 2009.

- [14] J. D. Olivo, B. Brown, D. Young, and S. Nešić, "Effect of corrosion inhibitor alkyl tail length on the electrochemical process governing CO<sub>2</sub> corrosion of mild steel," *Corrosion*, vol. 75, no. 2, pp. 137–139, 2019.
- [15] M. Migahed and A. Al-Sabagh, "Beneficial role of surfactants as corrosion inhibitors in petroleum industry: a review article," *Chemical Engineering Communications*, vol. 196, no. 9, pp. 1054–1075, 2009.
- [16] J. Martin and F. Valone, "The existence of imidazoline corrosion inhibitors," *Corrosion*, vol. 41, no. 5, pp. 281–287, 1985.
- [17] Y. Duda, R. Govea-Rueda, M. Galicia, H. I. Beltran, and L. S. Zamudio-Rivera, "Corrosion inhibitors: design, performance, and computer simulations," *The Journal of Physical Chemistry B*, vol. 109, no. 47, pp. 22674–22684, 2005.
- [18] Y.-J. Tan, S. Bailey, and B. Kinsella, "An investigation of the formation and destruction of corrosion inhibitor films using electrochemical impedance spectroscopy (eis)," *Corrosion science*, vol. 38, no. 9, pp. 1545–1561, 1996.
- [19] X. Liu, S. Chen, F. Tian, H. Ma, L. Shen, and H. Zhai, "Studies of protection of iron corrosion by rosin imidazoline self-assembled monolayers," *Surface and Interface Analysis: An International Journal devoted to the development and application of techniques for the analysis of surfaces, interfaces and thin films*, vol. 39, no. 4, pp. 317–323, 2007.
- [20] Y. Xiong, B. Brown, B. Kinsella, S. Nešić, and A. Pailleret, "Atomic force microscopy study of the adsorption of surfactant corrosion inhibitor films," *Corrosion*, vol. 70, no. 3, pp. 247–260, 2014.
- [21] S. Ramachandran, B.-L. Tsai, M. Blanco, H. Chen, Y. Tang, and W. A. Goddard, "Self-assembled monolayer mechanism for corrosion inhibition of iron by imidazolines," *Langmuir*, vol. 12, no. 26, pp. 6419–6428, 1996.
- [22] C. D. Taylor, A. Chandra, J. Vera, and N. Sridhar, "A multiphysics perspective on mechanistic models for chemical corrosion inhibitor performance," *Journal of the Electrochemical Society*, vol. 162, no. 7, p. C369, 2015.
- [23] Y. Zhu, M. L. Free, R. Woollam, and W. Durnie, "A review of surfactants as corrosion inhibitors and associated modeling," *Progress in Materials Science*, vol. 90, pp. 159–223, 2017.
- [24] S. Nešić, "Key issues related to modelling of internal corrosion of oil and gas pipelines—a review," *Corrosion science*, vol. 49, no. 12, pp. 4308–4338, 2007.
- [25] R. T. Loto, "Surface coverage and corrosion inhibition effect of *rosmarinus officinalis* and zinc oxide on the electrochemical performance of low carbon steel in dilute acid solutions," *Results in physics*, vol. 8, pp. 172–179, 2018.

- [26] V. S. Sastri, *Green corrosion inhibitors: theory and practice*, vol. 10. John Wiley & Sons, 2012.
- [27] W. Wang and J. C. Kwak, "Adsorption at the alumina–water interface from mixed surfactant solutions," *Colloids and Surfaces A: Physicochemical and Engineering Aspects*, vol. 156, no. 1-3, pp. 95–110, 1999.
- [28] D. Bitting and J. H. Harwell, "Effects of counterions on surfactant surface aggregates at the alumina/aqueous solution interface," *Langmuir*, vol. 3, no. 4, pp. 500–511, 1987.
- [29] T. F. Tadros, "The interaction of cetyltrimethylammonium bromide and sodium dodecylbenzene sulfonate with polyvinyl alcohol. adsorption of the polymer—surfactant complexes on silica," *Journal of Colloid and Interface Science*, vol. 46, no. 3, pp. 528–540, 1974.
- [30] R. Zhang and P. Somasundaran, "Advances in adsorption of surfactants and their mixtures at solid/solution interfaces," *Advances in colloid and interface science*, vol. 123, pp. 213–229, 2006.
- [31] P. Somasundaran and J. T. Kunjappu, "In-situ investigation of adsorbed surfactants and polymers on solids in solution," *Colloids and Surfaces*, vol. 37, pp. 245–268, 1989.
- [32] W. J. Lokar, L. K. Koopal, F. A. Leermakers, and W. A. Ducker, "Confinement-induced phase behavior and adsorption regulation of ionic surfactants in the aqueous film between charged solids," *The Journal of Physical Chemistry B*, vol. 108, no. 39, pp. 15033–15042, 2004.
- [33] P. Cummins, J. Penfold, and E. Staples, "A study of the structure of mixed cationic/nonionic micelles by small-angle neutron scattering spectrometry," *Langmuir*, vol. 8, no. 1, pp. 31–35, 1992.
- [34] X. Liu, A. Dedinaite, T. Nylander, A. P. Dabkowska, M. Skoda, R. Makuska, and P. M. Claesson, "Association of anionic surfactant and physisorbed branched brush layers probed by neutron and optical reflectometry," *Journal of colloid and interface science*, vol. 440, pp. 245–252, 2015.
- [35] R. Atkin, V. S. Craig, E. J. Wanless, and S. Biggs, "Mechanism of cationic surfactant adsorption at the solid–aqueous interface," *Advances in colloid and interface science*, vol. 103, no. 3, pp. 219–304, 2003.
- [36] J. W. Haefner, *Modeling Biological Systems:: Principles and Applications*. Springer Science & Business Media, 2005.

- [37] M. Aghaaminiha, A. M. Farnoud, and S. Sharma, "Quantitative relationship between cholesterol distribution and ordering of lipids in asymmetric lipid bilayers," *Soft Matter*, vol. 17, no. 10, pp. 2742–2752, 2021.
- [38] I. G. Mikellides, K. Tassis, and H. W. Yorke, "2d magnetohydrodynamics simulations of induced plasma dynamics in the near-core region of a galaxy cluster," *Monthly Notices of the Royal Astronomical Society*, vol. 410, no. 4, pp. 2602–2616, 2011.
- [39] I. R. Craig and D. E. Manolopoulos, "Chemical reaction rates from ring polymer molecular dynamics," *The Journal of chemical physics*, vol. 122, no. 8, p. 084106, 2005.
- [40] D. Chandler, "Interfaces and the driving force of hydrophobic assembly," *Nature*, vol. 437, no. 7059, pp. 640–647, 2005.
- [41] M. P. Allen and D. J. Tildesley, *Computer simulation of liquids*. Oxford university press, 2017.
- [42] D. Frenkel and B. Smit, *Understanding molecular simulation: from algorithms to applications*, vol. 1. Elsevier, 2001.
- [43] D. Sholl and J. A. Steckel, *Density functional theory: a practical introduction*. John Wiley & Sons, 2011.
- [44] R. Wu, M. Deng, B. Kong, and X. Yang, "Coarse-grained molecular dynamics simulation of ammonium surfactant self-assemblies: micelles and vesicles," *The Journal of Physical Chemistry B*, vol. 113, no. 45, pp. 15010–15016, 2009.
- [45] G. A. Somorjai and Y. Li, *Introduction to surface chemistry and catalysis*. John Wiley & Sons, 2010.
- [46] in *Modern aspects of electrochemistry, Number 38*, Springer, 2005.
- [47] M. Finšgar and J. Jackson, "Application of corrosion inhibitors for steels in acidic media for the oil and gas industry: a review," *Corrosion science*, vol. 86, pp. 17–41, 2014.
- [48] R. R. Naik, S. J. Stringer, G. Agarwal, S. E. Jones, and M. O. Stone, "Biomimetic synthesis and patterning of silver nanoparticles," *Nature materials*, vol. 1, no. 3, pp. 169–172, 2002.
- [49] X. Wang and I.-M. Hsing, "Surfactant stabilized pt and pt alloy electrocatalyst for polymer electrolyte fuel cells," *Electrochimica acta*, vol. 47, no. 18, pp. 2981–2987, 2002.

- [50] J. Zhang and C. M. Li, "Nanoporous metals: fabrication strategies and advanced electrochemical applications in catalysis, sensing and energy systems," *Chemical Society Reviews*, vol. 41, no. 21, pp. 7016–7031, 2012.
- [51] S. Nestic, "Testing of inhibitors for CO<sub>2</sub> corrosion using the electrochemical techniques," S. Nestic, W. Wilhelmsen (Inst. for Energy Technology, Kjeller, Norway), S. Skjerve, and S. M. Hesjevik (Statoil, Trondheim, Norway), pp. 1163–1192, 1995.
- [52] G. Gece, "Drugs: A review of promising novel corrosion inhibitors," *Corrosion Science*, vol. 53, no. 12, pp. 3873–3898, 2011.
- [53] P. B. Raja and M. G. Sethuraman, "Natural products as corrosion inhibitor for metals in corrosive media—a review," *Materials letters*, vol. 62, no. 1, pp. 113–116, 2008.
- [54] G. Gece and S. Bilgiç, "A theoretical study on the inhibition efficiencies of some amino acids as corrosion inhibitors of nickel," *Corrosion Science*, vol. 52, no. 10, pp. 3435–3443, 2010.
- [55] V. Jovancicevic, S. Ramachandran, and P. Prince, "Inhibition of CO<sub>2</sub> corrosion of mild steel by imidazolines and their precursors," tech. rep., NACE International, Houston, TX (United States), 1998.
- [56] S. Manne, J. Cleveland, H. Gaub, G. Stucky, and P. Hansma, "Direct visualization of surfactant hemimicelles by force microscopy of the electrical double layer," *Langmuir*, vol. 10, no. 12, pp. 4409–4413, 1994.
- [57] T. P. Goloub, L. K. Koopal, B. H. Bijsterbosch, and M. P. Sidorova, "Adsorption of cationic surfactants on silica. surface charge effects," *Langmuir*, vol. 12, no. 13, pp. 3188–3194, 1996.
- [58] H. N. Patrick, G. G. Warr, S. Manne, and I. A. Aksay, "Self-assembly structures of nonionic surfactants at graphite/solution interfaces," *Langmuir*, vol. 13, no. 16, pp. 4349–4356, 1997.
- [59] P. Somasundaran and D. Fuerstenau, "Mechanisms of alkyl sulfonate adsorption at the alumina-water interface," *The Journal of Physical Chemistry*, vol. 70, no. 1, pp. 90–96, 1966.
- [60] A. Fan, P. Somasundaran, and N. J. Turro, "Adsorption of alkyltrimethylammonium bromides on negatively charged alumina," *Langmuir*, vol. 13, no. 3, pp. 506–510, 1997.
- [61] H. N. Patrick, G. G. Warr, S. Manne, and I. A. Aksay, "Surface micellization patterns of quaternary ammonium surfactants on mica," *Langmuir*, vol. 15, no. 5, pp. 1685–1692, 1999.

- [62] M. Jaschke, H.-J. Butt, H. Gaub, and S. Manne, "Surfactant aggregates at a metal surface," *Langmuir*, vol. 13, no. 6, pp. 1381–1384, 1997.
- [63] R. Atkin, V. S. Craig, E. J. Wanless, and S. Biggs, "The influence of chain length and electrolyte on the adsorption kinetics of cationic surfactants at the silica–aqueous solution interface," *Journal of colloid and interface science*, vol. 266, no. 2, pp. 236–244, 2003.
- [64] T. P. Goloub and L. K. Koopal, "Adsorption of cationic surfactants on silica. comparison of experiment and theory," *Langmuir*, vol. 13, no. 4, pp. 673–681, 1997.
- [65] M. P. Allen and D. J. Tildesley, *Computer simulation of liquids*. Oxford university press, 1989.
- [66] J. D. Weeks, D. Chandler, and H. C. Andersen, "Role of repulsive forces in determining the equilibrium structure of simple liquids," *The Journal of chemical physics*, vol. 54, no. 12, pp. 5237–5247, 1971.
- [67] C. J. Van Oss, M. K. Chaudhury, and R. J. Good, "Interfacial lifshitz-van der waals and polar interactions in macroscopic systems," *Chemical reviews*, vol. 88, no. 6, pp. 927–941, 1988.
- [68] N. Choudhury and B. M. Pettitt, "On the mechanism of hydrophobic association of nanoscopic solutes," *Journal of the American Chemical Society*, vol. 127, no. 10, pp. 3556–3567, 2005.
- [69] N. Kovačević, I. Milošev, and A. Kokalj, "How relevant is the adsorption bonding of imidazoles and triazoles for their corrosion inhibition of copper?," *Corrosion science*, vol. 124, pp. 25–34, 2017.
- [70] S. Plimpton, "Fast parallel algorithms for short-range molecular dynamics," *Journal of computational physics*, vol. 117, no. 1, pp. 1–19, 1995.
- [71] V. Padmanabhan, S. K. Kumar, and A. Yethiraj, "Phase behavior of semiflexible polymer chains," *The Journal of chemical physics*, vol. 128, no. 12, p. 124908, 2008.
- [72] S. Sharma and P. G. Debenedetti, "Free energy barriers to evaporation of water in hydrophobic confinement," *The Journal of Physical Chemistry B*, vol. 116, no. 44, pp. 13282–13289, 2012.
- [73] M. Ester, H.-P. Kriegel, J. Sander, X. Xu, *et al.*, "A density-based algorithm for discovering clusters in large spatial databases with noise.," in *Kdd*, vol. 96, pp. 226–231, 1996.
- [74] H. Arkin and W. Janke, "Gyration tensor based analysis of the shapes of polymer chains in an attractive spherical cage," *The Journal of chemical physics*, vol. 138, no. 5, p. 054904, 2013.

- [75] S. Abbott, "Surfactant science: principles and practice," *Update*, vol. 1, pp. 2–26, 2016.
- [76] S. Sharma, X. Ko, Y. Kurapati, H. Singh, and S. Nešić, "Adsorption behavior of organic corrosion inhibitors on metal surfaces—some new insights from molecular simulations," *Corrosion*, vol. 75, no. 1, pp. 90–105, 2019.
- [77] S. Manne, T. Schäffer, Q. Huo, P. Hansma, D. Morse, G. Stucky, and I. A. Aksay, "Gemini surfactants at solid- liquid interfaces: control of interfacial aggregate geometry," *Langmuir*, vol. 13, no. 24, pp. 6382–6387, 1997.
- [78] S. Manne and H. E. Gaub, "Molecular organization of surfactants at solid-liquid interfaces," *Science*, vol. 270, no. 5241, pp. 1480–1482, 1995.
- [79] X. Qi, T. Balankura, Y. Zhou, and K. A. Fichthorn, "How structure-directing agents control nanocrystal shape: polyvinylpyrrolidone-mediated growth of ag nanocubes," *Nano letters*, vol. 15, no. 11, pp. 7711–7717, 2015.
- [80] C. A. Schoenbaum, D. K. Schwartz, and J. W. Medlin, "Controlling the surface environment of heterogeneous catalysts using self-assembled monolayers," *Accounts of chemical research*, vol. 47, no. 4, pp. 1438–1445, 2014.
- [81] R. A. Johnson and R. Nagarajan, "Modeling self-assembly of surfactants at solid/liquid interfaces. i. hydrophobic surfaces," *Colloids and Surfaces A: Physicochemical and Engineering Aspects*, vol. 167, no. 1-2, pp. 31–46, 2000.
- [82] R. Johnson and R. Nagarajan, "Modeling self-assembly of surfactants at solid–liquid interfaces. ii. hydrophilic surfaces," *Colloids and Surfaces A: Physicochemical and Engineering Aspects*, vol. 167, no. 1-2, pp. 21–30, 2000.
- [83] S.-L. Xu, C. Wang, Q.-D. Zeng, P. Wu, Z.-G. Wang, H.-K. Yan, and C.-L. Bai, "Self-assembly of cationic surfactants on a graphite surface studied by stm," *Langmuir*, vol. 18, no. 3, pp. 657–660, 2002.
- [84] W. A. Hayes and D. K. Schwartz, "Two-stage growth of octadecyltrimethylammonium bromide monolayers at mica from aqueous solution below the krafft point," *Langmuir*, vol. 14, no. 20, pp. 5913–5917, 1998.
- [85] K. Shimazu, I. Yagi, Y. Sato, and K. Uosaki, "In situ and dynamic monitoring of the self-assembling and redox processes of a ferrocenylundecanethiol monolayer by electrochemical quartz crystal microbalance," *Langmuir*, vol. 8, no. 5, pp. 1385–1387, 1992.
- [86] J. Woodward, I. Doudevski, H. Sikes, and D. Schwartz, "Kinetics of self-assembled monolayer growth explored via submonolayer coverage of incomplete films," *The Journal of Physical Chemistry B*, vol. 101, no. 38, pp. 7535–7541, 1997.

- [87] I. Doudevski, W. A. Hayes, and D. K. Schwartz, "Submonolayer island nucleation and growth kinetics during self-assembled monolayer formation," *Physical review letters*, vol. 81, no. 22, p. 4927, 1998.
- [88] G. Poirier and E. Pylant, "The self-assembly mechanism of alkanethiols on au (111)," *Science*, vol. 272, no. 5265, pp. 1145–1148, 1996.
- [89] S. Xu, S. J. Cruchon-Dupeyrat, J. C. Garno, G.-Y. Liu, G. Kane Jennings, T.-H. Yong, and P. E. Laibinis, "In situ studies of thiol self-assembly on gold from solution using atomic force microscopy," *The Journal of chemical physics*, vol. 108, no. 12, pp. 5002–5012, 1998.
- [90] X. Ko and S. Sharma, "Adsorption and self-assembly of surfactants on metal–water interfaces," *The Journal of Physical Chemistry B*, vol. 121, no. 45, pp. 10364–10370, 2017.
- [91] Y. Kurapati and S. Sharma, "Adsorption free energies of imidazolium-type surfactants in infinite dilution and in micellar state on gold surface," *The Journal of Physical Chemistry B*, vol. 122, no. 22, pp. 5933–5939, 2018.
- [92] L. T. Popoola, A. S. Grema, G. K. Latinwo, B. Gutti, and A. S. Balogun, "Corrosion problems during oil and gas production and its mitigation," *International Journal of Industrial Chemistry*, vol. 4, no. 1, pp. 1–15, 2013.
- [93] M. Knag, J. Sjöblom, G. Øye, and E. Gulbrandsen, "A quartz crystal microbalance study of the adsorption of quaternary ammonium derivatives on iron and cementite," *Colloids and Surfaces A: Physicochemical and Engineering Aspects*, vol. 250, no. 1-3, pp. 269–278, 2004.
- [94] H. Singh and S. Sharma, "Disintegration of surfactant micelles at metal–water interfaces promotes their strong adsorption," *The Journal of Physical Chemistry B*, vol. 124, no. 11, pp. 2262–2267, 2020.
- [95] S. Sharma, H. Singh, and X. Ko, "A quantitatively accurate theory to predict adsorbed configurations of linear surfactants on polar surfaces," *The Journal of Physical Chemistry B*, vol. 123, no. 34, pp. 7464–7470, 2019.
- [96] N. Choudhury and B. M. Pettitt, "The dewetting transition and the hydrophobic effect," *Journal of the American Chemical Society*, vol. 129, no. 15, pp. 4847–4852, 2007.
- [97] A. P. Willard and D. Chandler, "Instantaneous liquid interfaces," *The Journal of Physical Chemistry B*, vol. 114, no. 5, pp. 1954–1958, 2010.
- [98] M. Kermani and A. Morshed, "Carbon dioxide corrosion in oil and gas production—a compendium," *Corrosion*, vol. 59, no. 8, pp. 659–683, 2003.

- [99] M. Shalaby and M. Osman, "Synergistic inhibition of anionic and nonionic surfactants on corrosion of mild steel in acidic solution," *Anti-Corrosion Methods and Materials*, 2001.
- [100] G. Zhang, C. Chen, M. Lu, C. Chai, and Y. Wu, "Evaluation of inhibition efficiency of an imidazoline derivative in co<sub>2</sub>-containing aqueous solution," *Materials Chemistry and Physics*, vol. 105, no. 2-3, pp. 331–340, 2007.
- [101] I. Jevremović, M. Singer, S. Nešić, and V. Mišković-Stanković, "Inhibition properties of self-assembled corrosion inhibitor talloil diethylenetriamine imidazoline for mild steel corrosion in chloride solution saturated with carbon dioxide," *Corrosion Science*, vol. 77, pp. 265–272, 2013.
- [102] I. Jevremović, M. Singer, S. Nešić, and V. Mišković-Stanković, "Electrochemistry of carbon dioxide corrosion mitigation using tall oil diethylenetriamine imidazoline as corrosion inhibitor for mild steel," *Materials and Corrosion*, vol. 67, no. 7, pp. 756–768, 2016.
- [103] C. Li, S. Richter, and S. Nestic, "How do inhibitors mitigate corrosion in oil-water two phase flow beyond lowering the corrosion rate?," in *CORROSION 2013*, OnePetro, 2013.
- [104] Y. Chen and W. Jepson, "Eis measurement for corrosion monitoring under multiphase flow conditions," *Electrochimica acta*, vol. 44, no. 24, pp. 4453–4464, 1999.
- [105] M. Foss, E. Gulbrandsen, and J. Sjoblom, "Alteration of wettability of corroding carbon steel surface by carbon dioxide corrosion inhibitors—effect on carbon dioxide corrosion rate and contact angle," *Corrosion*, vol. 64, no. 12, pp. 905–919, 2008.
- [106] M. Foss, E. Gulbrandsen, and J. Sjoblom, "Effect of corrosion inhibitors and oil on carbon dioxide corrosion and wetting of carbon steel with ferrous carbonate deposits," *Corrosion*, vol. 65, no. 1, pp. 3–14, 2009.
- [107] M. Foss, E. Gulbrandsen, and J. Sjoblom, "Oil wetting and carbon dioxide corrosion inhibition of carbon steel with ferric corrosion products deposits," *Corrosion*, vol. 66, no. 2, pp. 025005–025005, 2010.
- [108] X. Ko and S. Sharma, "A quantitatively accurate theory to predict adsorbed configurations of asymmetric surfactant molecules on polar surfaces," *The Journal of Physical Chemistry B*, vol. 124, no. 26, pp. 5517–5524, 2020.
- [109] W. Lorenz and F. Mansfeld, "Determination of corrosion rates by electrochemical dc and ac methods," *Corrosion Science*, vol. 21, no. 9-10, pp. 647–672, 1981.

- [110] J. Newman and K. E. Thomas-Alyea, *Electrochemical systems*. John Wiley & Sons, 2012.
- [111] B. Hou, Q. Zhang, Y. Li, G. Zhu, and G. Zhang, “Influence of corrosion products on the inhibition effect of pyrimidine derivative for the corrosion of carbon steel under supercritical co<sub>2</sub> conditions,” *Corrosion Science*, vol. 166, p. 108442, 2020.
- [112] L. D. Paolinelli, T. Pérez, and S. N. Simison, “The effect of pre-corrosion and steel microstructure on inhibitor performance in co<sub>2</sub> corrosion,” *Corrosion Science*, vol. 50, no. 9, pp. 2456–2464, 2008.
- [113] E. Gulbrandsen, A. Stangeland, T. Burchardt, S. Nesic, S. Morten Hesjevik, S. Skjfrve, and B. Sundfer, “Effect of precorrosion on the performance of inhibitors for co<sub>2</sub> corrosion of carbon steel,” in *CORROSION 98*, OnePetro, 1998.
- [114] A. Shamsa, R. Barker, Y. Hua, E. Barmatov, T. L. Hughes, and A. Neville, “Performance evaluation of an imidazoline corrosion inhibitor in a co<sub>2</sub>-saturated environment with emphasis on localised corrosion,” *Corrosion Science*, vol. 176, p. 108916, 2020.
- [115] H.-h. Zhang, X. Pang, M. Zhou, C. Liu, L. Wei, and K. Gao, “The behavior of pre-corrosion effect on the performance of imidazoline-based inhibitor in 3 wt.% nacl solution saturated with co<sub>2</sub>,” *Applied Surface Science*, vol. 356, pp. 63–72, 2015.
- [116] E. Senatore, W. Taleb, J. Owen, Y. Hua, J. P. Gomes, R. Barker, and A. Neville, “Evaluation of high shear inhibitor performance in co<sub>2</sub>-containing flow-induced corrosion and erosion-corrosion environments in the presence and absence of iron carbonate films,” *Wear*, vol. 404, pp. 143–152, 2018.
- [117] P. Cornwell, “A review of shampoo surfactant technology: consumer benefits, raw materials and recent developments,” *International journal of cosmetic science*, vol. 40, no. 1, pp. 16–30, 2018.
- [118] R. Bordes and K. Holmberg, “Amino acid-based surfactants—do they deserve more attention?,” *Advances in Colloid and Interface Science*, vol. 222, pp. 79–91, 2015.
- [119] A. V. Svensson, L. Huang, E. S. Johnson, T. Nylander, and L. Piculell, “Surface deposition and phase behavior of oppositely charged polyion/surfactant ion complexes. 1. cationic guar versus cationic hydroxyethylcellulose in mixtures with anionic surfactants,” *ACS applied materials & interfaces*, vol. 1, no. 11, pp. 2431–2442, 2009.
- [120] A. V. Svensson, E. S. Johnson, T. Nylander, and L. Piculell, “Surface deposition and phase behavior of oppositely charged polyion- surfactant ion complexes. 2. a means to deliver silicone oil to hydrophilic surfaces,” *ACS Applied Materials & Interfaces*, vol. 2, no. 1, pp. 143–156, 2010.

- [121] M. Clauzel, E. S. Johnson, T. Nylander, R. K. Panandiker, M. R. Sivik, and L. Piculell, "Surface deposition and phase behavior of oppositely charged polyion-surfactant ion complexes. delivery of silicone oil emulsions to hydrophobic and hydrophilic surfaces," *ACS applied materials & interfaces*, vol. 3, no. 7, pp. 2451–2462, 2011.
- [122] D. Li, M. S. Kelkar, and N. J. Wagner, "Phase behavior and molecular thermodynamics of coacervation in oppositely charged polyelectrolyte/surfactant systems: a cationic polymer jr 400 and anionic surfactant sds mixture," *Langmuir*, vol. 28, no. 28, pp. 10348–10362, 2012.
- [123] X. Tang, W. Zou, P. H. Koenig, S. D. McConaughy, M. R. Weaver, D. M. Eike, M. J. Schmidt, and R. G. Larson, "Multiscale modeling of the effects of salt and perfume raw materials on the rheological properties of commercial threadlike micellar solutions," *The Journal of Physical Chemistry B*, vol. 121, no. 11, pp. 2468–2485, 2017.
- [124] J.-H. Mu, G.-Z. Li, X.-L. Jia, H.-X. Wang, and G.-Y. Zhang, "Rheological properties and microstructures of anionic micellar solutions in the presence of different inorganic salts," *The Journal of Physical Chemistry B*, vol. 106, no. 44, pp. 11685–11693, 2002.
- [125] M. Pleines, W. Kunz, T. Zemb, D. Benczédi, and W. Fieber, "Molecular factors governing the viscosity peak of giant micelles in the presence of salt and fragrances," *Journal of colloid and interface science*, vol. 537, pp. 682–693, 2019.
- [126] S. Candau, A. Khatory, F. Lequeux, and F. Kern, "Rheological behaviour of wormlike micelles: effect of salt content," *Le Journal de Physique IV*, vol. 3, no. C1, pp. C1–197, 1993.
- [127] A. Parker and W. Fieber, "Viscoelasticity of anionic wormlike micelles: effects of ionic strength and small hydrophobic molecules," *Soft Matter*, vol. 9, no. 4, pp. 1203–1213, 2013.
- [128] M. Cates and S. Candau, "Statics and dynamics of worm-like surfactant micelles," *Journal of Physics: Condensed Matter*, vol. 2, no. 33, p. 6869, 1990.
- [129] A. Khatory, F. Lequeux, F. Kern, and S. Candau, "Linear and nonlinear viscoelasticity of semidilute solutions of wormlike micelles at high salt content," *Langmuir*, vol. 9, no. 6, pp. 1456–1464, 1993.
- [130] W. Zou and R. G. Larson, "A mesoscopic simulation method for predicting the rheology of semi-dilute wormlike micellar solutions," *Journal of Rheology*, vol. 58, no. 3, pp. 681–721, 2014.

- [131] W. Zou, G. Tan, H. Jiang, K. Vogtt, M. Weaver, P. Koenig, G. Beaucage, and R. G. Larson, "From well-entangled to partially-entangled wormlike micelles," *Soft matter*, vol. 15, no. 4, pp. 642–655, 2019.
- [132] G. B. Goh, D. M. Eike, B. P. Murch, and C. L. Brooks III, "Accurate modeling of ionic surfactants at high concentration," *The Journal of Physical Chemistry B*, vol. 119, no. 20, pp. 6217–6224, 2015.
- [133] X. Tang, P. H. Koenig, and R. G. Larson, "Molecular dynamics simulations of sodium dodecyl sulfate micelles in water: The effect of the force field," *The Journal of Physical Chemistry B*, vol. 118, no. 14, pp. 3864–3880, 2014.
- [134] D. S. Yakovlev and E. S. Boek, "Molecular dynamics simulations of mixed cationic/anionic wormlike micelles," *Langmuir*, vol. 23, no. 12, pp. 6588–6597, 2007.
- [135] S. Wang and R. G. Larson, "Coarse-grained molecular dynamics simulation of self-assembly and surface adsorption of ionic surfactants using an implicit water model," *Langmuir*, vol. 31, no. 4, pp. 1262–1271, 2015.
- [136] R. L. Anderson, D. J. Bray, A. Del Regno, M. A. Seaton, A. S. Ferrante, and P. B. Warren, "Micelle formation in alkyl sulfate surfactants using dissipative particle dynamics," *Journal of chemical theory and computation*, vol. 14, no. 5, pp. 2633–2643, 2018.
- [137] H. Wang, X. Tang, D. M. Eike, R. G. Larson, and P. H. Koenig, "Scission free energies for wormlike surfactant micelles: development of a simulation protocol, application, and validation for personal care formulations," *Langmuir*, vol. 34, no. 4, pp. 1564–1573, 2018.
- [138] T. Taddese, R. L. Anderson, D. J. Bray, and P. B. Warren, "Recent advances in particle-based simulation of surfactants," *Current Opinion in Colloid & Interface Science*, vol. 48, pp. 137–148, 2020. Formulations and Cosmetics.
- [139] E. Lavagnini, J. L. Cook, P. B. Warren, M. J. Williamson, and C. A. Hunter, "A surface site interaction point method for dissipative particle dynamics parametrization: application to alkyl ethoxylate surfactant self-assembly," *The Journal of Physical Chemistry B*, vol. 124, no. 24, pp. 5047–5055, 2020.
- [140] C. R. Wand, M. Panoukidou, A. Del Regno, R. L. Anderson, and P. Carbone, "The relationship between wormlike micelle scission free energy and micellar composition: The case of sodium lauryl ether sulfate and cocamidopropyl betaine," *Langmuir*, vol. 36, no. 41, pp. 12288–12298, 2020.
- [141] B. O. Conchuir, K. Gardner, K. E. Jordan, D. J. Bray, R. L. Anderson, M. A. Johnston, W. C. Swope, A. Harrison, D. R. Sheehy, and T. J. Peters, "Efficient

- algorithm for the topological characterization of worm-like and branched micelle structures from simulations,” *Journal of Chemical Theory and Computation*, vol. 16, no. 7, pp. 4588–4598, 2020.
- [142] P. Holland and D. Rubingh, “Nonideal multicomponent mixed micelle model,” *The Journal of Physical Chemistry*, vol. 87, no. 11, pp. 1984–1990, 1983.
- [143] P. M. Holland, “Nonideal mixed micellar solutions,” *Advances in Colloid and Interface Science*, vol. 26, pp. 111–129, 1986.
- [144] R. Nagarajan and E. Ruckenstein, “Theory of surfactant self-assembly: a predictive molecular thermodynamic approach,” *Langmuir*, vol. 7, no. 12, pp. 2934–2969, 1991.
- [145] T. A. Camesano and R. Nagarajan, “Micelle formation and cmc of gemini surfactants: a thermodynamic model,” *Colloids and Surfaces A: Physicochemical and Engineering Aspects*, vol. 167, no. 1-2, pp. 165–177, 2000.
- [146] S. Puvvada and D. Blankschtein, “Molecular-thermodynamic approach to predict micellization, phase behavior and phase separation of micellar solutions. i. application to nonionic surfactants,” *The Journal of chemical physics*, vol. 92, no. 6, pp. 3710–3724, 1990.
- [147] V. Srinivasan and D. Blankschtein, “Effect of counterion binding on micellar solution behavior: 1. molecular- thermodynamic theory of micellization of ionic surfactants,” *Langmuir*, vol. 19, no. 23, pp. 9932–9945, 2003.
- [148] V. Srinivasan and D. Blankschtein, “Effect of counterion binding on micellar solution behavior: 2. prediction of micellar solution properties of ionic surfactant-electrolyte systems,” *Langmuir*, vol. 19, no. 23, pp. 9946–9961, 2003.
- [149] K. D. Danov, P. A. Kralchevsky, S. D. Stoyanov, J. L. Cook, and I. P. Stott, “Analytical modeling of micelle growth. 1. chain-conformation free energy of binary mixed spherical, wormlike and lamellar micelles,” *Journal of colloid and interface science*, vol. 547, pp. 245–255, 2019.
- [150] K. D. Danov, P. A. Kralchevsky, S. D. Stoyanov, J. L. Cook, and I. P. Stott, “Analytical modeling of micelle growth. 2. molecular thermodynamics of mixed aggregates and scission energy in wormlike micelles,” *Journal of colloid and interface science*, vol. 551, pp. 227–241, 2019.
- [151] K. D. Danov, P. A. Kralchevsky, S. D. Stoyanov, J. L. Cook, and I. P. Stott, “Analytical modeling of micelle growth. 3. electrostatic free energy of ionic wormlike micelles—effects of activity coefficients and spatially confined electric double layers,” *Journal of Colloid and Interface Science*, vol. 581, pp. 262–275, 2021.

- [152] K. D. Danov, P. A. Kralchevsky, R. D. Stanimirova, S. D. Stoyanov, J. L. Cook, and I. P. Stott, "Analytical modeling of micelle growth. 4. molecular thermodynamics of wormlike micelles from ionic surfactants: Theory vs. experiment," *Journal of Colloid and Interface Science*, vol. 584, pp. 561–581, 2021.
- [153] J. F. Rathman and S. D. Christian, "Determination of surfactant activities in micellar solutions of dimethyldodecylamine oxide," *Langmuir*, vol. 6, no. 2, pp. 391–395, 1990.
- [154] M. Turner and M. Cates, "Linear viscoelasticity of wormlike micelles: a comparison of micellar reaction kinetics," *Journal de Physique II*, vol. 2, no. 3, pp. 503–519, 1992.
- [155] T. Vu, M. R. Weaver, G. B. Kasting, and P. Koenig, "Effect of pH on the structure and dynamics of wormlike micelles in an amino acid-derived surfactant composition," *Langmuir*, vol. 37, no. 14, pp. 4112–4120, 2021.
- [156] E. Aniansson and S. N. Wall, "Kinetics of step-wise micelle association," *The Journal of Physical Chemistry*, vol. 78, no. 10, pp. 1024–1030, 1974.
- [157] G. Aniansson, "The mean lifetime of a micelle," in *Surfactants, Adsorption, Surface Spectroscopy and Disperse Systems*, pp. 2–5, Springer, 1985.
- [158] R. Pool and P. G. Bolhuis, "Sampling the kinetic pathways of a micelle fusion and fission transition," *The Journal of chemical physics*, vol. 126, no. 24, p. 244703, 2007.
- [159] M. Turner and M. Cates, "Linear viscoelasticity of living polymers: A quantitative probe of chemical relaxation times," *Langmuir*, vol. 7, no. 8, pp. 1590–1594, 1991.
- [160] C. Oelschlaeger, G. Waton, and S. Candau, "Rheological behavior of locally cylindrical micelles in relation to their overall morphology," *Langmuir*, vol. 19, no. 25, pp. 10495–10500, 2003.
- [161] T. W. Healy, C. J. Drummond, F. Grieser, and B. S. Murray, "Electrostatic surface potential and critical micelle concentration relationship for ionic micelles," *Langmuir*, vol. 6, no. 2, pp. 506–508, 1990.
- [162] J. N. Israelachvili, "Chapter 14 - electrostatic forces between surfaces in liquids," in *Intermolecular and Surface Forces (Third Edition)* (J. N. Israelachvili, ed.), pp. 291–340, San Diego: Academic Press, third edition ed., 2011.
- [163] S. Shah, N. Jamroz, and Q. Sharif, "Micellization parameters and electrostatic interactions in micellar solution of sodium dodecyl sulfate (sds) at different temperatures," *Colloids and Surfaces A: Physicochemical and Engineering Aspects*, vol. 178, no. 1-3, pp. 199–206, 2001.

- [164] B. Naskar, A. Dey, and S. P. Moulik, "Counter-ion effect on micellization of ionic surfactants: A comprehensive understanding with two representatives, sodium dodecyl sulfate (sds) and dodecyltrimethylammonium bromide (dtab)," *Journal of Surfactants and Detergents*, vol. 16, no. 5, pp. 785–794, 2013.
- [165] N. Christov, N. Denkov, P. Kralchevsky, K. Ananthapadmanabhan, and A. Lips, "Synergistic sphere-to-rod micelle transition in mixed solutions of sodium dodecyl sulfate and cocoamidopropyl betaine," *Langmuir*, vol. 20, no. 3, pp. 565–571, 2004.
- [166] J. G. Weers, J. F. Rathman, F. U. Axe, C. A. Crichlow, L. D. Foland, D. R. Scheuing, R. J. Wiersema, and A. G. Zielske, "Effect of the intramolecular charge separation distance on the solution properties of betaines and sulfobetaines," *Langmuir*, vol. 7, no. 5, pp. 854–867, 1991.
- [167] F. L. Barroso da Silva, D. Bogren, O. Söderman, T. Åkesson, and B. Jönsson, "Titration of fatty acids solubilized in cationic, nonionic, and anionic micelles. theory and experiment," *The Journal of Physical Chemistry B*, vol. 106, no. 13, pp. 3515–3522, 2002.
- [168] C. S. Handloser, M. Chakrabarty, and M. W. Mosher, "Experimental determination of pka values by use of nmr chemical shift," *Journal of Chemical Education*, vol. 50, no. 7, p. 510, 1973.
- [169] T. Iwasaki, M. Ogawa, K. Esumi, and K. Meguro, "Interactions between betaine-type zwitterionic and anionic surfactants in mixed micelles," *Langmuir*, vol. 7, no. 1, pp. 30–35, 1991.
- [170] A. Shiloach and D. Blankschtein, "Prediction of critical micelle concentrations and synergism of binary surfactant mixtures containing zwitterionic surfactants," *Langmuir*, vol. 13, no. 15, pp. 3968–3981, 1997.
- [171] P. M. Holland, *Modeling Mixed Surfactant Systems*, ch. 2, pp. 31–44.
- [172] H. Lu, M. Yuan, B. Fang, J. Wang, and Y. Guo, "Wormlike micelles in mixed amino acid-based anionic surfactant and zwitterionic surfactant systems," *Journal of Surfactants and Detergents*, vol. 18, no. 4, pp. 589–596, 2015.
- [173] T. Vu, P. Koenig, B. M. Cochran, K. Ananthapadmanabhan, M. Weaver, B. Reeder, H. D. Hutton, and G. B. Kasting, "Thickening mechanisms for an amino acid-derived surfactant composition," *Colloids and Surfaces A: Physicochemical and Engineering Aspects*, vol. 589, p. 124424, 2020.
- [174] J. Salvatier, T. V. Wiecki, and C. Fonnesbeck, "Probabilistic programming in python using PyMC3," *PeerJ Computer Science*, vol. 2, p. e55, apr 2016.
- [175] R. McElreath, *Statistical rethinking: A Bayesian course with examples in R and Stan*. CRC press, 2020.

- [176] K. Danov, S. Kralchevska, P. Kralchevsky, K. Ananthapadmanabhan, and A. Lips, "Mixed solutions of anionic and zwitterionic surfactant (betaine): surface-tension isotherms, adsorption, and relaxation kinetics," *Langmuir*, vol. 20, no. 13, pp. 5445–5453, 2004.



**OHIO**  
UNIVERSITY

Thesis and Dissertation Services